On the Dynamics of Massive Eccentric Nuclear Disks

by

Heather N. Wernke

B.S., Embry-Riddle Aeronautical University, 2016

M.S., University of Colorado, 2019

A thesis submitted to the

Faculty of the Graduate School of the

University of Colorado in partial fulfillment

of the requirements for the degree of

Doctor of Philosophy

Department of Astrophysical and Planetary Sciences

2021

Committee Members:

Ann-Marie Madigan, Chair

David Brain

Julie Comerford

Jason Dexter

Noah Finkelstein

Wernke, Heather N. (Ph.D., Astrophysical and Planetary Sciences)

On the Dynamics of Massive Eccentric Nuclear Disks

Thesis directed by Prof. Ann-Marie Madigan

The Andromeda Galaxy (M31) hosts an elongated nucleus that resolves into two distinct brightness peaks. The double nucleus is explained by an eccentric nuclear disk which consists of stars moving on apsidally-aligned orbits around a supermassive black hole. The same secular gravitational torques that dynamically stabilize these disks can produce tidal disruption events (TDEs) at very high rates. I use N-body simulations to show that this is true in both Newtonian gravity and with general relativistic precession. Additionally, I show that orbital elements between successive TDEs from eccentric nuclear disks are correlated.

The double nucleus in M31 may seem like an unusual feature, but many early-type galaxies in the local universe have asymmetric nuclei indicating the possible presence of eccentric nuclear disks. I create photometric (surface density) and kinematic (line-of-sight velocity) maps of eccentric nuclear disks using N-body simulations. By observing my simulations along many different lines of sight, I am able to classify them as double nuclei, offset nuclei, and centered nuclei. Observations of any of the photometric or kinematic signatures discussed here could be evidence for the potential of a galaxy hosting an eccentric nuclear disk.

Finally, I show that eccentric nuclear disks are not unique to galactic centers. Orbits cluster together in the scattered disk in the outer Solar System. The secular torques between orbits in the axisymmetric near-Keplerian disk cause a dynamical instability. After the inclination instability saturates, an eccentric nuclear disk forms. I present photometric and kinematic maps of the disk as the instability occurs and as the apsidal clustering persists afterwards. The observed clustering could explain the strange orbits of minor planets in the outer Solar System and is also expected to be found in exoplanetary systems.

Dedication

For Jesus Christ, King of the Universe.

Acknowledgements

My first big thank you goes to my research advisor, Dr. Ann-Marie Madigan, for providing excellent support, direction, and inspiration. I am so grateful to have had the opportunity to work with Ann-Marie, who genuinely cares about her students. Thank you for challenging me and for teaching me what it looks like to be a truly valued, respected, and trusted professor.

Infinite thanks to my parents, Glenn and Lynley Wernke for all of their love and support. I will always look up to my Mom and Dad. Thank you for being my greatest teachers and role models. I love you and am filled with gratitude.

I am so grateful for Fr. Peter Mussett and for his continual encouragement, direction, and friendship. Thank you to the entire St. Thomas Aquinas community for being there in the best moments, the worst moments, and everything in between.

Thank you to my wonderful roommate, Liz, who has become a great friend. Thank you for keeping me sane and for feeding me so many delicious meals. Thank you to my lovely friends, Suehyun and Lydia, for their faith-filled friendship, encouragement, prayers, laughter, and accountability.

Thank you to Greg and Cathy Babbitt for graciously allowing me to escape to their beautiful cabin to focus on writing.

There are so many people that this dissertation work would have been impossible without. Thank you for all of your prayers and love. Many thanks and blessings to all of you!

Contents

Chapter

Tables

Table

Figures

Figure

Chapter 1

Introduction

This thesis work focuses on the internal dynamics and observability of eccentric nuclear disks. I study the effects of general relativity on the tidal disruption event rate from eccentric nuclear disks. I also create simulated photometric and kinematic maps of eccentric nuclear disks from many different lines of sight. Finally, I apply my work of galactic nuclei to the outer Solar System. I cover relevant background and motivation in the following introduction. In Section 1.1, I introduce tidal disruption events, including their rates and observations. In Section 1.2, I explain the basics of loss cone dynamics. I then introduce eccentric nuclear disks in Section 1.3. This requires a description of different stellar relaxation processes. The study of eccentric nuclear disks is motivated by the nucleus of the Andromeda galaxy, which I introduce in Section 1.3.2. I then provide some background evidence that eccentric nuclear disks are common in the local universe. I then explain some of the basic dynamics of eccentric nuclear disks and how they could contribute to tidal disruption events. In Section 1.4 I introduce the scattered disk in the outer Solar System and explain how the secular dynamics in galactic nuclei are directly related to planetary systems. Finally, in Section 1.5 I provide a brief summary of what will be covered in this thesis.

The work presented here is based on the following publications:

- Madigan, A.-M., Halle, A., Moody, M., McCourt, M., Nixon, C., & **Wernke, H. N.** 2018a, ApJ, 853, 141
- **Wernke, H. N.**, & Madigan, A.-M. 2019, ApJ, 880, 42

- **Wernke, H. N.**, & Madigan, A.-M. 2021, ApJ, in review
- Zderic, A., Tiongco, M., Collier, A., Generozov, A., **Wernke, H. N.**, & Madigan, A.-M. 2021, AJ, in review

1.1 Tidal Disruption Events

A tidal disruption event (TDE) occurs when a star is violently ripped apart by a black hole's tidal forces (Hills 1975). When a star is tidally disrupted, roughly half of the stellar debris remains gravitationally bound to the black hole while the other half of the debris escapes, creating a high velocity tail. The gravitationally bound debris forms an accretion disk which feeds the black hole. As the stellar debris returns to the black hole with a fallback rate of $t^{-5/3}$ (Phinney 1989; Evans & Kochanek 1989; Lodato et al. 2009; Guillochon & Ramirez-Ruiz 2013), a flare of light is emitted (Rees 1988). Emission from a TDE occurs most often in optical, ultraviolet (UV), and X-ray wavelengths (Ulmer 1999). Several dozen TDE candidates have been identified in the last two decades, from UV/optical to X-ray. TDE candidates are generally identified as flaring events inconsistent with supernovae, at the centers of galaxies. The flare of light generally decays on timescales from months to years.

The flares that we observe from TDEs can provide insight into the mysteries of many areas of astrophysics. They can show us the existence of a central black hole in otherwise quiescent galaxies (Maksym et al. 2013; MacLeod et al. 2014). We can also use the observations of TDEs to test our theories of accretion physics and relativistic jets (Zauderer et al. 2011; Bloom et al. 2011; van Velzen et al. 2016; Alexander 2017). If something massive, like a white dwarf, were tidally disrupted, we should even be able to detect and learn about gravitational waves from the Light Interferometer Space Antenna (LISA) (MacLeod et al. 2014). TDEs could even be helpful for measuring the masses and spins of supermassive black holes. Additionally, we can test our understanding of gravitational stellar dynamics

near supermassive black holes by comparing theoretical TDE rates with observations.

A star is tidally disrupted when a black hole's tidal forces overcome the star's self-gravity. This occurs when a star reaches what is called the tidal radius. The tidal disruption radius is defined as:

$$r_t = R_* \left(\frac{M_\bullet}{M_*} \right)^{1/3}, \tag{1.1}$$

where $M_\bullet$ is the mass of the black hole, and M_* and R_* are the mass and radius of the disrupting star respectively. The tidal radius is derived by equating the Newtonian surface tidal acceleration due to the gravitational attraction of the supermassive black hole,

$$a = \frac{G M_\bullet R_*}{r_t^3}, \tag{1.2}$$

with the star's self-gravitational acceleration,

$$a = \frac{G M_*}{R_*^2}, \tag{1.3}$$

where G is the gravitational constant (Stone et al. 2019). One of the first dynamical explorations of a star being disrupted as it crossed the tidal radius was presented by Rees (1988). His graphical representation is included here, in Figure 1.1. One can see that the star is distorted before it reaches the tidal radius, then when it does reach the tidal radius, it is fully disrupted and torn into debris. The escape velocity for a solar-type star in this situation is $\sim 10^3$ km/s. The specific gravitational self-binding energy (the energy required to tear the star apart) is $\sim 10^{-5} c^2$ with a spread of $\sim 10^{-3} c^2$, where c is the speed of light. Half of the stellar debris remains bound to the black hole on eccentric orbits. The other half of the stellar debris escapes on unbound, hyperbolic orbits. The specific binding energies and escape speeds of the debris are calculated assuming a supermassive black hole mass of $M_\bullet \geq 10^6 M_\odot$, where $M_\odot$ is a solar mass (Rees 1988).

It is well known that TDEs are fundamentally general relativistic events, as they are the result of the strong tidal forces of supermassive black holes. We can easily confirm this by comparing the tidal radius (Equation 1.1) to the black hole's gravitational radius, defined

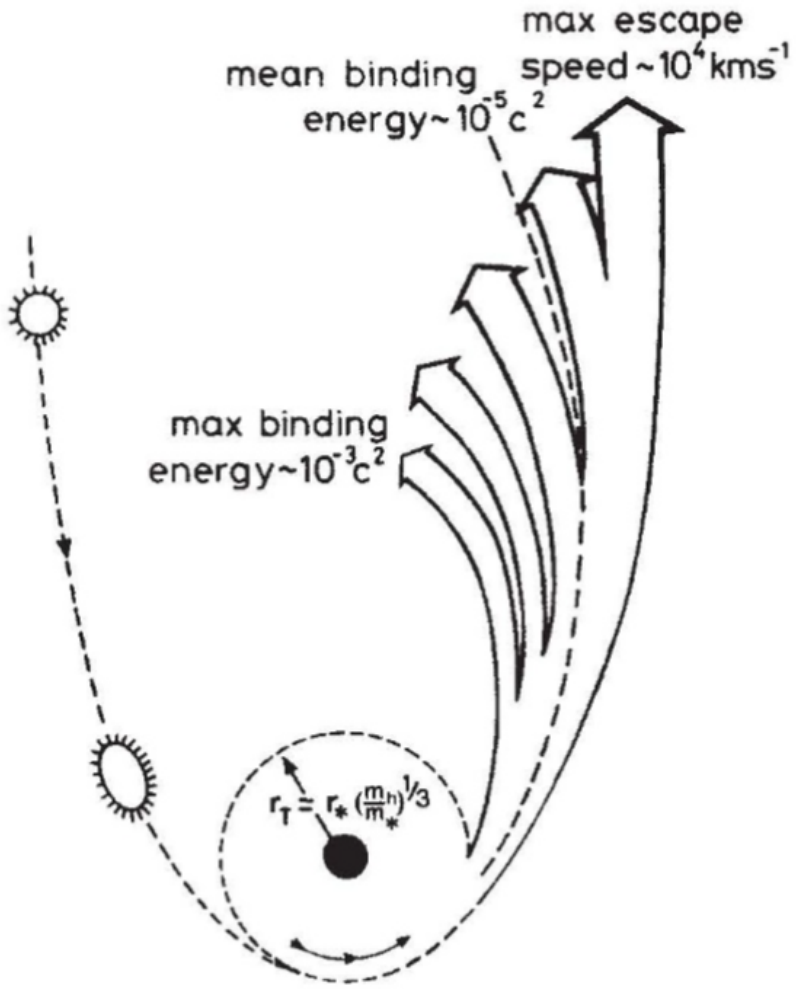

Figure 1.1: **A star is tidally disrupted.** A solar-type star approaching a supermassive black hole on a parabolic orbit with pericenter distance r_t is distorted during infall, and then tidally disrupted when it reaches pericenter. Half of the debris escapes on hyperbolic orbits (with a maximum escape speed $\sim 10^4$ km/s), while the other half remains bound to the black hole on elliptical orbits (with a maximum binding energy $\sim 10^{-3} c^2$). This Figure is from Rees (1988).

by,

$$r_g = \frac{GM_\bullet}{c^2}. \tag{1.4}$$

For the smallest supermassive black holes, the tidal radius is much larger than the gravitational radius, but for larger supermassive black holes the tidal radius is on the same order of the gravitational radius, meaning that general relativity is fundamental to understanding

the physics of TDEs (Stone et al. 2019).

The strength of a TDE is quantified by the penetration factor, which is defined as,

$$\beta = \frac{r_t}{r_p}. \tag{1.5}$$

r_p is the pericenter of the star's orbit, the point closest to the black hole. Encounters with very large β will result in the star being swallowed whole, while encounters with very small β will result in partial disruptions. A partial disruption means that a star's outer layers will be stripped, but its core remains intact.

1.1.1 Rates and Observations of Tidal Disruption Events

The current detection rate of flares from TDEs is about two per year (van Velzen 2018). This is expected to increase with new surveys such as the Legacy Survey of Space and Time (LSST) with the Vera Rubin Observatory (van Velzen et al. 2011). LSST will map the entire sky in just a few nights. Bricman & Gomboc (2020) estimate that LSST will detect between 10-22 TDEs per night. The eROSITA telescope is expected to observe $\sim 10^3$ TDEs per year (Khabibullin et al. 2014).

TDE rates are traditionally derived under the assumption that stars are found in a spherical distribution around the central supermassive black hole and are driven to the black hole (Wang & Merritt 2004; Stone & Metzger 2016). Theoretical TDE rates in these spherical nuclear star clusters have been calculated to be 2.1×10^{-4} yr^{-1} gal^{-1} (Wang & Merritt 2004), and more recently 2.0×10^{-4} yr^{-1} gal^{-1} (Stone & Metzger 2016). In observations, however, TDEs are preferentially found in rare post-merger or post-starburst galaxies (K+A/E+A galaxies) at much higher rates. K+A/E+A galaxies are a relatively rare subtype of elliptical galaxy that underwent a major starburst about 1-1.5 Gyr ago (Couch & Sharples 1987; Poggianti 2004). These galaxies are named in this way due to the A star characteristic Balmer absorption features in their spectra. The Balmer absorption appears superimposed on an old K star or early-type galaxy population (Dressler & Gunn 1983). K+A/E+A

galaxies make up 0.2% of the galaxies in the local universe, and yet, the observed TDE rates in these K+A/E+A galaxies are $1 - 3 \times 10^{-3}$ yr^{-1} gal^{-1}, which pushes the observed TDE rate of 'normal' galaxies down to $1 - 5 \times 10^{-6}$ yr^{-1} gal^{-1} (French et al. 2016). There is even evidence that the TDE rate could be as high as 10^{-1} yr^{-1} gal^{-1} in ultra-luminous infrared galaxies (ULIRGs), which are galaxies typically in the process of merging (Tadhunter et al. 2017; Dou et al. 2017). We learn from these observations that merging galaxies and post-merger galaxies tend to have elevated TDE rates.

The open TDE catalog[1] currently has 97 observed TDE candidate events, one of the most well-studied events being ASASSN-14li. ASASSN-14li is one of the nearest (90 Mpc) TDEs discovered, so it has been observed at many wavelengths, creating a rich data set (Kara et al. 2018). ASASSN-14li is hosted by an E+A galaxy (Prieto et al. 2016). It is a luminous flaring event at the center of a galaxy that is inconsistent with supernovae. Candidates are typically excluded from the TDE catalog if the host galaxy shows signs of active galactic nuclei (AGN) activity, which introduces observational biases in the sample of TDE candidate host galaxies. The first TDEs were discovered in the 1990s and were observed at X-ray wavelengths. TDEs have since been observed across the electromagnetic spectrum, from radio to gamma-ray wavelengths. The observed emission depends on many different parameters, such as the mass of the black hole, the mass of the star, and the size and structure of the star. Observing the light curves, then, should tell us about the stars that were disrupted, and about the supermassive black holes responsible for the disruption.

There have been a number of alternative ideas to explain these flaring events at galactic centers. Proposed TDE impostors include supernovae in AGN disks and black hole accretion disk instabilities (Saxton et al. 2016). One distinguishing feature that can be used to discriminate between real TDEs and TDE impostors is the critical black hole mass beyond which a TDE will not be observable, known as the Hills mass (Hills 1975). The Hills mass results from the fact that the tidal radius and Schwarzschild radius of a black hole scale

[1] https://tde.space/

differently with the mass of the black hole. In Equation 2.1, we see r_t is proportional to $M_\bullet^{1/3}$. The Schwarzschild radius is defined by,

$$r_s = 2r_g = \frac{2M_\bullet G}{c^2}. \tag{1.6}$$

The Schwarzschild radius describes the location of the event horizon of the black hole. This is the horizon beyond which nothing can escape the black hole's gravitational force. By comparing the tidal radius to the Schwarzschild radius, we learn what size black hole will swallow stars completely, meaning that no gas will be left outside the event horizon to be observed as a luminous flare (Hills 1975; MacLeod et al. 2012). This occurs when the tidal radius is inside the Schwarzschild radius, which is true for any black hole above a Hills mass, defined by,

$$M_H = \left(\frac{c^2 R_*}{2G}\right)^{3/2} M_*^{-1/2}. \tag{1.7}$$

This is simply found by equating the tidal radius and the Schwarzschild radius. The Hills mass indicates that a white dwarf can only be disrupted by an intermediate mass black hole ($M_\bullet < 10^5 M_\odot$), while a red giant can be disrupted by even the most massive supermassive black holes ($M_\bullet \simeq 10^{10} M_\odot$) (MacLeod et al. 2012). For a solar-type star of $1M_\odot$ and $1R_\odot$, $M_H \approx 10^8 M_\odot$. A rapidly spinning black hole will raise this limit to $\sim 10^9 M_\odot$, as shown in Figure 1.2. Recently, van Velzen (2018) presented the black hole mass function of optical/UV-selected TDE candidates and showed a sharp decrease in the number of candidates above $M_\bullet = 10^{7.5} M_\odot$, as shown in Figure 1.3. This is consistent with the direct capture of stars when the black hole is above the Hills mass and can be used to provide strong evidence that we are seeing TDEs rather than TDE impostors.

1.2 Loss Cone Dynamics

An orbit is described by its energy (E) and angular momentum (J). A Kepler orbit is additionally described by its eccentricity vector ($\boldsymbol{e}$) and angular momentum vector ($\boldsymbol{J}$). The eccentricity vector points from the supermassive black hole to the pericenter of the

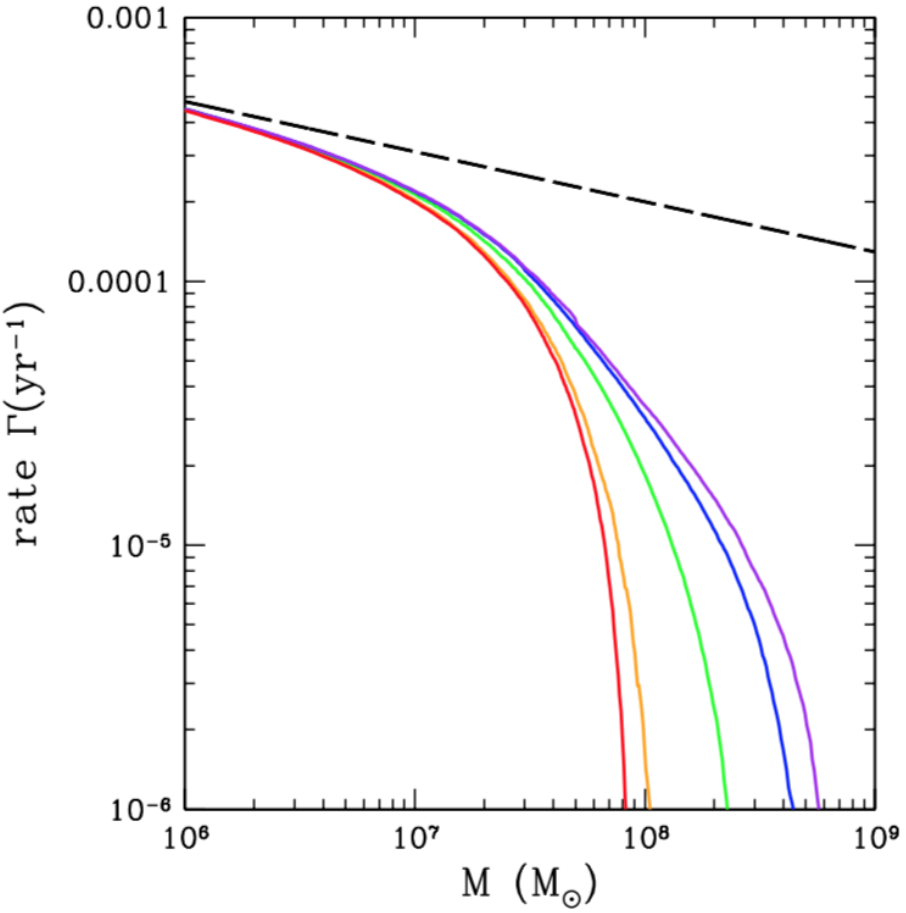

Figure 1.2: **TDE rates for galaxies with black holes of differing spins.** The TDE rate increases with supermassive black hole spin. The dashed line shows the TDE rate predicted by Wang & Merritt (2004). The colored curves show the relativistic correction to that prediction. The red curve corresponds to a spin of $a/M = 0$, orange is 0.5, green is 0.9, blue is 0.99, and purple is 0.999. This figure is from Kesden (2012).

orbit. The energy and angular momentum describe the size and shape of the orbit, while the eccentricity and angular momentum vectors describe the orientation of the orbit. These are the quantities we follow in order to track orbital changes.

The number and rate of TDEs from two-body relaxation have been studied extensively (Frank & Rees 1976; Lightman & Shapiro 1977; Shapiro & Marchant 1978; Cohn & Kulsrud 1978; Stone & Metzger 2016). Two-body relaxation is the process by which stars exchange energy and angular momentum amongst themselves, and hence change their orbits. Some-

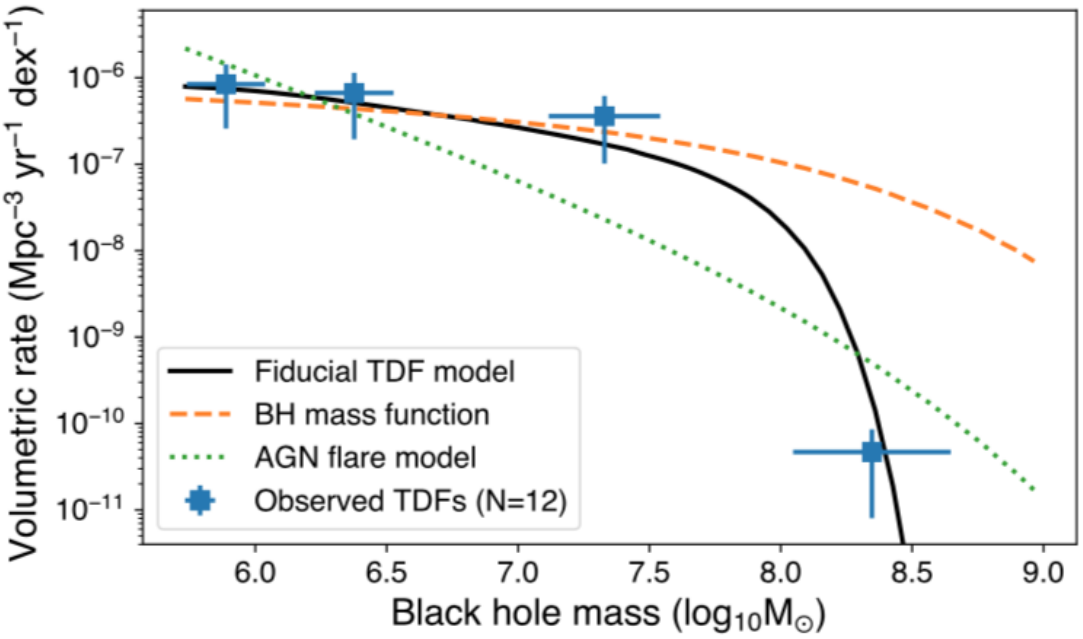

Figure 1.3: **TDE rates as a function of black hole mass.** The number of candidates decreases sharply with black holes of masses greater than $10^{7.5}M_\odot$, which is a signature of the Hills mass. This figure is from the top panel of Figure 3 in van Velzen (2018).

times an interaction between two stars can change the angular momentum and energy of one of them in a way such that the star will be tidally disrupted.

In order for a star in these systems to get close enough to the supermassive black hole to tidally disrupt, it must enter a region called the loss cone. The loss cone is defined as the region containing orbits with pericenter inside the tidal radius of the supermassive black hole. The pericenter of an orbit is within the tidal radius if it's angular momentum is less than the angular momentum of the loss cone, $J_{\rm LC}$. Orbits contained by the loss cone have an angular momentum less than the angular momentum of an orbit with a pericenter equal to the tidal radius,

$$J < J_{\rm LC} = \sqrt{2GM_\bullet r_t}. \tag{1.8}$$

This expression assumes that the star is on an orbit with semi-major axis much greater than r_t. In other words, it assumes the orbit is eccentric.

Stars in this region will be disrupted within one orbital period, unless their orbits are

perturbed out of the loss cone before reaching pericenter (Rauch & Tremaine 1996). They are on doomed orbits. Their velocity vectors point to a point inside the tidal radius of the black hole. In order for these velocity vectors to be associated with orbits that pass within the tidal radius, the star's velocity vector must lie within a cone of half-angle $\theta_{\rm LC}$, given by:

$$\theta_{\rm LC} \approx \begin{cases} \left(\frac{r_t}{r}\right)^{1/2} & r \lesssim r_h \\ \left(\frac{r_t r_h}{r^2}\right)^{1/2} & r \gtrsim r_h \end{cases} \tag{1.9}$$

where r is the distance of the star from the supermassive black hole and r_h is the radius of influence of the supermassive black hole. The rate of TDEs is set by the rate at which relaxation processes repopulate the loss cone.

1.2.1 Loss Cone Regimes

There are two loss cone regimes, defined by the parameter, q,

$$q = \left(\frac{\Delta J_{\rm P}}{J_{\rm LC}}\right)^2. \tag{1.10}$$

$\Delta J_{\rm P}$ is the change in angular momentum per orbital period. If $q \ll 1$, stars take multiple orbital periods to enter into the loss cone. This is known as the empty loss cone regime or the diffusion limit. In two-body relaxation, stars random walk in angular momentum space into the loss cone. This occurs inside the black hole's radius of influence. If, on the other hand, $q \gg 1$, then stars can jump into and out of the loss cone within just one orbital period. This is known as the full loss cone regime or the pinhole limit. The pinhole regime begins near the radius of influence of the black hole where the orbital periods are long (Lightman & Shapiro 1977). In the pinhole limit, the loss cone is rapidly replenished, while the diffusive limit keeps the loss cone normally unoccupied because it takes many orbital periods for one star to slowly migrate into the loss cone.

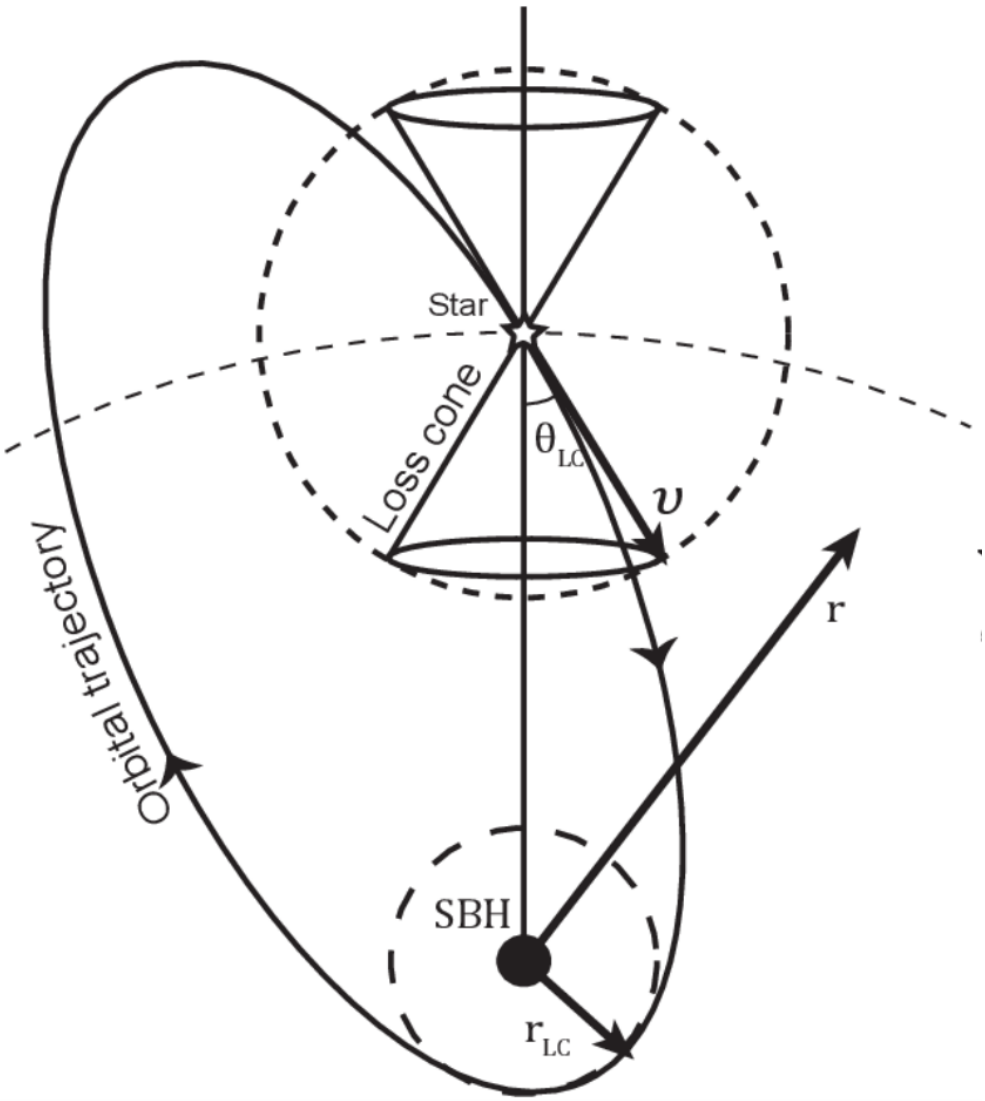

Figure 1.4: **Representation of the loss cone.** Orbits with velocity vectors that fall within the loss cone (of half-angle $\theta_{\rm LC}$) will pass within the disruption sphere at $r_{\rm LC}$, which is the same as the tidal radius. This figure is from Merritt (2013).

1.3 Eccentric Nuclear Disks

1.3.1 Stellar Relaxation

Hills initially predicted that the TDE rate could be high enough to contribute to the growth of supermassive black holes and activity in AGN. This prediction was based on the assumption that stellar relaxation due to two-body relaxation could rapidly refill a depleted

loss cone (see Section 1.2 on loss cone dynamics and Section 1.3.1 on stellar relaxation) (Hills 1975).

Relaxation is the process by which stars interact with each other to move towards a system in equilibrium. It is commonly assumed that TDE rates in galactic nuclei are dominated by two-body relaxation processes. Two-body relaxation occurs because of gravitational interactions between stars in the system. A single star can gravitationally change the orbit of another single star. These gravitational interactions cause changes in energy and angular momentum. As the interactions are random, the energy and angular momentum random-walk (or diffuse) in phase-space. The change in energy (ΔE) and the change in angular momentum (ΔJ) therefore grow with time proportionally to $t^{1/2}$. This, however, is not the only form of relaxation present in galactic nuclei.

Resonant relaxation arises in systems with nearly Keplerian orbits (Tremaine 1998). In galactic nuclei hosting supermassive black holes, the gravitational potential in the inner nucleus is dominated by the black hole, meaning it is nearly Keplerian. When orbits are Keplerian, a particle on the orbit will trace out the same path multiple times. Instead of N number of stars, then, we can think of N orbits. Each orbit is an ellipse, with mass equal to the stellar mass, and density inversely proportional to the local speed in the orbit. Each orbit can therefore be treated as a wire, as a tool to understand the orbital dynamics. On a timescale less than the precession timescale, the orbits remain ∼fixed, and exert mutual torques on each other. This is different from interactions in two-body relaxation, which simply look at the encounters between two particles at a time. Resonant relaxation has been studied in spherical stellar systems (Rauch & Tremaine 1996) as well as in protoplanetary disks (Tremaine 1998). In resonant relaxation, the angular momentum relaxation can be greatly enhanced, while the energy relaxation is unaffected. The angular momentum relaxation timescale therefore becomes much shorter than the energy relaxation timescale (Rauch & Tremaine 1996). Angular momentum relaxation provides a steady supply of stars to the loss cone.

Ignoring general relativistic effects, resonant relaxation is most important and efficient for stars in orbits that are very close to the central supermassive black hole and are nearly Keplerian. This means that in a spherical stellar distribution, where TDEs come most often from near the radius of influence, resonant relaxation will not greatly increase the rate or number of TDEs (Rauch & Ingalls 1998). Additionally, resonant relaxation is much more efficient on eccentric orbits than on circular orbits, because the torque that changes the angular momentum is linearly proportional to eccentricity (Gürkan & Hopman 2007).

1.3.2 The Double Nucleus in Andromeda

Not all galactic nuclei, however, are like our galactic center - spherically symmetric in distribution. The nucleus of our nearest galactic neighbor, Andromeda (M31), has a very different configuration. The M31 nucleus has been a curious target for astronomers ever since it was first imaged by the balloon-borne telescope, Stratoscope II, with a resolution of $0\farcs2$ in 1971 (Light et al. 1974). The Stratoscope II images show that the nucleus of M31 is elongated and asymmetrical, with a faint extension on one side of the peak. Spectroscopic observations similarly show asymmetric kinematic profiles. The velocity dispersion peak is displaced from the velocity center by $0\farcs2 \pm 0\farcs03$ away from P1 (Dressler & Richstone 1988; Kormendy 1988; Kormendy & Bender 1999). The Hubble Space Telescope (HST) revealed that M31's nucleus appears asymmetric because it is a double nucleus, now resolved into two distinct brightness peaks as shown in Figure 3.4. The HST images were taken with the Wide Field/Planetary Camera (WF/PC) with a resolution of $0\farcs044$ per pixel. Images were taken in both the V (visual) and I (infrared) bands. A contour map of the nucleus is shared in Figure 1.6. There is a faint peak (P2) lying approximately at the bulge center, and a brighter component (P1) which is offset by $0\farcs5$ (≈ 2 pc) (Lauer et al. 1993). P1 corresponds to the offset peak observed by Stratoscope II. P2 lies within the faint extension to the peak that was noted by Light et al. (1974).

An initial hypothesis to explain the two brightness peaks is that P1 and P2 are two

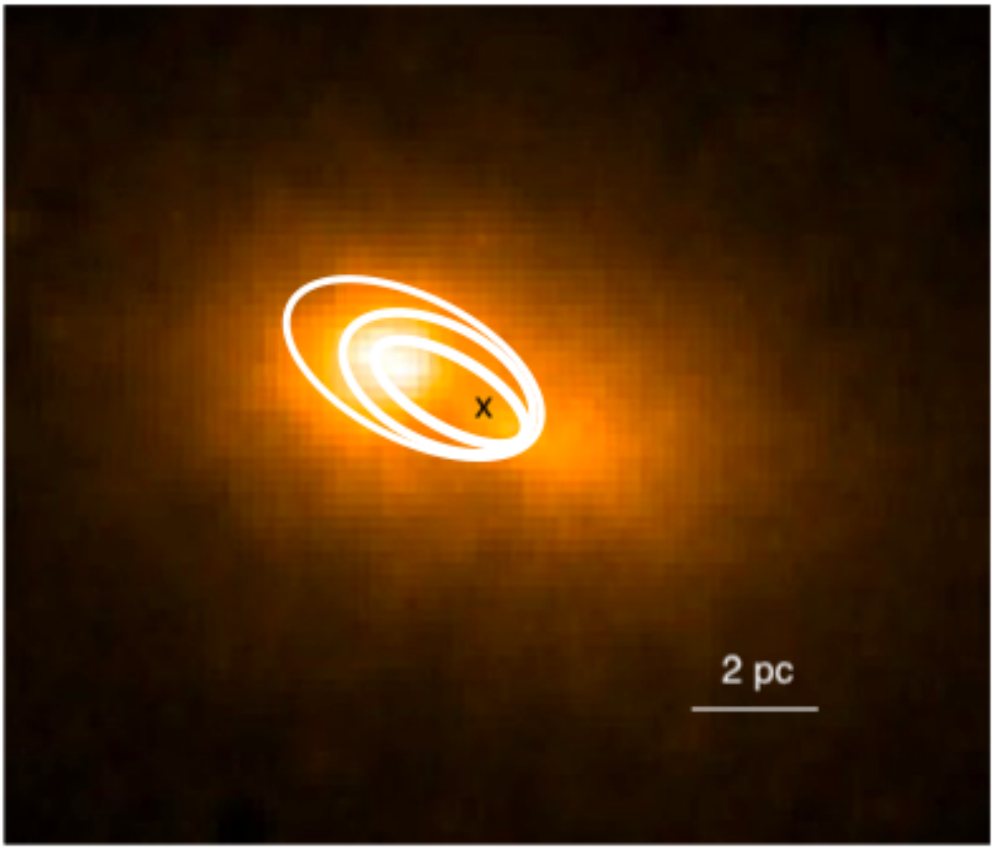

Figure 1.5: **The double nucleus of Andromeda Galaxy (M31).** Hubble Space Telescope (HST) image of the nucleus of M31 (Lauer et al. 1993). The image is overlaid with eccentric orbits in order to visualize the eccentric disk structure. The x marks the position of the black hole. The brighter peak at apocenter is designated P1 and the fainter peak at pericenter is designated P2.

separate star clusters. Two star clusters in that proximity, however, would decay due to dynamical friction, which causes the loss of energy as the clusters gravitationally interact with the surrounding matter in the bulge. Dynamical friction would therefore cause two separate star clusters to merge on a very short timescale ($\lesssim 10^8$ yr), making it very improbable to find that configuration in M31 (Lauer et al. 1993; Tremaine 1995). The same double peak is seen in the near-infrared, indicating that there is not a dust band creating a dip in brightness (Davidge et al. 1997; Corbin et al. 2001). We also learn from Kormendy & Bender (1999) that both P1 and P2 have K-type stellar populations and are nearly identical. This suggests that the two brightness peaks must comprise a single system of stars.

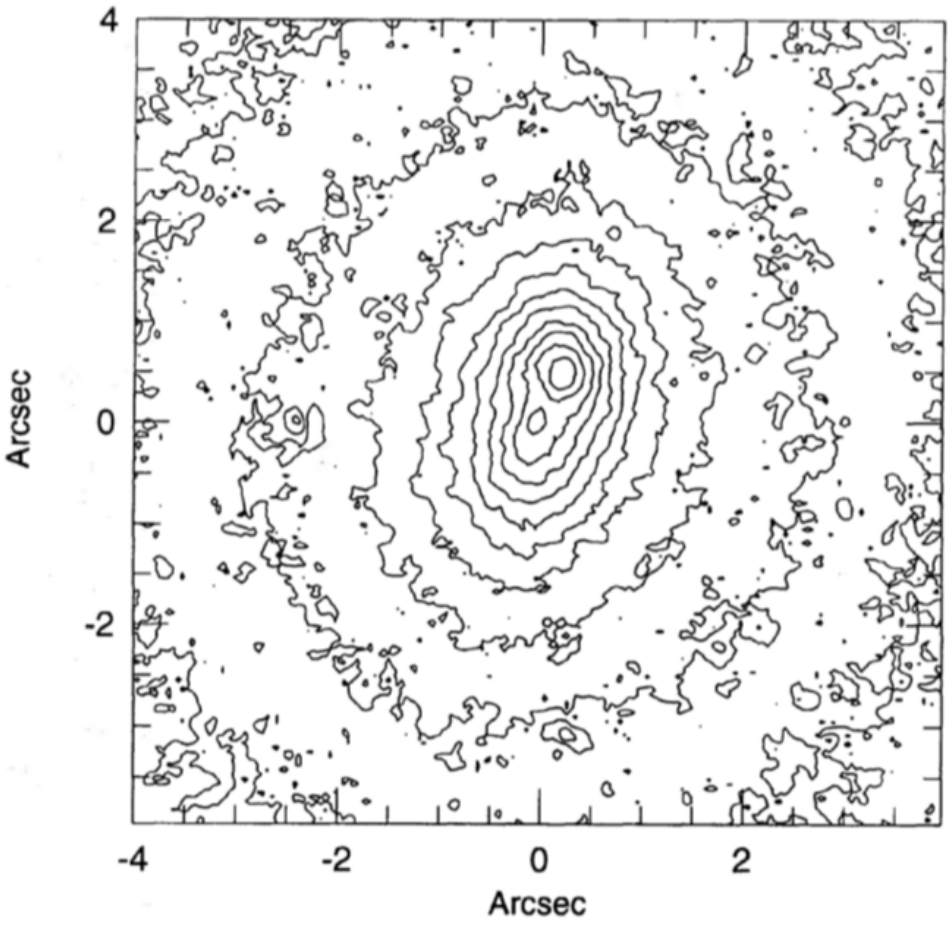

Figure 1.6: **Contour map of the M31 nucleus.** This plot shows contours of the V band image. This figure is rotated 70° from the photometry in Figure 3.4. This figure is from Lauer et al. (1993).

The double-peaked nucleus can be explained by a thick eccentric nuclear disk of Keplerian orbits around a supermassive black hole (Tremaine 1995). An eccentric nuclear disk is found within the radius of influence of the supermassive black hole and all of the orbital eccentricity vectors are aligned. P1 corresponds to apocenter (the furthest point from the black hole) of the eccentric nuclear disk and P2 corresponds to the pericenter of the eccentric nuclear disk. P1 is bright because stars spend the most time in their orbits at apocenter according to Kepler's laws. P2 is a result of disk stars with small semi-major axes and all of the orbits' pericenters being pinched together (Tremaine 1995). Tremaine's model says that

the black hole and bulge center should be displaced from P2 towards P1 by $0\farcs02$, putting them at a focus of the eccentric disk rather than at pericenter. This is in agreement with Lauer et al. (1993) and King et al. (1995), who estimated that the bulge center is displaced from P2 towards P1 by $0'' - 0\farcs05$.

Tremaine (1995) takes the eccentric disk to be lying in the plane of the disk of M31. The orientation of the disk is described by three angles $[\theta_a, \theta_i, \theta_l]$ defined in Peiris & Tremaine (2003). θ_a is the azimuthal angle, measured in the disk plane from the ascending node of the disk on the sky to the symmetry axis of the disk. θ_i is the inclination angle. θ_l is the angle in the sky plane from the x-axis to the ascending node of the disk on the sky. In the aligned model from Tremaine (1995), the orientation of the disk is $[\theta_a = -11°, \theta_i = 77.5°, \theta_l = -52.3°]$. Peiris & Tremaine (2003) later showed that an eccentric nuclear disk model not aligned with the M31 disk better fits the observations. The orientation parameters for the non-aligned model are $[\theta_a = -34.5°, \theta_i = 54.1°, \theta_l = -42.8°]$. Figure 1.7 shows the observed surface brightness, Tremaine's 1995 fit, and the bulge and disk contributions to the total surface density profile of the M31 nucleus. We see here that the bulge enhances P2 in observations.

1.3.3 Evidence for the Common Prevalence of Eccentric Nuclear Disks

While it may seem like the central disk in M31 is an unusual and unlikely arrangement, the fact that we see it in our closest major galaxy suggests that it may actually be a common configuration. In fact, despite observational challenges, Lauer et al. (2005) found that about 15% of nearby, early-type galaxies have features that suggest they may host eccentric nuclear disks. While the galaxies in the Lauer et al. (2005) sample are very difficult to resolve (the eccentric nuclear disks are within the radius of influence of the supermassive black hole), the features that they see are what we would expect if we were seeing eccentric nuclear disks from different angles on the sky. They see galaxies with asymmetric nuclei and even some with central minima.

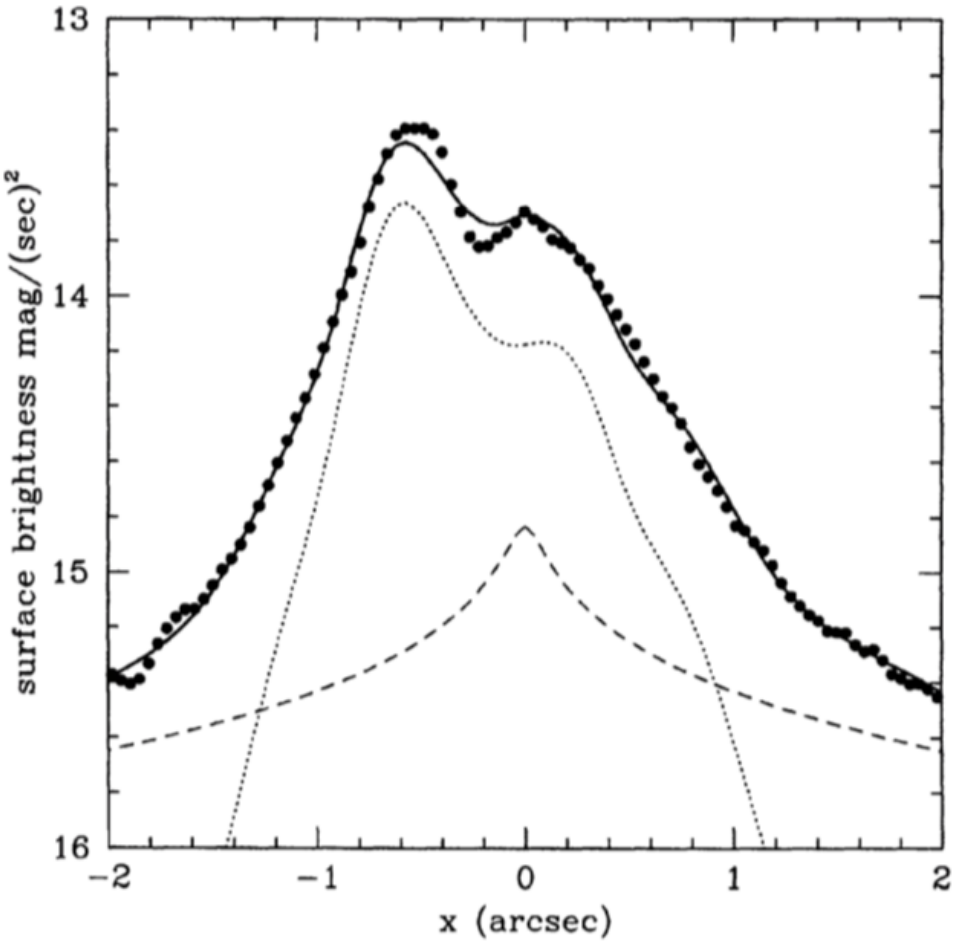

Figure 1.7: **Surface brightness profile of the M31 nucleus along the P2-P1 axis.** The filled circles show the observed data from the Hubble Space Telescope. The solid line shows Tremaine's best-fit aligned model. The dashed line shows the contribution of the bulge to the surface density profile. The dotted line shows the contribution of the eccentric nuclear disk to the surface density profile. The bulge enhances P2 relative to P1 in observations. This figure is from the top panel of Figure 1 in Tremaine (1995).

In 1996, Lauer et al. (1996) showed that NGC 4486B has a double nucleus, like the one in M31. NGC 4486B is a compact, low-luminosity elliptical galaxy, companion to the much larger NGC 4486 (M87). HST observations of NGC 4486B reveal two brightness peaks separated by 10-13 parsecs. The two peaks are at similar distances from the photocenter, but as with M31, the peak that is further from the center is the brighter peak, suggesting that it corresponds to apocenter of an eccentric nuclear disk. Figure 1.8 shows the HST V,

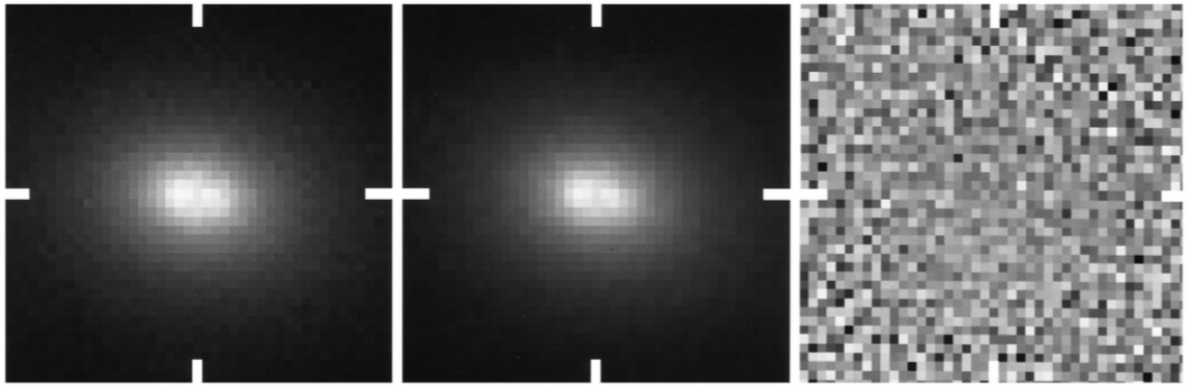

Figure 1.8: **V, I, and color ratio images of NGC 4486B.** P1 is on the left and P2 is on the right. The tick marks indicate the photocenter of the galaxy. This figure is from Lauer et al. 1996 Lauer et al. (1996).

I, and color ratio images of NGC 4486B from Lauer et al. (1996). The color ratio image indicates that dust is not causing the central dip in brightness. NGC4486B is viewed in a nearly edge-on orientation.

Lauer et al. (2002) present observations of six early-type galaxies that have central minima in their nuclei, possibly related to M31 and NGC 4486B. NGC 3706 is an S0 galaxy (also known as a lenticular galaxy with properties of both elliptical and spiral galaxies) viewed edge-on, featuring a bright nuclear stellar ring or torus. NGC 4406 and NGC 6876 are both giant elliptical galaxies with central minima in their nuclei. A260, A347, and A3574 are brightest cluster galaxies (the brightest galaxy in a cluster of galaxies) with dips in their core brightness profiles. Lauer et al. (2002) explain that it is very possible that all six of these galaxies may contain stellar tori and features similar to the double nucleus found in M31.

Lauer et al. (2005) present yet another galaxy sample. Again, they find several galaxies in their sample that have features suggestive of an eccentric nuclear disk. Of 65 non-dust obscured early-type galaxies, they find that 6.15% have central minima, 1.54% have double nuclei, and 7.69% are offset. One of the galaxies that they classify as having a central minimum, NGC 4382 (a bright S0 galaxy), strongly resembles the double nucleus of M31.

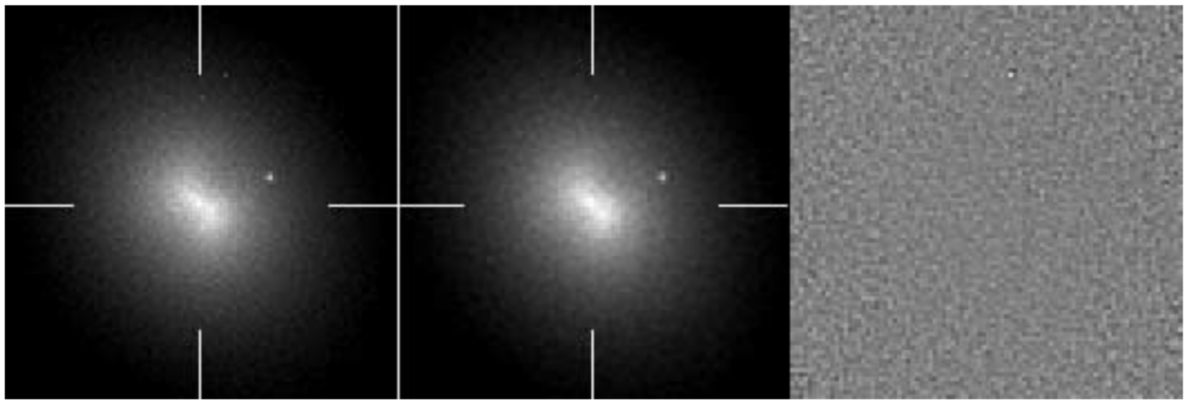

Figure 1.9: **V, I, and color ratio images of NGC 4382.** P1 is on the right and P2 is on the left. The tick marks indicate the photocenter of the galaxy. The color ratio image shows that there is no central dust absorption. This figure is from Lauer et al. 2005 Lauer et al. (2005).

The V, I, and color ratio images of the NGC 4382 nucleus are shown in Figure 1.9. In these images, the central minimum is a sort of valley between two brightness peaks, likely explained by an eccentric nuclear disk. Again, the color ratio image indicates that the dip in brightness is not due to dust obscuration.

Recently, Alonso-Herrero et al. (2018) were able to resolve the nucleus of NGC 5643, a nearby Seyfert galaxy, with the Atacama Large Millimeter/sub-millimeter Array (ALMA). Similar to M31, they see two peaks of emission and an asymmetric structure, but with an AGN at the center.

Finally, Gültekin et al. (2014) follow up with spectroscopic observations of the stellar torus in NGC 3706, originally presented by Lauer et al. (2002). They find that the ratio of mean velocity to velocity dispersion is an unexpectedly low value. They conclude that the stellar torus is not consistent with an axisymmetric ring of stars on circular orbits, and that the disk must contain stars orbiting in both directions. They did not, however, consider that an eccentric nuclear disk could explain their observations.

Clearly there is evidence that eccentric nuclear disks must be common in the local universe, so now we must venture to explain them dynamically.

1.3.4 Secular Torques and Stability

Until recently, the stability of eccentric nuclear disks has been a mystery. One would expect that the apsidal precession of individual orbits would spread out the disk into an axisymmetric structure on a timescale much shorter than the age of the stars that we observe in the disk. In a perfectly Keplerian potential, the angular momentum and eccentricity vectors of an orbit are constant. Adding a small Keplerian force, however, such as general relativity and perturbations from surrounding stars, cause changes in the angular momentum and eccentricity vectors. Rotation in eccentricity vectors is called precession. The orbits precess in time by:

$$\boldsymbol{J}' = \boldsymbol{\tau} = \boldsymbol{r} \times \boldsymbol{F} \tag{1.11a}$$

$$\boldsymbol{e}' = \frac{1}{GM_\bullet} \left(\boldsymbol{F} \times \boldsymbol{J} + \boldsymbol{v} \times \boldsymbol{\tau} \right), \tag{1.11b}$$

where $\boldsymbol{\tau}$ is the torque created by the non-Keplerian force, $\boldsymbol{F}$, and $\boldsymbol{v}$ is the velocity of the star. The precession of the eccentricity vectors depends on the orbital semimajor axes, which means we would expect the eccentricity vectors to spread out within the timescale of differential precession. This would mean that the eccentric disk observed in the nucleus of M31 and other galaxies, would indeed be transient phenomena.

This, however, only looks at half of the picture. The forces that cause a precession in eccentricity vectors also result in a build up of gravitational torques between orbits (Rauch & Tremaine 1996). Because the mass of the eccentric nuclear disk in M31 is about 15% of the mass of the supermassive black hole, the secular (orbit-averaged) gravitational torques between orbits are very strong and hold the disk together. Figure 1.10 shows how these torques stabilize the eccentric nuclear disk. An eccentric nuclear disk precessing in a prograde direction with a mass that is much greater than the background stellar potential will be stable. If one orbit (shown in red in the left panel of Figure 1.10) is perturbed slightly ahead of the disk, it will feel a gravitational pull back towards the disk. This gravitational force, in the negative direction of motion, negatively torques the orbit (see Equation 1.11a). The

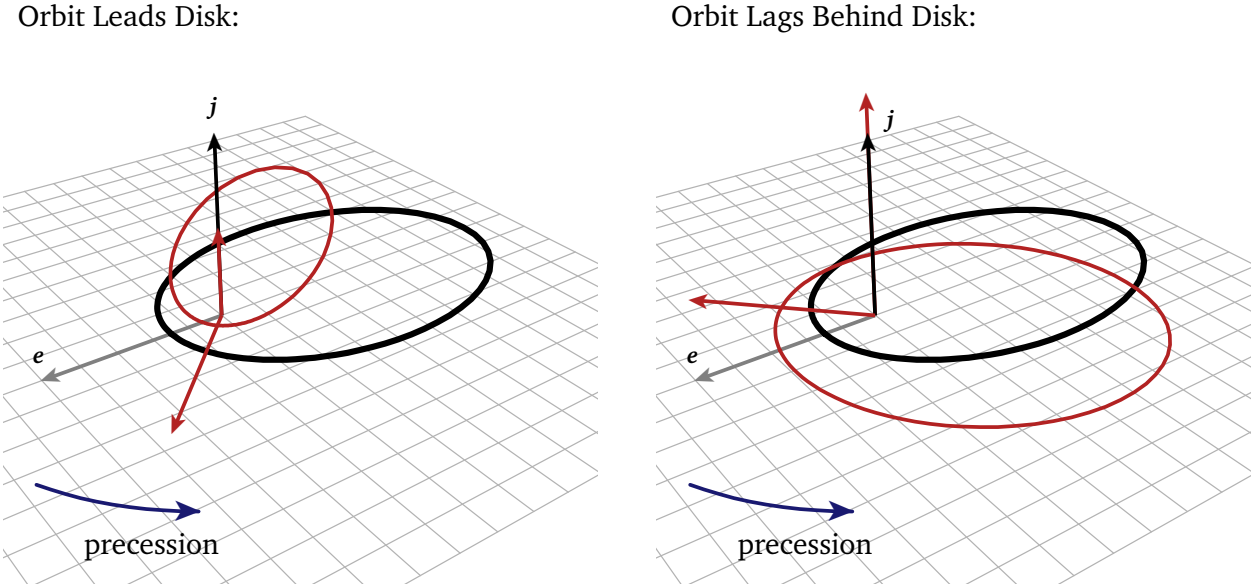

Figure 1.10: **Oscillations of orbits in a stable eccentric nuclear disk.** The eccentric nuclear disk is represented here in black as one ellipse. The disk precesses in a prograde (counter-clockwise) direction. In red is a single orbit that has been perturbed slightly ahead of (left panel) or slightly behind (right panel) the disk. When this orbit is ahead of the disk, it feels a gravitational pull back towards the black disk. This gravitational pull causes the orbit to be negatively torqued, which results in an increase in eccentricity. A more eccentric orbit precesses more slowly, so the disk is then able to catch back up with the orbit. Similarly, if an orbit is behind the disk, it will feel a gravitational pull that causes the orbit's eccentricity to decrease, hence precessing faster and catching back up with the disk. The overall effect is to stabilize the disk. This figure was originally published in Madigan et al. (2018a).

negative torque causes a decrease in the orbital angular momentum, and therefore increases the orbital eccentricity. Eccentricity is related to an orbit's specific angular momentum by the following equation:

$$j = \sqrt{GM_{\bullet}a(1-e^2)}, \tag{1.12}$$

where a is the orbit's semi-major axis and e is the orbital eccentricity. Because more circular orbits have smaller eccentricity, they are easier to rotate and will precess faster than orbits with larger eccentricities. This means that the orbit that was perturbed slightly ahead of the eccentric disk will slow down until the disk is able to catch up to it, keeping the disk in a stabilized orientation. Similarly, as shown in the right panel of Figure 1.10, if the orbit is

perturbed slightly behind the disk, the orbit will be positively torqued, causing an increase in angular momentum and decrease in eccentricity. This means that an orbit behind the disk will precess more rapidly until it catches back up to the disk. Therefore, the eccentric nuclear disk remains stable (Madigan et al. 2018a). This stabilizing mechanism also means that perturbed orbits undergo oscillations in eccentricity as well as oscillations in orientation about the disk.

Figure 1.11 shows the result of N-body simulations presented in Madigan et al. (2018a). These simulations were run with $N = 100-1000$ stars on eccentric ($e = 0.8$) apsidally-aligned orbits in Newtonian gravity. The plot shows the x and y components of the eccentricity vector in the plane of the disk. This confirms that a prograde precessing (counter-clockwise) eccentric nuclear disk remains stable, with the bulk of the disk precessing together. The orbits in the outer edge of the disk (5-10% of the disk mass) are pushed beyond the initial outer edge by two-body relaxation. These orbits precess slower and with retrograde (clockwise) motion. The mean precession rate of the disk slows due to two-body relaxation increasing the semi-major axes of the stellar orbits.

The stabilizing mechanism described earlier naturally results in a disk with a negative eccentricity gradient, meaning that the orbital eccentricities decrease as a function of semi-major axis. Orbits at low semi-major axis must increase their eccentricities, while orbits at high semi-major axis must become more circular, in order for the disk to stably precess as one body. Figure 1.12, initially presented in Madigan et al. (2018a), shows that this holds true in N-body simulations of eccentric nuclear disks. The top panel of Figure 1.12 shows that the mean eccentricity is very high ($\langle e \rangle \approx 0.95$) at the inner edge of the disk, while much lower ($\langle e \rangle \approx 0.3$) at the outer edge of the prograde-precessing disk. Orbits beyond $a \gtrsim 2.3$ precess with retrograde motion. The bottom panel of Figure 1.12 shows that a stable eccentric nuclear disk also has an inclination distribution in semi-major axis with a negative gradient. The high eccentricity orbits at the inner edge of the disk have less angular momentum, which means they can be torqued with less force. The negative inclination gradient, is therefore, a

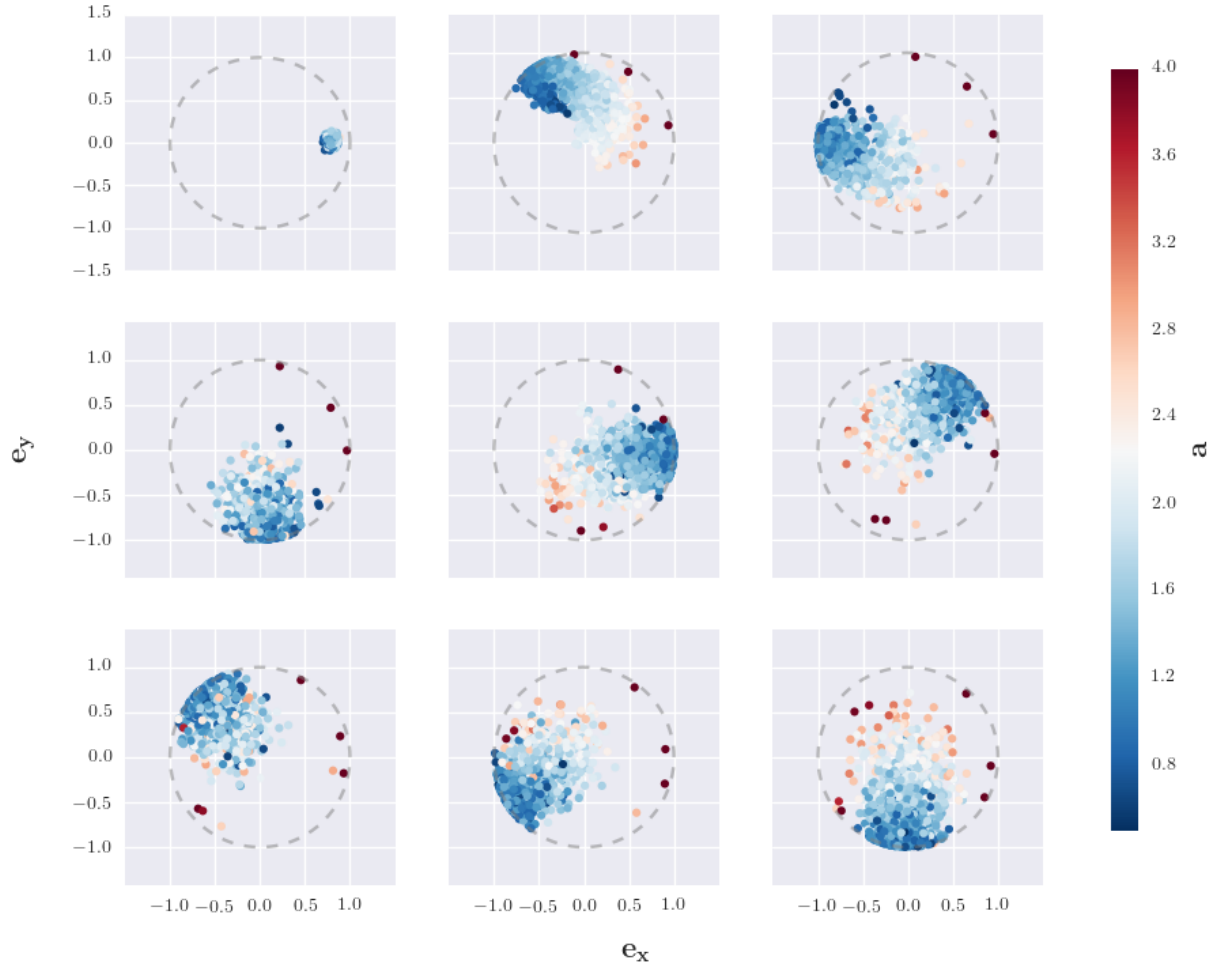

Figure 1.11: **The eccentricity vectors of an eccentric nuclear disk evolving in time.** The eccentricity vectors of stars in an N-body simulation are plotted every 100 orbits (left to right, top to bottom) in e_x-e_y space. The grey dashed circled indicates values of $e = 1$. The stars are colored in semi-major axis. The bulk of the disk precesses together in prograde motion (counter-clockwise), while the outermost orbits precess with retrograde motion (clockwise). This figure was originally published in Madigan et al. (2018a).

natural result of the negative eccentricity gradient.

Figure 1.13 shows the precessing orbits of two stars from an N-body simulation presented in Madigan et al. (2018a). The plot depicts the stars' eccentricity versus longitude of pericenter, ϖ, through time (∼300 orbital periods). The longitude of pericenter is the sum of the longitude of the ascending node (Ω) and the argument of pericenter (ω). It measures the angle at which the orbit's pericenter would be if the orbit had 0° inclination. The inner

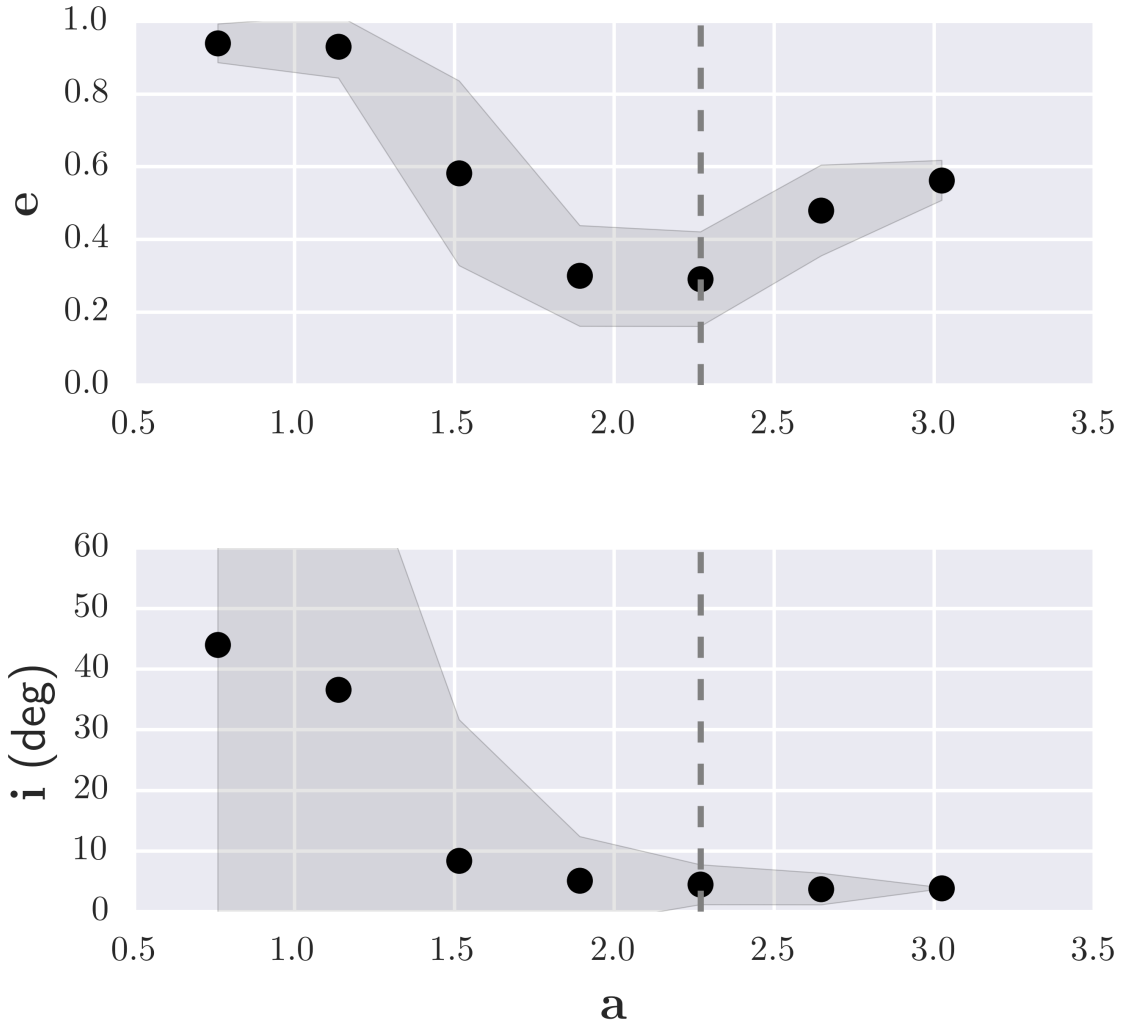

Figure 1.12: **The negative eccentricity and inclination gradients.** Top: the eccentricity gradient as a function of semimajor axis after 200 orbital periods. The mean eccentricity approaches unity at the inner edge of the disk. Bottom: the inclination gradient as a function of semimajor axis after 200 orbital periods. The grey regions show 1σ standard deviation. The vertical dashed lines divide the prograde precessing bulk of the disk and the retrograde precessing outer disk. This figure was originally published in Madigan et al. (2018a).

orbit oscillates with counterclockwise motion. When it is ahead of the disk ($\varpi - \langle\varpi\rangle > 0$), its eccentricity increases and the orbital precession slows. Similarly, when it is behind the disk ($\varpi - \langle\varpi\rangle < 0$), it becomes more circular and precesses more quickly. The outer orbit precesses with retrograde motion, oscillating in eccentricity as it encounters and moves past the inner disk.

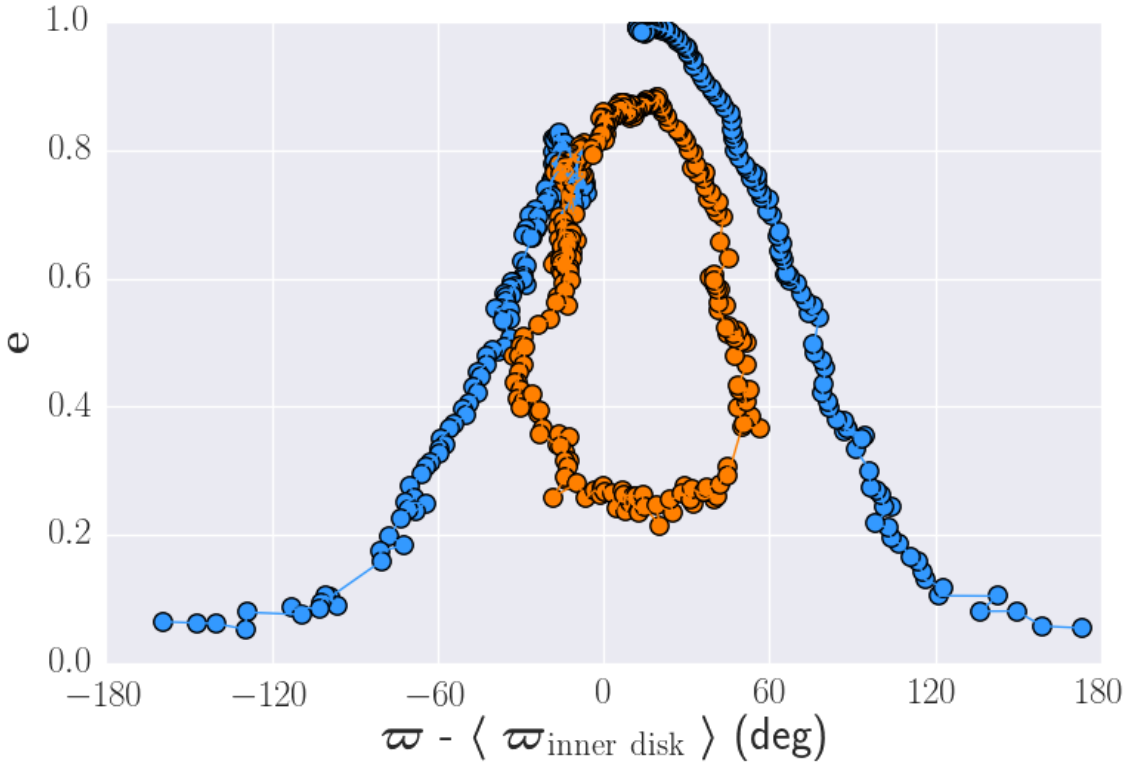

Figure 1.13: **Oscillations of orbits.** Evolution data for two stars over 300 orbital periods. The inner, orange, orbit oscillates with counter-clockwise motion about the main body of the disk. The outer, blue, orbit precesses with clockwise motion as it moves past the inner disk. This figure was originally published in Madigan et al. (2018a).

1.3.5 Tidal Disruption Events from Eccentric Nuclear Disks

As an eccentric nuclear disk stays stable, the orbits undergo oscillations in eccentricity. If we consider the case of the orbit ahead of the disk becoming more eccentric, and allow it to become highly eccentric, it may cause a star on the orbit to be tidally disrupted as it goes through pericenter. Stars will tidally disrupt if during their orbital oscillations, their eccentricities approach a value of one. A "TDE threshold" is calculated in Madigan et al. (2018a) as:

$$\frac{\delta e}{1-e} \sim \sqrt{\frac{e(1+e)}{(1-e)}}\phi_{\rm disk}^{-3/2}\ \delta i_e. \tag{1.13}$$

Here, e is the initial eccentricity of the orbit, δe is the magnitude of the eccentricity oscillation, $\phi_{\rm disk}$ is the angular width of the disk in radians, and δi_e is the amplitude of oscillation.

Whenever the TDE threshold is $\frac{\delta e}{(1-e)} \gtrsim 1$, the disk will rapidly produce tidal disruption events. Equation 1.13 is plotted as a function of eccentricity in Figure 1.14. The TDE

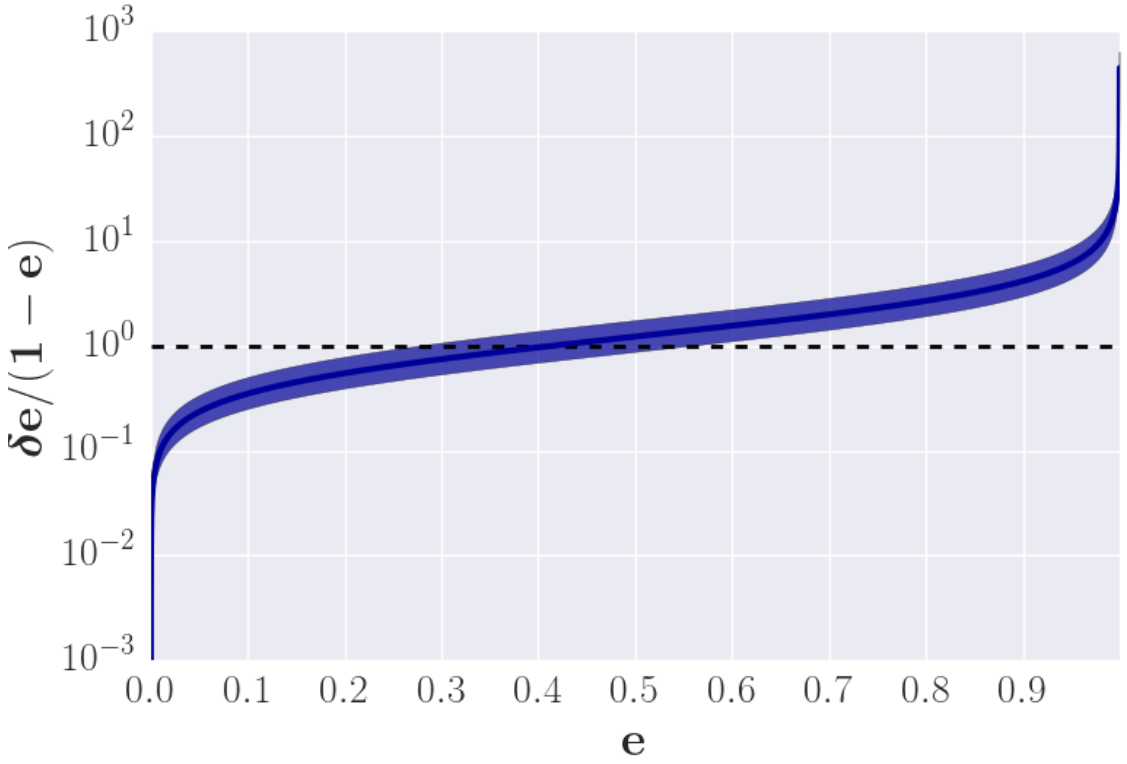

Figure 1.14: **TDE threshold.** Equation 1.13 plotted as a function of eccentricity. The dashed line is at $\frac{\delta e}{(1-e)} = 1$. Stars with equilibrium (unperturbed) eccentricities $\gtrsim 0.6$ could result in TDEs. This figure was originally published in Madigan et al. (2018a).

threshold is met whenever the orbits have equilibrium (unperturbed) eccentricities $e \gtrsim 0.6$. When the orbits have equilibrium eccentricities $e \gtrsim 0.9$, they greatly surpass the TDE threshold. Figure 1.15 shows the eccentricity versus time evolution of a handful of stars with large equilibrium eccentricities (starting at $e = 0.8$). Within just two precession periods, all five stars are torqued to extreme eccentricities $(1 - e) < 10^{-5}$.

Disrupting the inner-most stars will not deplete the supply of stars to be disrupted, as the gravitational torques due to secular dynamics are much more efficient at refilling the loss cone than two-body relaxation, which has typically been used to determine TDE rates. Since each TDE removes mass from the system, but not angular momentum, it does

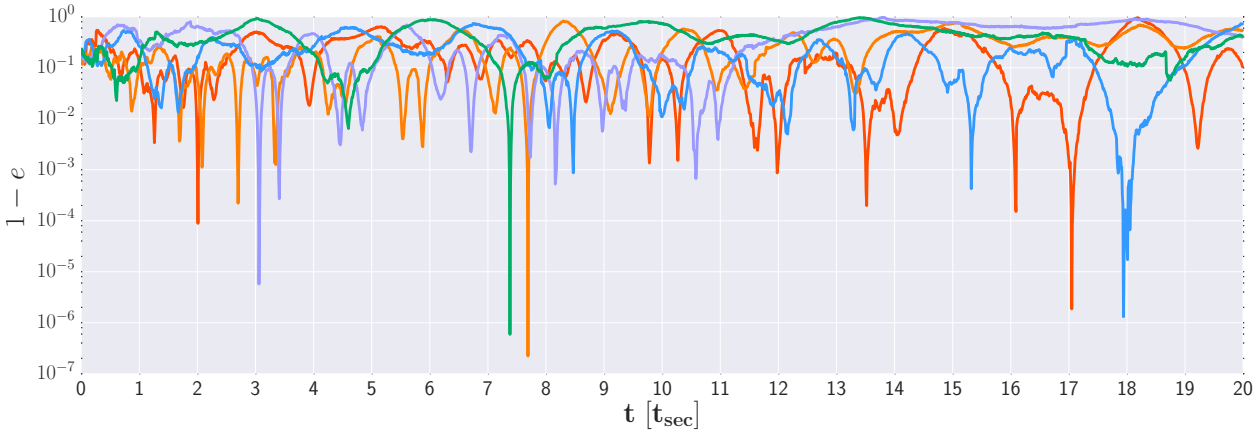

Figure 1.15: **High stellar eccentricities.** The eccentricity evolution of several stars in an eccentric nuclear disk. The stars begin with an eccentricity of 0.8, but are torqued to extreme eccentricities ($1 - e < 10^{-4}$). Time on the x-axis is shown in terms of the secular timescale ($t_{\rm sec} = \frac{M_\bullet}{M_{\rm disk}} P$). $t_{\rm sec} = 100P$ for this simulation. This figure was originally published in Madigan et al. (2018a).

indicate that the mean eccentricity will slowly decrease with time, eventually dipping below the TDE threshold. If, however, the eccentric nuclear disk was embedded in a star cluster, background stars could join the structure, replenishing the disk's mass, and prolonging the phase of elevated TDE rates. When the inner edge of a disk does drop down to $e \lesssim 0.6$ (below the TDE threshold), tidal interactions are greatly reduced and the eccentric disk structure fossilizes, producing what we likely see in M31. Once a stable eccentric disk forms, it should persist until either the background potential changes, or the galaxy undergoes another merger.

We propose that one of the main causes of TDEs is secular torques in eccentric nuclear disks (Madigan et al. 2018a). Hopkins & Quataert (2010a,b) show that eccentric nuclear disks could be formed through the merging of two galaxies, meaning that it would be likely to find eccentric nuclear disks in K+A/E+A galaxies. TDE rates in eccentric nuclear disks could be as high as $0.3 - 3$ yr^{-1} gal^{-1} at early times in the life of the disk (Madigan et al. 2018a). Several other methods have been theorized to explain the enhanced TDE rates in K+A/E+A galaxies. One of these theories is an enhanced rate due to supermassive black

hole binaries after the starburst. Chen et al. (2011) show that the TDE rate should scale weakly with the supermassive black hole mass ratio. This would indicate that TDEs would be seen primarily after minor mergers. TDEs are preferentially observed, however, in mergers with a more equal supermassive black hole mass ratio, indicating that the TDE rate is not driven by supermassive black hole binaries (French et al. 2017). Another theory involves more dense spherical star clusters resulting in enhanced two-body relaxation (Stone & van Velzen 2016).

1.4 The Scattered Disk in the Outer Solar System

The secular dynamics of eccentric orbits in galactic nuclei are directly related to the secular dynamics of eccentric orbits in planetary systems. Beyond Neptune ($a = 30$ AU), our Solar System is populated with small, icy minor planets. These icy bodies are on eccentric orbits and form a scattered disk structure. We can study the orbits in an axisymmetric near-Keplerian disk just as we do for eccentric nuclear disks.

An axisymmetric near-Keplerian disk of eccentric orbits will undergo a dynamical instability known as the "inclination instability." The inclination instability is driven by the collective gravity of the bodies in the axisymmetric disk of eccentric orbits. The orbits collectively grow in inclination and cluster in argument of pericenter (ω). They coherently tilt out of the disk plane, lifting into the shape of a bowl or cone (Madigan & McCourt 2016; Madigan et al. 2018b).

Clustering in ω is a unique signature of the inclination instability. Trujillo & Sheppard (2014) report that this same clustering exists in the icy minor planets with large pericenters beyond Neptune. Batygin & Brown (2016) hypothesize that a large planet, named Planet 9, exists beyond Neptune. Planet 9 would perturb the orbits of extreme trans-Neptunian objects (eTNOs) so that they are apsidally clustered. The self-gravity of the orbits, however, apsidally cluster without the need for a large planet beyond Neptune (Madigan & McCourt 2016; Madigan et al. 2018b). The inclination instability requires that about 20 Earth masses

exist in the outer Solar System between 100 and 1000 AU (Zderic & Madigan 2020). This is a larger, but similar mass to what is predicted for Planet 9.

We are interested not only in the clustered planets in the outer Solar System, but in the potential for observing clustering in exoplanetary systems as they should also undergo the inclination instability and form apsidal clustering. In Chapter 4 we present photometric (surface density) and kinematic (line-of-sight velocity) plots of an axisymmetric scattered disk. We show that apsidal clustering (an eccentric nuclear disk) is long-lasting in a primordial scattered disk that includes the gravitational influence of the giant planets after the inclination instability has saturated.

1.5 Summary of the Following Thesis Work

In Madigan et al. (2018a) we simulate eccentric nuclear disks in Newtonian gravity. Rapid apsidal precession due to general relativity, however, can quench secular dynamical mechanisms; a well-known example of this is the Kozai-Lidov effect (Ford et al. 2000; Blaes et al. 2002; Naoz et al. 2013). Resonant relaxation in a spherical cluster also gets quenched by general relativistic precession because the orbits move too rapidly to allow torques to build up (Rauch & Tremaine 1996). Similarly, one might expect general relativistic precession to disrupt the secular torques of the eccentric nuclear disk, greatly decreasing the TDE rate.

Presented here, we explore the effects of general relativity on the number of TDEs occurring in eccentric nuclear disks. We also quantify the distribution of orbital elements of TDEs that originate in eccentric nuclear disks. We do this using N-body simulations with and without general relativity. The novelty of these simulations is that we include self-gravity as well as general relativity. When self-gravity is not included, inclination flips, retrograde or counter-rotating orbits, and TDEs will be missed, all of which are fascinating and extremely important events for observers and dynamicists working to explain the structure and evolution of eccentric nuclear disks. We compare the number of TDEs that occur with and without general relativity and we track the orbital elements of a single tidally dis-

rupted star in order to show how quickly the orbit is torqued to an extreme eccentricity. We explore the unique orbital elements of tidally disrupted stars from eccentric nuclear disks, including the penetration factor, inclination distribution, and change in orientation between TDEs.

As eccentric nuclear disks are found in the centers of galaxies, they are very difficult to resolve. We explore what these disks should look like when observed from many different orientations and resolutions. There is plenty of evidence that these disks are common so we explain what observers should expect to see. In doing so, we create both photometric and kinematic maps of simulated eccentric nuclear disks. We also explore the effects of stellar mass segregation on the observed photometry. Radial mass segregation is a well-known process that occurs in stellar systems, including eccentric nuclear disks (Foote et al. 2020), affecting what will be observed.

Finally, we apply our work to the scattered disk in the outer Solar System. The dynamics that we explore in the context of galactic nuclei turn out to be directly relevant to planetary systems. The collective self-gravity of outer solar system bodies (in an axisymmetric near-Keplerian disk) results in apsidal clustering of the orbits. Apsidal clustering is simply an eccentric nuclear disk. We explore the dynamical formation of an eccentric nuclear disk in the outer Solar System by creating photometric and kinematic maps of the scattered disk.

Chapter 2

The Effect of General Relativistic Precession on Tidal Disruption Events from Eccentric Nuclear Disks

An eccentric nuclear disk consists of stars moving on apsidally-aligned orbits around a central black hole. The secular gravitational torques that dynamically stabilize these disks can also produce tidal disruption events (TDEs) at very high rates in Newtonian gravity. General relativity, however, is known to quench secular torques via rapid apsidal precession.

Here we show that for a disk to black hole mass ratio of $M_{\rm disk}/M_\bullet \gtrsim 10^{-3}$, the system is in the full loss cone regime. The magnitude of the torque per orbital period acting on a stellar orbit means that general relativistic precession does not have a major effect on the dynamics. Thus we find no evidence that TDE rates from eccentric nuclear disks in the full loss cone regime are affected by general relativistic precession. Furthermore, we show that orbital elements between successive TDEs from eccentric nuclear disks are correlated, potentially resulting in unique observational signatures.

This chapter reproduces Wernke & Madigan (2019).

2.1 Introduction

A tidal disruption event (TDE) occurs when a star is violently ripped apart by a black hole's tidal forces (Hills 1975). When a star is tidally disrupted, roughly half of the stellar debris remains bound to the black hole while the other half of the debris escapes. The gravitationally bound debris forms an accretion disk which feeds the black hole, producing a

flare (Rees 1988). The current detection rate of flares from TDEs is about two per year (van Velzen 2018) and this is expected to increase with new surveys such as the Large Synoptic Survey Telescope (LSST) (van Velzen et al. 2011).

TDE flares can provide insight into the mysteries of many areas of astrophysics. They illuminate central black holes in otherwise quiescent galaxies (Maksym et al. 2013; MacLeod et al. 2014). We can use their observations to test theories of accretion physics and relativistic jets (Zauderer et al. 2011; Bloom et al. 2011; van Velzen et al. 2016; Alexander 2017). Tidal disruptions of white dwarfs should even produce gravitational waves detectable by the Light Interferometer Space Antenna (LISA) (Zalamea et al. 2010; MacLeod et al. 2014). Additionally, we can test our understanding of gravitational stellar dynamics near supermassive black holes by comparing theoretical TDE rates with observations. We begin by introducing loss cone dynamics which are important in understanding how general relativistic precession in eccentric nuclear disks could cause TDE rates to vary.

2.1.1 Loss cone dynamics

The rate of TDEs due to stellar two-body relaxation has been studied extensively (Frank & Rees 1976; Lightman & Shapiro 1977; Shapiro & Marchant 1978; Cohn & Kulsrud 1978; Stone & Metzger 2016). Two-body relaxation is the diffusive process by which stars exchange energy and angular momentum amongst themselves, sometimes scattering a star onto a tidally disrupting orbit. It is faster to reach such an orbit by diffusion in angular momentum than in energy (Frank & Rees 1976).

In order for a star in these systems to get close enough to the supermassive black hole (SMBH) to tidally disrupt, it must enter the loss cone. The loss cone defines the region containing orbits with pericenters inside the tidal disruption radius of the black hole. The tidal disruption radius is:

$$r_t = \left(\frac{M_\bullet}{M_*}\right)^{1/3} R_*, \tag{2.1}$$

where $M_\bullet$ is the mass of the black hole, M_* is the mass of the star, and R_* is the radius of the star (Rees 1988). Orbits within the loss cone have angular momenta less than the angular momentum of an orbit with a pericenter equal to the tidal radius,

$$J < J_{\rm LC} \approx \sqrt{2GM_\bullet r_t}. \tag{2.2}$$

There are two loss cone regimes, defined by the parameter q,

$$q = \left(\frac{\Delta J_{\rm P}}{J_{\rm LC}}\right)^2, \tag{2.3}$$

where $\Delta J_{\rm P}$ is the change in angular momentum per orbital period (Lightman & Shapiro 1977). If $q \ll 1$, stars take multiple orbital periods to enter the loss cone. This is known as the empty loss cone regime or the diffusion limit because the time for a star to enter the loss cone is greater than the time for the star to be destroyed. If $q \gg 1$, stars can jump into and out of the loss cone within one orbital period. This is known as the full loss cone regime or the pinhole limit, because the loss cone is continuously populated by stars. The division between the two loss cone regimes for a spherical nuclear star cluster lies close to the radius of influence of the black hole (Lightman & Shapiro 1977). The TDE rate, in this case, is also dominated by stars coming from this region.

2.1.2 Status of observations of TDEs

In deriving theoretical TDE rates, we typically assume that stars come from an isotropic, spherical distribution around the black hole and are driven to the black hole through two-body relaxation (Wang & Merritt 2004; Stone & Metzger 2016). Many TDE rates have been calculated theoretically for spherical nuclear star clusters. For example, Wang & Merritt (2004) calculate a TDE rate of 2.1×10^{-4} yr^{-1} gal^{-1}, and more recently Stone & Metzger (2016) calculate a rate of 2.0×10^{-4} yr^{-1} gal^{-1}. In observations, however, TDEs are preferentially found in post-merger or post-starburst galaxies (K+A/E+A galaxies) at much higher rates (Arcavi et al. 2014). K+A/E+A galaxies are a relatively rare subtype of elliptical

galaxy that underwent a major starburst about 1-1.5 Gyr ago (Couch & Sharples 1987; Poggianti 2004). K+A/E+A galaxies make up 0.2% of the galaxies in the local universe, and yet, the observed TDE rates in these K+A/E+A galaxies are $1 - 3 \times 10^{-3}$ yr^{-1} gal^{-1}, which pushes the observed TDE rate of 'normal' galaxies down to $1 - 5 \times 10^{-6}$ yr^{-1} gal^{-1} (French et al. 2016). There is even (tentative) evidence that the TDE rate could be as high as 10^{-1} yr^{-1} gal^{-1} in ultra-luminous infrared galaxies (ULIRGs), which are typically in the process of merging (Tadhunter et al. 2017; Dou et al. 2017). We learn from these observations that merging galaxies and post-merger galaxies tend to have elevated TDE rates.

Several dozen TDE candidates have been identified in the last two decades, from UV/optical to X-ray. TDE candidates are generally identified as flaring events, inconsistent with supernovae, at the centers of galaxies. Candidates are typically excluded if the host galaxy shows signs of AGN activity. There have been a number of alternative ideas to explain these flaring events at galactic centers. Proposed TDE impostors include supernovae in AGN disks and black hole accretion disk instabilities (Saxton et al. 2016). One distinguishing feature that can be used to discriminate between real TDEs and impostors is the critical black hole mass beyond which a TDE will not be observable, known as the Hills mass (Hills 1975). The Hills mass results from the fact that the tidal radius and Schwarzschild radius of a black hole scale differently with mass of the black hole. The Schwarzschild radius is given by

$$r_s = \frac{2GM_\bullet}{c^2}, \tag{2.4}$$

where G is the gravitational constant and c is the speed of light. Equating the tidal radius to the Schwarzschild radius yields a Hills mass of $\sim 10^8 M_\odot$ for a solar-type star. Above this limit, the star plunges into the black hole without emitting a flare. A rapidly spinning black hole can raise this limit to $\sim 10^9 M_\odot$ (Kesden 2012). Recently, van Velzen (2018) presented the black hole mass function of optical/UV-selected TDE candidates and showed a sharp decrease in the number of candidates above $M_\bullet = 10^{7.5} M_\odot$. This is consistent with the direct

capture of stars when the black hole is above the Hills mass and provides strong evidence that we are seeing TDEs rather than impostors.

2.1.3 Secular dynamics and eccentric nuclear disks

Two-body relaxation is not the only form of relaxation present in galactic nuclei. Resonant relaxation[1] arises in near-Keplerian potentials (Rauch & Tremaine 1996). In resonant relaxation, a particle on a near-Keplerian orbit traces out the same path repeatedly. On a timescale less than the precession timescale, the orbits remain ∼fixed, and exert mutual gravitational torques on each other. Thus, the angular momentum relaxation can be greatly enhanced, while the energy relaxation is unaffected (Rauch & Tremaine 1996).

Resonant relaxation is most effective for stars orbiting close to the central supermassive black hole (in the absence of general relativity). This means that in an isotropic, spherical stellar distribution, where TDEs come most often from near the radius of influence, resonant relaxation will not greatly increase the rate or number of TDEs (Rauch & Ingalls 1998). Not all galactic nuclei, however, are ∼spherical like our galactic center. The nucleus of our nearest galactic neighbor, Andromeda (M31), has a very different configuration.

The Andromeda Galaxy (M31) has an elongated nucleus that resolves into two distinct brightness peaks. The double-nucleus can be explained by a thick, apsidally-aligned eccentric nuclear disk of Keplerian orbits around a SMBH (Tremaine 1995). The two brightness peaks correspond to apoapsis and periapsis of the eccentric nuclear disk.

While the central disk in M31 may seem like an unusual and unlikely arrangement, the fact that we see it in our closest major galaxy suggests that it is a common configuration. In fact, despite observational challenges, Lauer et al. (2005) found that about 20% of nearby, early-type galaxies have features consistent with eccentric nuclear disks seen from different angles on the sky.

[1] Note that this is a secular (orbit-averaged) effect; 'resonant' here refers to the resonance between the azimuthal and radial frequency of a Kepler orbit.

2.1.4 TDEs from eccentric nuclear disks

The stability of eccentric nuclear disks has long been a mystery. One would expect that the apsidal precession of individual orbits would spread out the disk into an axisymmetric structure on a timescale much shorter than the age of the stars (Tremaine 1995). In a recent paper (Madigan et al. 2018a), we proposed that the same secular mechanism that stabilizes eccentric nuclear disks is responsible for producing high rates of TDEs.

In Madigan et al. (2018a), we explain that the forces that cause precession in eccentricity vectors also result in a build-up of gravitational torques between orbits. These torques change the eccentricities of individual orbits as they are perturbed ahead of, or behind, the disk. Differential precession driven by these eccentricity changes holds the disk together. We also showed in Madigan et al. (2018a) that the orbits in an eccentric nuclear disk undergo oscillations in eccentricity. During the high eccentricity phase of an oscillation, a star can be tidally disrupted as it moves through pericenter. The gravitational torques due to secular dynamics are much more efficient at refilling the loss cone than two-body relaxation (Madigan et al. 2018a), which has typically been used to determine TDE rates. We proposed that secular torques in eccentric nuclear disks can produce the observed high rate of TDEs in K+A/E+A galaxies (Madigan et al. 2018a). Hopkins & Quataert (2010a,b) show that eccentric nuclear disks can form via the merging of gas-rich galaxies, meaning that it would be likely to find eccentric nuclear disks in post-merger, K+A/E+A galaxies. TDE rates in eccentric nuclear disks could be as high as ~ 1 yr^{-1} gal^{-1} at early times in the life of the disk (Madigan et al. 2018a).

Several other mechanisms have been theorized to explain the enhanced TDE rates in K+A/E+A galaxies. One of these theories is an enhanced rate due to SMBH binaries after the starburst. Chen et al. (2011) show that the TDE rate should scale weakly with the SMBH mass ratio. This would indicate that TDEs would be seen primarily after minor mergers, which are more common. TDEs are preferentially observed, however, in mergers with a

more equal SMBH mass ratio, indicating that the TDE rate is not driven by SMBH binaries (French et al. 2017). Another theory to explain the enhanced TDE rates in K+A/E+A galaxies involves more dense spherical star clusters resulting in enhanced two-body relaxation (Stone & van Velzen 2016; Stone et al. 2018).

2.1.5 This work

In Madigan et al. (2018a), we evolved eccentric nuclear disks with N-body simulations in Newtonian gravity. We showed that the secular torques in eccentric nuclear disks result in extremely high TDE rates. This previous work did not include rapid apsidal precession due to general relativity, however, which can quench secular dynamical mechanisms. A well-known example of this is the Kozai-Lidov effect which can be quenched by general relativistic precession as low angular momentum orbits apsidally precess too fast for the gravitational torques to build up (Lidov 1962; Kozai 1962; Ford et al. 2000; Blaes et al. 2002; Naoz et al. 2013). Resonant relaxation in a spherical cluster also gets quenched at low semi-major axes by general relativistic precession as the orbits move too rapidly to allow torques to build up coherently (Rauch & Tremaine 1996; Madigan et al. 2011).

Similarly, one might expect general relativistic precession to disrupt the secular torques of the eccentric nuclear disk, greatly decreasing the TDE rate. As eccentricity increases due to secular torques, the general relativistic precession rate also increases as given by the orbit-averaged precession rate due to general relativity:

$$\dot{\omega}_{GR} = \frac{6\pi G M_\bullet}{a c^2 \left(1 - e^2\right)}. \tag{2.5}$$

Equation 2.5 is a first order post-Newtonian approximation in general relativity yielding corrections to Newtonian accelerations of $\mathcal{O}(v^2/c^2)$ (Einstein 1916). One would therefore expect eccentric orbits to precess ahead of the disk, escaping completely until joining back up on the other side and re-circularizing (Madigan et al. 2018a). In this case, general relativistic precession would completely shut down the resonant relaxation in the eccentric

nuclear disk and we would expect to see very few TDEs.

The goal of this work is to explore the effects of general relativity on TDEs occurring in eccentric nuclear disks, and to quantify the distribution of orbital elements of TDEs that originate in eccentric nuclear disks. We do this using N-body simulations with and without general relativity. We present the paper in the following manner: in Section 2.2 we describe the initial conditions and parameters for our simulations, and compare the number of TDEs that occur with and without general relativity. We track the orbital elements of a single tidally disrupted star in order to show how quickly the orbit is torqued to an extreme eccentricity. In Section 2.3 we explore the unique orbital elements of tidally disrupted stars from eccentric nuclear disks, including the penetration factor, inclination distribution, and change in eccentricity vector between TDEs. In Section 3.5 we summarize and discuss our results.

2.2 N-body Simulations of Eccentric Nuclear Disks with General Relativistic Precession

We run N-body simulations of eccentric nuclear disks with `REBOUND` (Rein & Liu 2012) and the `IAS15` integrator (Rein & Spiegel 2015). We implement general relativity as a post-Newtonian approximation with `REBOUNDX`[2] . In this paper, we show results from simulations with the following general disk parameters: N=100 stars[3] , each with an initial eccentricity of 0.8, a range of semi-major axes ($a = 1 - 2$) with a surface density of $\Sigma \propto a^{-2}$, Rayleigh distributed inclinations with mean 0.1°, and a disk mass of $10^{-2} M_\bullet$. We want to qualitatively understand the effects of general relativistic precession rather than obtain an exact number for the TDE rate.

In each of these simulations, we examine the effect that general relativity has on the

[2] https://github.com/dtamayo/reboundx

[3] In Madigan et al. (2018a), we used a range of $N = 100 - 1000$ stars. The Madigan et al. (2018a) simulations in Newtonian gravity gave the same qualitative results for the different N. Here we use $N = 100$ stars in order to reduce computing time.

number of tidal disruption events. The orbit-averaged precession rate due to general relativity is given by Equation 2.5. We track the general relativistic precession rate in our simulations by calculating the change in the orientation of the eccentricity vector at each time step.

A star is considered tidally disrupted if at any point in the simulation its radius $\leq r_t$. We treat stars as point masses and do not extract them from our simulation after they are disrupted, but they are counted only once as a TDE.

2.2.1 Effects of General Relativity

We find that the TDE rate with general relativistic precession is the same as in Newtonian gravity. About 12% of disk stars are tidally disrupted[4] for a $10^6 M_\odot$ black hole during a time of 1000 orbital periods, where each orbital period is roughly 1000 years. We have compiled results from ∼45 simulations with general relativistic precession and ∼100 simulations without general relativistic precession. The mean percent and standard deviation of tidally disrupted disk stars is shown in Figure 2.1. In an isotropic, homogeneous case, we would expect to see about 1% of disk stars tidally disrupted. We are focused, however, on comparing the number of TDEs in an eccentric nuclear disk with and without general relativistic precession. The number of TDEs is approximately equal for both general relativistic simulations and Newtonian simulations. This means that general relativistic precession does not shut down the secular torques in eccentric nuclear disks, as we initially expected.

In order to understand this, we track the orbital elements of a single star (with general relativistic precession) which suffers a tidal disruption event in Figure 2.2. We see a star that develops an eccentricity such that its orbital angular momentum is less than the loss cone angular momentum. The star also passes through pericenter while it is at a high eccentricity, meaning that the star is close enough to the black hole to be tidally disrupted.

[4] This percentage is smaller than in Madigan et al. (2018a) because we have a more rigorous TDE criterion and exclude partial disruptions from our analysis.

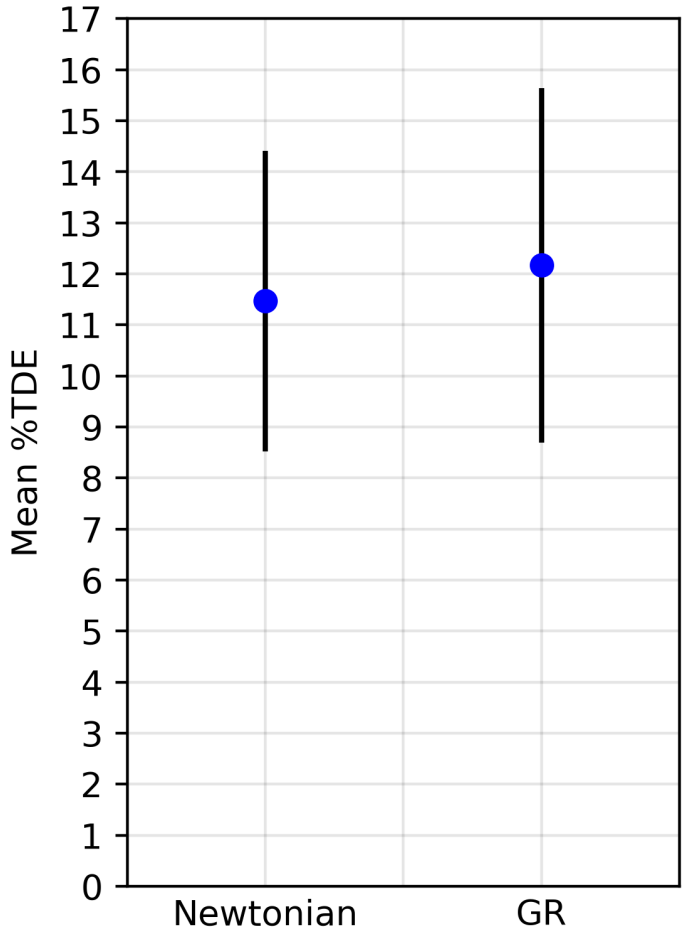

Figure 2.1: **Mean percent of disk stars tidally disrupted in Newtonian gravity and with general relativistic precession.** Here we see that eccentric nuclear disks with Newtonian gravity and with general relativistic precession each have a mean of roughly 12% of disk stars that tidally disrupt. The error bars show the standard deviation. By performing a Welch's t-test for a difference in means and obtaining a P-value of 0.255, we find that the means are not statistically different.

We also see that the star's orbital inclination flips by $\sim$180° as it reaches extreme eccentricity (see discussion in Section 2.3.2). Panel 4 shows the general relativistic precession rate, which we track by calculating the change of i_e in each time step. i_e tracks the orientation of the eccentricity vector in the plane of the disk and is given by

$$i_e = \arctan\left(\frac{e_y}{e_x}\right), \tag{2.6}$$

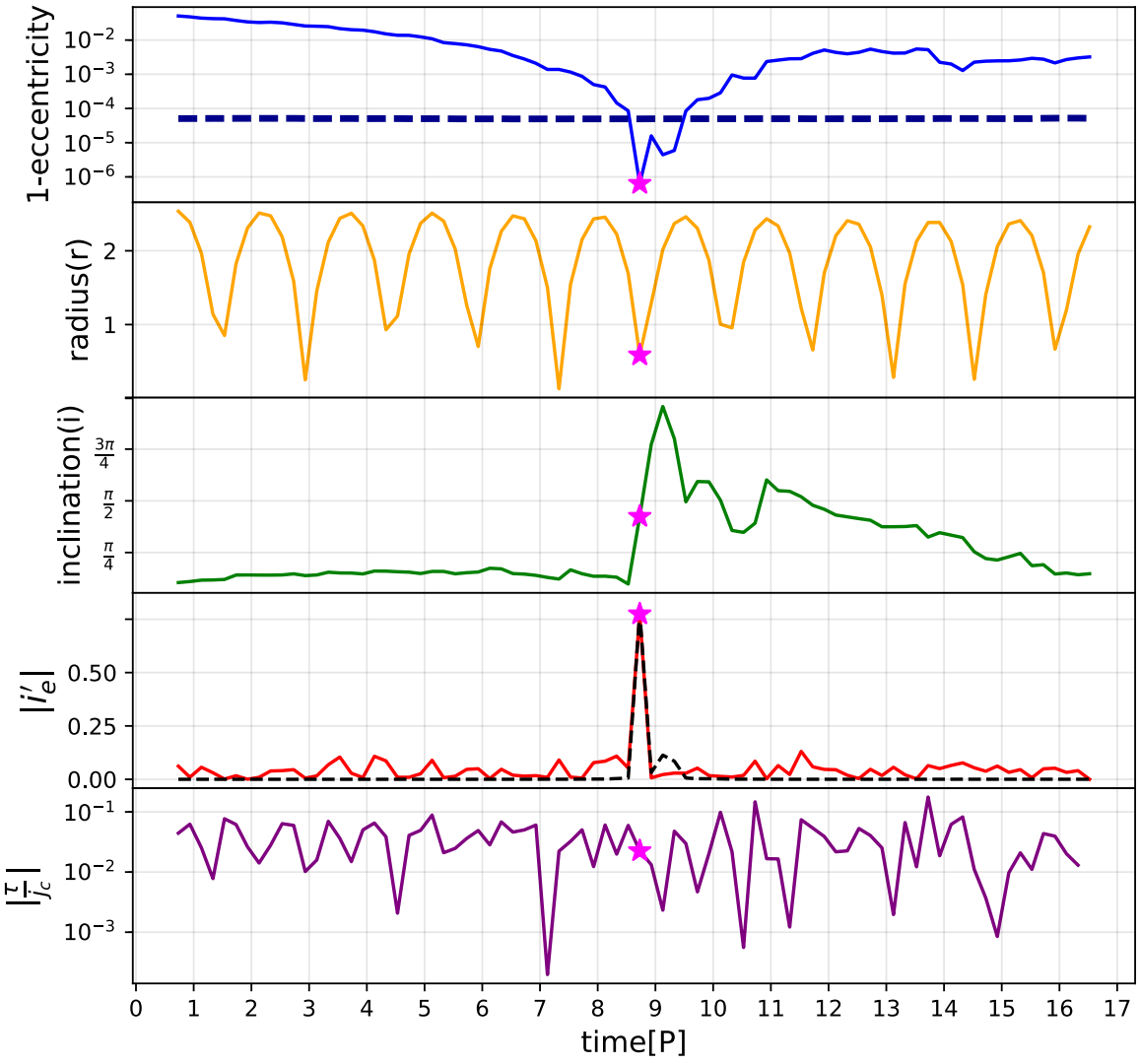

Figure 2.2: **A tidal disruption event (TDE) in an N-body simulation of an eccentric nuclear disk with general relativistic precession.** A star marks the point of tidal disruption in each panel. *Top panel:* the eccentricity of a star undergoing a tidal disruption event as a function of time in units of orbital periods (P). At the time of tidal disruption, the eccentricity increases from $\sim$0.999 to $>$ 0.9999 within one orbital period. The dashed line shows the $1-e$ value such that $J = J_{\rm LC}$. *Second panel:* the orbital radius (in code units) of the same star as a function of time. The star meets the requirement of being at pericenter to be tidally disrupted. *Third panel:* the inclination of this star flips by 180° at the same time it reaches an extreme eccentricity. *Fourth panel:* the general relativistic precession rate with the time derivative of the eccentricity vector (i'_e) in units of radians per orbital period. The black dashed line shows the analytic general relativistic precession rate ($\dot{\omega}_{GR}$) from Equation 2.5. General relativistic precession is effective for less than one orbital period, allowing the star to still tidally disrupt. The normalized torque required to produce a TDE is on the order of 10^{-2} per orbital period. *Bottom panel:* the normalized torque applied to the orbit of the star oscillates around 10^{-2} per orbital period, ensuring that even with general relativity, the tidal disruption event can occur.

(Madigan & McCourt 2016). Here e_x and e_y are the x and y components of the eccentricity vector. We use i_e instead of the argument of periapsis, ω, or the longitude of periapsis, ϖ, to avoid effects of changing inclination. As an orbit rolls over its major axis, the eccentricity vector remains close to the $x-y$ plane, even though the inclination grows. ω and ϖ, however, will change with the flipping inclination. We see that the rate of change of i_e is very small until the star reaches pericenter at an extreme eccentricity where there is a large jump due to general relativity. This jump in precession rate is only present for a fraction of an orbital period. The final panel of Figure 2.2 shows the torque acting on the orbit in units of the circular angular momentum which we explore in the next section.

2.2.2 Magnitude of Torque from Disk

Here we calculate the magnitude of the torque exerted on a typical orbit by the disk. The orbit is described by its specific angular momentum and energy

$$j^2 = GM_\bullet a\ (1 - e^2) \tag{2.7a}$$

$$E = \frac{GM_\bullet}{2a}. \tag{2.7b}$$

For an eccentric orbit, the specific torque is given by

$$\boldsymbol{\tau} = \boldsymbol{j}' = \boldsymbol{r} \times \boldsymbol{f}. \tag{2.8}$$

$\boldsymbol{r}$ is the orbital radius and $\boldsymbol{f}$ is the specific gravitational force felt by an orbit due to the rest of the disk. This force is defined by

$$|\boldsymbol{f}| = \frac{GM_{\rm disk}}{r^2}, \tag{2.9}$$

where $M_{\rm disk}$ is the mass of the eccentric nuclear disk. Approximating r by the semi-major axis a yields a torque

$$|\boldsymbol{\tau}| \approx \frac{GM_{\rm disk}}{a}. \tag{2.10}$$

Normalizing the torque by the circular angular momentum $\left(j_c = \sqrt{GM_\bullet a}\right)$ yields

$$\left|\frac{\boldsymbol{\tau}}{j_c}\right| \approx \frac{M_{\rm disk}}{M_\bullet}\frac{2\pi}{P}, \tag{2.11}$$

where $P = 2\pi\sqrt{a^3/GM_\bullet}$ is the orbital period. Hence, in our N-body simulations, in which $M_{\rm disk}/M_\bullet = 10^{-2}$, the normalized torque per orbital period should be on the order of 6×10^{-2}. The final panel in Figure 2.2 shows that indeed our example star experiences a torque of $\mathcal{O}(\text{few} \times 10^{-2})$. This magnitude of torque can change an orbit's eccentricity from $e \approx 0.998$ to $e \approx 1$ within one orbital period. That is, the change in angular momentum required to produce a TDE can occur within one orbital period, suggesting that our system is in the full loss cone regime. By assuming a $10^6 M_\odot$ black hole and a solar-type star, we find from Equation 2.3, that $q \approx 40$ in our simulations, putting the system well within the full loss cone or pinhole regime. This explains why general relativity is ineffective at shutting down the TDE production. In the full loss cone regime, a stellar orbit can be propelled from outside the loss cone to inside in less than an orbital period. General relativistic precession only acts strongly when the star approaches pericenter, at which point it is too late to avoid disruption.

Not all eccentric nuclear disks will be in the full loss cone regime. The transition from full loss cone to empty loss cone occurs when $q = 1$ such that

$$\frac{M_{\rm disk}}{M_\bullet} = \sqrt{\frac{r_t}{2\pi^2 a}}. \tag{2.12}$$

For a SMBH of $10^6 M_\odot$, solar-type stars, and a disk inner edge of $a = 0.05$ pc, we find that disks with $M_{\rm disk}/M_\bullet \geq 1.5 \times 10^{-3}$ are in the full loss cone regime. The M31 disk has an observed disk mass ratio of $\sim 10^{-1}$ (Tremaine 1995), putting it in the full loss cone regime.

2.3 Unique Orbital Elements

Two-body relaxation predicts that the time between individual TDEs ($\sim 10^4$ years) is much greater than the time it takes for a TDE disk to accrete onto the black hole. If stars

come from eccentric nuclear disks however, the typical timescale between individual TDEs can be much shorter (∼1-10 yr; Madigan et al. 2018a), and TDE disks could potentially overlap with one another. This could have interesting observational consequences especially if the orbital parameters of TDEs are correlated.

2.3.1 Penetration Factor

The strength of a tidal disruption may be quantified by the dimensionless penetration factor,

$$\beta = \frac{r_t}{r_p}, \tag{2.13}$$

where r_t is the tidal radius and r_p is the pericenter of the star's orbit (Press & Teukolsky 1977). In Figure 2.3 we show the distribution of penetration factors in our simulations.

If the penetration factor is greater than or equal to one, the star will be tidally disrupted. If the penetration factor is less than, but close to one, the star may have its outer layers stripped, with a stellar core remaining intact (Ivanov & Novikov 2001; Guillochon & Ramirez-Ruiz 2013; Bogdanović et al. 2014; Mainetti et al. 2017). If the penetration factor is too large however, the star will fall straight into the black hole without emitting an electromagnetic flare. This occurs when the $r_p < r_s$. For a non-spinning, $10^6 M_\odot$ black hole and solar-type stars this occurs at $\beta = 23.5$.

We see in Figure 2.3 that the probability distribution function, $P \propto \beta^{-2}$, is fully consistent with the full loss cone or pinhole regime (Lightman & Shapiro 1977). This is significant because the critical radius (where $q = 1$) is typically found near the radius of influence of the black hole. We find that eccentric nuclear disks bring the critical radius orders of magnitude within the radius of influence, to a radius smaller than the inner edge of the disk.

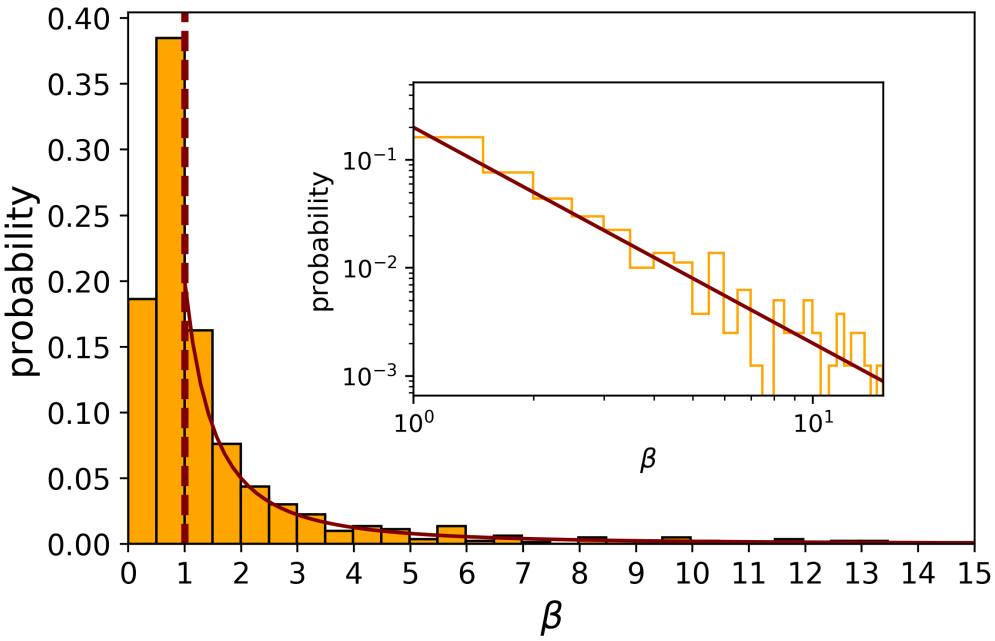

Figure 2.3: **The distribution of impact parameters with general relativity.** The dashed line shows the critical value of the impact parameter. A star with an impact parameter less than one will be tidally squeezed and stretched (many will even lose mass), but not fully disrupted. A disruption event with an impact parameter greater than 23.5 (corresponding to solar-type stars and a non-spinning $10^6 M_\odot$ black hole) will not be visible to observers because its pericenter is inside the Schwarzschild radius. We see in this figure that our results are consistent with the pinhole regime in which orbits have large steps in angular momentum, allowing stars to jump into the loss cone within an orbital period. The probability distribution function of the impact parameter is well-fit by the curve $\propto \beta^{-2}$, as shown by the solid maroon line. The inset shows the same histogram with the curve $\propto \beta^{-2}$ on a log-log scale.

2.3.2 Inclination Distribution

In a spherical, isotropic stellar system dominated by two-body relaxation, there should be no correlation between the orbital angular momentum vectors of consecutive TDEs, and so we would expect to see an isotropic distribution of TDE inclinations. This is quite different in the case that stars are originating in an eccentric nuclear disk.

We find that whenever a star reaches a high eccentricity in our simulations, it undergoes an inclination flip of 180°. Figure 2.4 is an example of a double peak in eccentricity

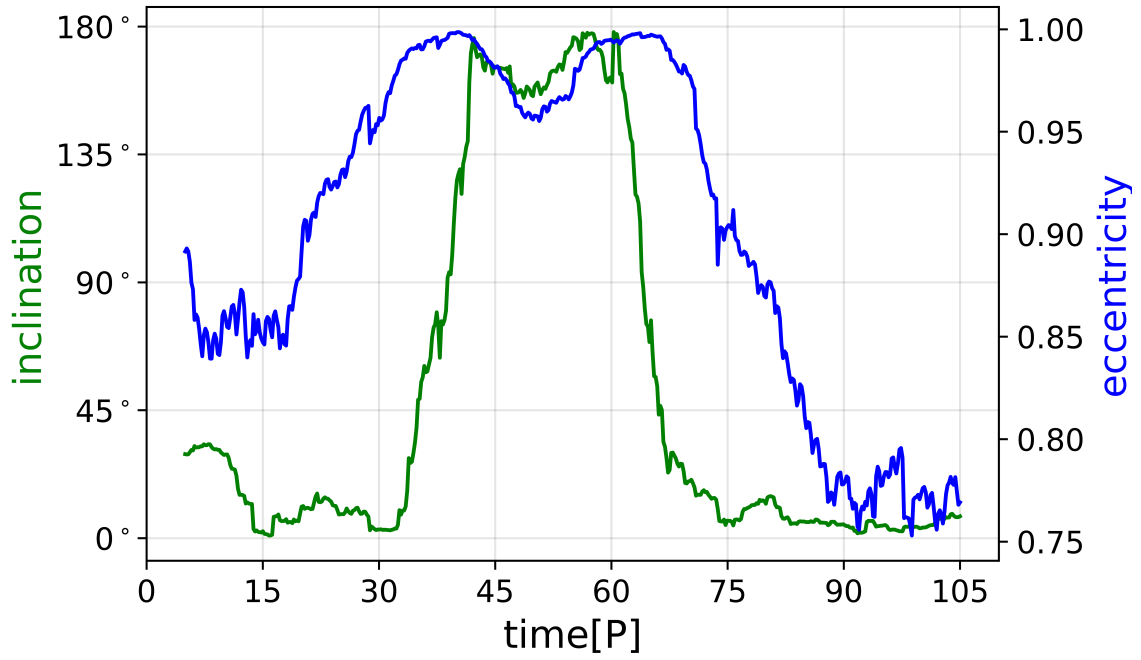

Figure 2.4: **The inclination flip of a star at high eccentricity.** The blue line shows the eccentricity of the star, while the green line shows the inclination of the orbit in radians. The inclination flips from 0° to 180° or vice versa, corresponding to the extreme peaks in eccentricity. An orbit with an inclination between 0° and 90° is prograde and an orbit with inclination between 90° and 180° is retrograde.

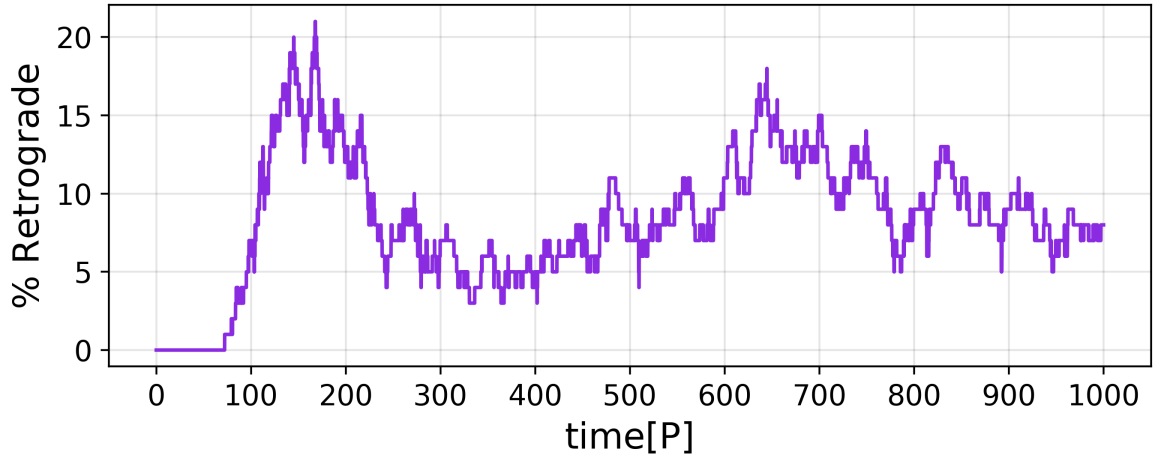

Figure 2.5: **The percentage of disk stars on retrograde orbits with time.** A typical plot of the changing percentage of retrograde orbits with time for a single simulation. The eccentric nuclear disk simulation begins with all orbits in a prograde orientation. The number of retrograde orbits climbs quickly after about 150 orbital periods to a peak of ∼20% retrograde and then oscillates around 10% retrograde for the rest of the simulation.

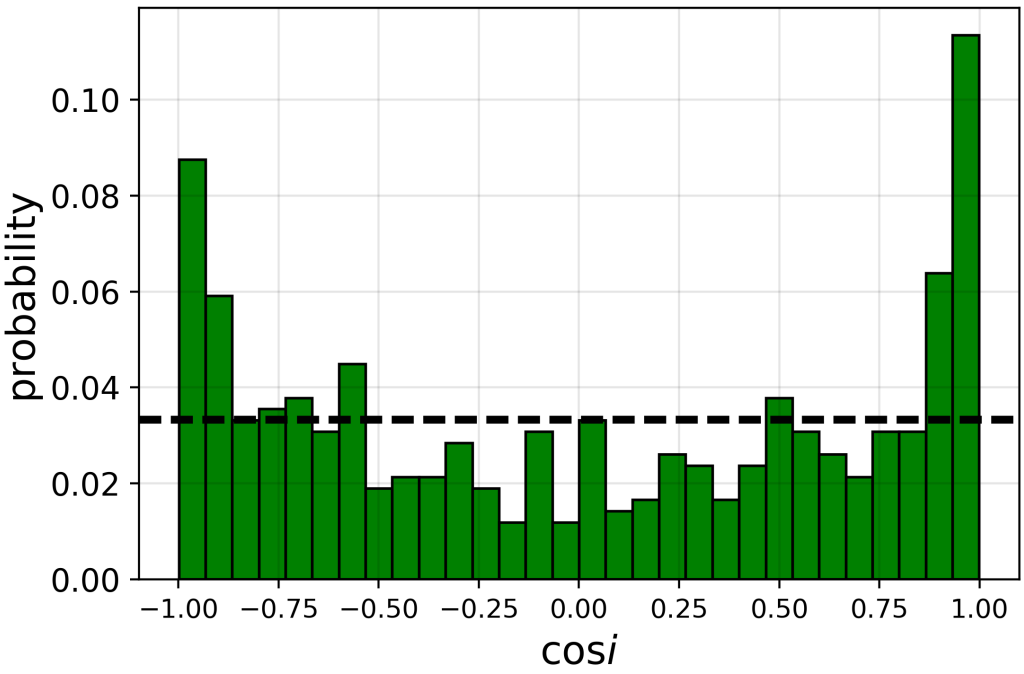

Figure 2.6: **The distribution of orbital inclinations of disrupted stars with general relativity.** The black dashed line shows the isotropic distribution of cosine of inclinations that we would see from a spherical cluster. Stars originating in an eccentric nuclear disk preferentially tidally disrupt at inclinations of 0° and 180°.

corresponding to a double 180° flip in inclination. As the orbit is negatively torqued by the disk to extreme eccentricity (in blue), its angular momentum vector decreases until it passes through zero. At this point, the inclination (in green) flips 180° and the orbit switches from a prograde orientation (with respect to the disk) to a retrograde orientation. The orbit now feels a positive torque causing it to circularize and precess quickly back towards the disk. On the other side of the disk, the angular momentum will again decrease, pass through zero and change direction. The orbit is prograde again after the second flip. These double peaks of inclination were also seen in our Newtonian simulations (Madigan et al. 2018a).

As the orbits flip from prograde to retrograde and back, the percentage of stars on retrograde orbits fluctuates throughout a given simulation. Figure 2.5 is an example of the percentage of retrograde orbits in a disk for a single simulation. Most of these retrograde orbits lie near the inner edge of the disk. There have been many kinematic studies of the

M31 disk which give differing precession values for the disk (Sambhus & Sridhar 2000; Bacon et al. 2001; Jacobs & Sellwood 2001; Salow & Statler 2001; Sambhus & Sridhar 2002; Salow & Statler 2004; Lockhart et al. 2018). Current dynamical models of the eccentric nuclear disk in M31 (e.g., Peiris & Tremaine 2003) do not include retrograde moving stars. Our results indicate that the stars on retrograde orbits could be very important for both observations and models.

The flipping of orbits in inclination results in an anisotropic distribution of TDE inclinations (see Figure 2.6). Stars preferentially tidally disrupt at orbital inclinations of 0° and 180° with respect to the disk mid-plane. More disruptions occur at 0°. This is because the stars get the first opportunity to disrupt at an inclination of 0°, while their orbit is ahead of the disk. The probability for a star to disrupt in one orbital period is

$$\begin{aligned} P_{\rm TDE} &= \frac{J_{\rm LC}}{\Delta J_{\rm P}} \\ &= \frac{1}{\sqrt{2}\pi}\sqrt{\frac{r_t}{a}}\left(\frac{M_\bullet}{M_{\rm disk}}\right). \end{aligned} \tag{2.14}$$

We estimate $a \approx 10^{-2}\ r_H$ for the inner edge of the disk, where r_H is the radius of influence of the black hole, based on the disks in M31 and the Galactic center (Madigan et al. 2018a). We take r_H to be 5pc from observations of the Galactic center (Lu et al. 2009). We find that $P_{\rm TDE} = 0.15$. Out of 100 stars vulnerable to disruption, ∼15 will tidally disrupt at an inclination of 0°. 85 stars will then flip inclinations and have a 15% chance (∼12-13) of tidally disrupting at an inclination of 180°. Therefore, we find that the number of TDEs at 180° is 85% the number at 0°, or in general,

$$N_{\rm TDE\ (i=180^\circ)} = (1 - P_{\rm TDE})\ N_{\rm TDE\ (i=0^\circ)}. \tag{2.15}$$

This explains the height difference that we see in the inclination distribution in Figure 2.6.

For a spinning Kerr black hole, the tidal and capture cross-sections shift towards negative angular momenta (Beloborodov et al. 1992). The asymmetric cross-sections make it easier for stars on retrograde orbits to be captured, meaning that prograde TDEs will be

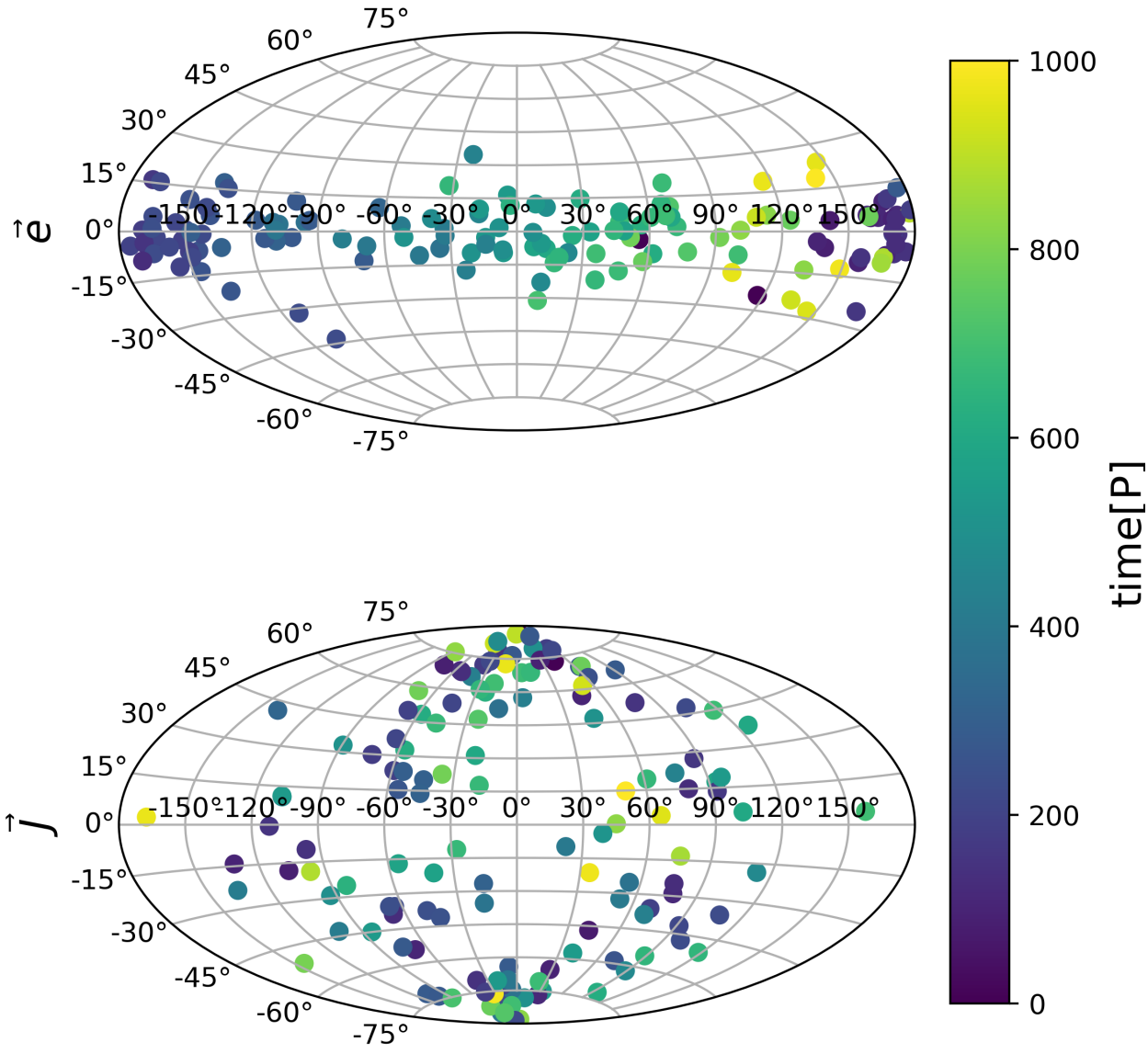

Figure 2.7: **Aitoff projection of eccentricity and angular momentum vectors of TDEs.** Colors indicate the time of TDE in units of orbital periods at the inner edge of the disk. *Top:* The eccentricity vectors, $\boldsymbol{e}$, precess together in a prograde direction, staying close to the mid-plane. The orbits start with their eccentricity vectors at about 60° and then precess together in a prograde direction (to the right on our projection plot). The first TDEs begin occurring after about 200 orbital periods, when the disk has precessed to ∼0°. When the orbits flip in inclination, they flip over the major axis instead of the latus rectum. *Bottom:* The spread in the angular momentum vectors, $\boldsymbol{j}$, with a majority at the poles, confirms that the orbits roll over their major axes.

preferentially observed. If the spin angular momentum vector of the black hole is aligned with the orbital angular momentum vector of the disk, then the preference for TDEs from eccentric nuclear disks to have $\sim 0^\circ$ orbital inclination puts them at the perfect orientation to be visibly disrupted by a Kerr black hole.

2.3.3 Eccentricity Vector

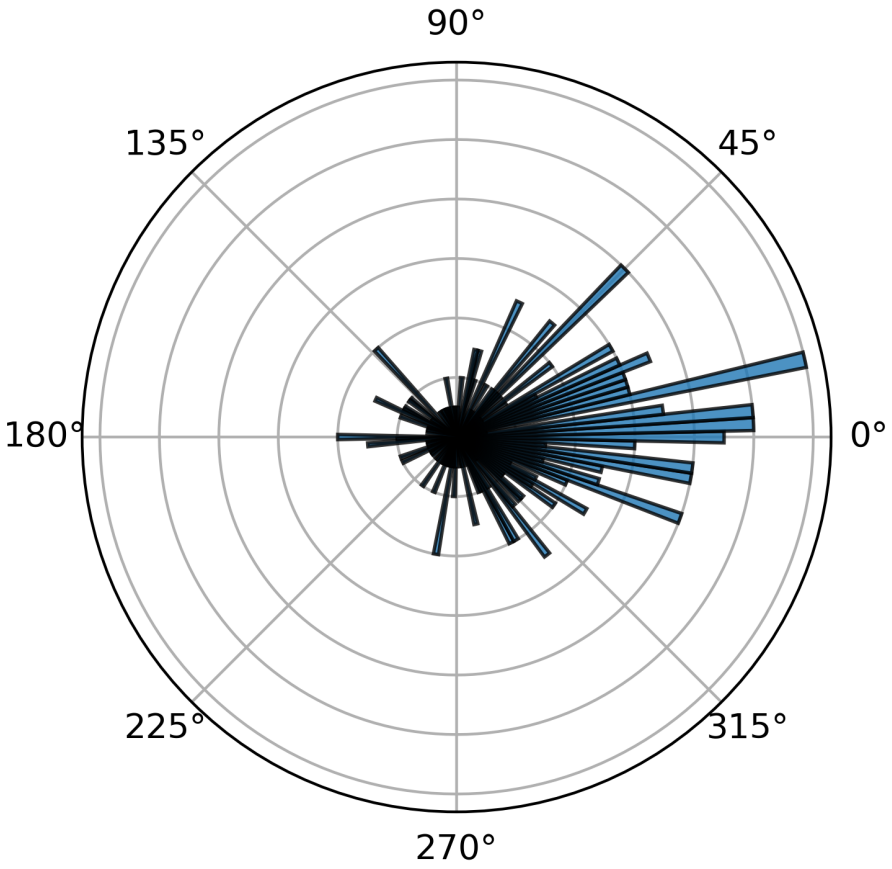

Figure 2.8: **The distribution of $\Delta\theta$ between TDEs.** A histogram of $\Delta\theta$ for consecutive TDEs with general relativistic precession. About 20% of the consecutive TDEs occur with a small ($\leq 20^\circ$), positive change in i_e. This is partially due to the prograde precession of the disk. The clustering of $\Delta\theta$ around 0 and slightly greater than 0 show that the first condition for tidal streams crossing is met for many consecutive TDEs. Prograde precession is in the positive (counter-clockwise) direction.

We plot the eccentricity vectors of tidally disrupted stars at the time of TDE in the top panel of Figure 2.7. The eccentricity vectors precess together in a prograde direction while

remaining in the plane. This means that when a stellar orbit flips in inclination, it flips over its major axis. The bottom panel of Figure 2.7 shows the angular momentum vectors of the same tidally disrupted stars at the time of TDE. The spread in angular momentum vectors confirms that the orbits roll over their major axes.

With TDEs preferentially occurring in the plane with inclinations of 0° or 180°, the debris streams from two sequential TDEs could cross and produce unique observational signatures. Bonnerot & Rossi (2019) derive the conditions necessary for a tidal stream crossing to occur, which depend on disk properties, tidal stream widths, and the time between consecutive TDEs. If the pericenter shift between tidally disrupted stars is positive, the time delay is small, and the inclination offset is less than the width of the tidal streams, crossing of the tidal streams could occur. While our simulations do not allow for the calculation of accurate time delays (due to the low N nature of our simulations) or stream width, we calculate the pericenter shift between two TDEs with an angle, $\Delta\theta$. This $\Delta\theta$ tracks the orientation of the orbit of the first TDE with respect to the orientation of the orbit of the second TDE. We track the orientation of the orbits in our simulation with i_e, defined in Equation 2.6. We therefore calculate $\Delta\theta$ between TDEs as

$$\Delta\theta = i_{e_2} - i_{e_1}. \tag{2.16}$$

We show, in Figure 2.8, a distribution of the $\Delta\theta$ between pairs of TDEs in our simulations. We see that about 20% of consecutive TDEs occur with a small ($\leq 20°$), positive $\Delta\theta$, satisfying one of the conditions for tidal streams crossing. We expect that this condition would be met due to prograde precession of the eccentric nuclear disk.

2.4 Discussion

This paper focuses on the dynamics of eccentric nuclear disks with general relativistic precession. In Madigan et al. (2018a), we showed that the same secular mechanism that keeps eccentric nuclear disks stable results in extremely high TDE rates. This work did

not include general relativity, however, which is known to quench secular torques via rapid apsidal precession. In this paper, we show that secular gravitational torques push the orbits of stars to extremely high eccentricities within one orbital period (full loss cone regime). This does not allow general relativistic precession enough time to suppress the TDE rate. The geometry of eccentric nuclear disks is key: the torques acting on an orbit from the rest of the disk stars are coherent. Our results point to the following conclusions and implications:

(1) General relativistic precession does not significantly affect the TDE rate from eccentric nuclear disks as stars at the inner edge of the disk are in the full loss cone regime. TDEs occur in simulations with general relativity approximately as often as they occur in Newtonian simulations.

(2) TDEs from eccentric nuclear disks do not follow an isotropic distribution of inclinations; they preferentially disrupt at inclinations of 0° and 180° with respect to the mid-plane of the disk. Overlapping TDE disks may have similar (or opposing) angular momenta that can build up (or cancel each other out).

(3) The probability of disrupting stars on prograde orbits is higher than the probability of disrupting stars on retrograde orbits for a non-spinning, Schwarzschild black hole in an eccentric nuclear disk. Similarly, the number of prograde captured stars (within the Schwarzschild radius so that a flare will not be observed), will also be greater than the number of retrograde captured stars for a non-spinning, Schwarzschild black hole.

(4) If an eccentric nuclear disk forms during a gas-rich major merger (Hopkins & Quataert 2010a,b), it is likely that the central gaseous accretion event that produces the disk aligns the disk angular momentum with that of the central SMBH. Spinning, Kerr black holes have asymmetric tidal and capture cross-sections (Beloborodov et al. 1992). For black holes with mass greater than the Hills mass, the only observable

TDEs are those on prograde orbits aligned with the black hole spin. *The preference for TDEs from eccentric nuclear disks to have* $\sim 0^\circ$ *orbital inclination puts them in the perfect orientation to be observably disrupted by such black holes.* There may be evidence of TDEs by extremely massive black holes already. ASSASN-15lh is a TDE candidate found in a galaxy with a central SMBH much more massive than the Schwarzschild Hills mass ($\sim 10^{8.24} M_\odot$) (Leloudas et al. 2016).

(5) In steady-state, eccentric nuclear disks have a non-negligible fraction of retrograde orbiting stars ($\sim$10%). Most of these will lie at the inner edge of the disk. This will lead to interesting observational signatures in the velocity moments of eccentric nuclear disks.

Finally, we look back to our nearest neighbor, Andromeda (M31). To date, no TDEs have been observed from its center. This may be due to the fact that the eccentric nuclear disk in M31 is very old, on the order of Gyr (Sil'chenko et al. 1998). Unless continuously replenished, an eccentric nuclear disk loses mass due to stars being destroyed by tidal forces, but it does not lose significant angular momentum. The disk, therefore, becomes less eccentric with time, causing the TDE rate to decrease (Madigan et al. 2018a). Another possible explanation for the absence of TDEs in M31 is that more massive stars have a greater chance of disrupting than less massive stars (due to their location in the eccentric nuclear disk; Foote et al. 2019, in prep.) and the more massive stars will die off first, causing the TDE rate to decrease with time. At $M_\bullet \simeq 1.4 \times 10^8 M_\odot$, the mass of the M31 black hole is also greater than the Hills mass (Bender et al. 2005). We should not expect to observe TDEs of solar-type stars, unless the black hole is spinning.

Chapter 3

Photometry and Kinematics of Self-Gravitating Eccentric Nuclear Disks

The Andromeda Galaxy hosts an elongated nucleus with (at least) two distinct brightness peaks. The double nucleus can be explained by the projection of a thick, apsidally-aligned eccentric nuclear disk of stars in orbit about the central black hole. Several nearby early-type galaxies have similar asymmetric nuclear features, indicating the possible presence of eccentric nuclear disks. We create simulated photometric (surface density) and kinematic (line-of-sight velocity) maps of eccentric nuclear disks using N-body simulations. We image our simulations from various lines of sight in order to classify them as double nuclei, offset nuclei, and centered nuclei. We explore the effects of mass segregation on the photometric maps, finding that heavier stars are concentrated in the brighter peak. The average line-of-sight velocity values are lower in an eccentric nuclear disk than for a circular ring about the supermassive black hole. The velocity dispersion values are higher and peak at the position of the supermassive black hole, which does not typically match the peak in photometry.

This chapter reproduces Wernke & Madigan (2021).

3.1 Introduction

The elliptical nucleus of M31 was first resolved by the balloon-borne Stratoscope II telescope, which showed an asymmetric nucleus. Later, (Nieto et al., 1986) showed that the nucleus was not only asymmetric, but offset from the bulge. Almost 20 years after the initial observations, Hubble Space Telescope Wide Field/Planetary Camera (*HST*/WFPC)

images, with $0\farcs043$ per pixel resolution, showed that the nucleus of M31 contains two separate components. The component with the higher surface brightness, which was observed by Stratoscope II, is known as P1; the fainter peak is designated P2. P1 and P2 are separated by $0\farcs49 \pm 0\farcs01$ or 1.8 pc (Lauer et al. 1993). P2 lies closest to the nuclear/bulge center which is coincident with the peak in stellar velocity dispersion. That is to say that the kinematic center is separate from the luminosity peak (Dressler & Richstone 1988; Kormendy 1988). P1 and P2 contain stars of the same stellar spectral type (K), indicating that they are a part of the same system (Kormendy & Bender 1999). Tremaine (1995) explained the double nucleus of M31 as the projected appearance of an apsidally-aligned eccentric stellar disk. The stars in the eccentric nuclear disk travel around the supermassive black hole within the radius of influence on Keplerian orbits. The two observed components correspond to apocenter (P1) and pericenter (P2) of the eccentric nuclear disk.

The fact that we see an eccentric nuclear disk in our largest galactic neighbor suggests that apsidally-aligned stellar disks may be a common occurrence in galactic nuclei. Even with observational challenges due to resolution, evidence may exist for many eccentric nuclear disks in the local universe. Lauer et al. (1996) showed that NGC 4464B also contains a double nucleus and is likely host to a similar structure to the eccentric disk in M31. Lauer et al. (2002) identified numerous galaxies with local surface brightness minima in their centers, noting that at least some may be related to the double-nucleus systems. Lauer et al. (2005) presented *HST* observations of 77 early-type galaxies. They noted that the galaxies with offset centers may be poorly resolved examples of double nuclei or central minima. About 15% of nearby early-type galaxies have features consistent with eccentric nuclear disks seen from different orientations on the sky (Lauer et al. 2005). Furthermore, Gruzinov et al. (2020) showed that a lopsided configuration can be an equilibrium mode of a rotating nuclear star cluster.

An eccentric nuclear disk is composed of stars moving on apsidally aligned, near-Keplerian orbits around a central supermassive black hole. Hopkins & Quataert (2010a,b)

showed that eccentric nuclear disks can form from gas-rich galaxy mergers. In a galaxy with a scoured stellar core due to the binary black hole inspiral (Begelman et al., 1980), apsidal precession will be dominated by the gravitational potential of the newly formed disk and not by a spherical background potential. This increases the chances of the eccentric nuclear disk being stable. The presence of an eccentric nuclear disk in a galaxy could therefore provide information about the galaxy's merger history. Stellar orbits in the disk precess prograde with respect to their orbital angular momenta. Higher eccentricity orbits precess more slowly and end up behind the bulk of the disk, which then torques them to lower eccentricities. The orbits then precess more rapidly. In this way, orbits precess back and forth across the disk oscillating in eccentricity. This secular mechanism may explain the high rate of tidal disruption events (TDEs) observed in post-merger, starburst K+A/E+A galaxies (Madigan et al. 2018a). Stars from these disks preferentially disrupt at orbital inclinations of 0° and 180° (Wernke & Madigan 2019). Combined with the high rate of TDE production, this creates the conditions for overlapping TDE disks. The high TDE rates also create more opportunity for gravitational wave bursts from TDEs to be observed by the Laser Interferometer Space Antenna (LISA) (Pfister et al. 2021). Eccentric nuclear disks should also efficiently torque orbits of compact stellar remnants to high eccentricities which may result in extreme mass ratio inspirals (EMRIs), another exciting target for LISA.

In this paper, we show that double nuclei, offset nuclei, and nuclei with central minima can all be recovered by viewing eccentric nuclear disks in isolation from different lines of sight. We also show that gravitational mass segregation leads to heavier stars concentrating in the apocenter peak. Photometric and spectroscopic maps of eccentric nuclear disks have been produced to compare the M31 eccentric disk by Lauer et al. (1993), Tremaine (1995), Kormendy & Bender (1999), Peiris & Tremaine (2003), Brown & Magorrian (2013), and Lockhart et al. (2018). The novelty of the work presented here is that we "observe" eccentric nuclear disks in *self-gravitating* N-body simulations. We quantify the expected prevalence

of double nuclei and offset nuclei and compare to the Lauer et al. (2005) survey. We note that using N-body simulations restricts us to simulating a narrow range in semi-major axis. In effect we simulate only the innermost edge of the disk. For this reason we refrain from making direct comparisons with the M31 nucleus; rather we examine the qualitative features of the self-gravitating structure. Furthermore, we simulate a disk that is a factor of one hundred lower in mass than the central black hole which means that our disks are photometrically modest systems. In reality, such a disk would be overwhelmed by background stellar cusps and bulges. However, we simulate the eccentric nuclear disks in isolation, without the presence of a bulge or nuclear cusp, in order to pinpoint the features made by this lopsided structure.

We present the paper in the following manner. In Section 3.2 we describe the initial conditions and parameters for our simulations, and explain the methods used to rotate and "observe" our simulated disks. In Section 3.3 we explore the photometric maps of eccentric nuclear disks from different orientations. We also explore the effects of differing resolution and number of stellar particles. In Section 3.4, we make kinematic maps of an eccentric nuclear disk, including line-of-sight velocity and velocity dispersion maps. In Section 3.5 we summarize and discuss our results.

3.2 Methods

We run N-body simulations of eccentric nuclear disks about supermassive black holes with `REBOUND` (Rein & Liu 2012) and the `IAS15` integrator (Rein & Spiegel 2015). We initialize simulations with the following parameters: $N = 100 - 1000$ star particles, each with an initial eccentricity of $e = 0.8$, a range of semi-major axes ($a = 1 - 2$) with a surface density of $\Sigma \propto a^{-2}$, Rayleigh distributed inclinations with mean 10°, Gaussian distributed longitude of pericenter (ϖ) with mean 1 radian and standard deviation 0.5 radian, and a disk mass of $10^{-2} M_\bullet$, where $M_\bullet$ is the mass of the black hole. The particles are distributed randomly between $[0, 360°)$ in mean anomaly (M) and longitude of ascending node (Ω).

At the end of each integration, we populate each orbit with 100 stars uniformly in mean anomaly; this increases the effective resolution. We then make surface density plots for the eccentric nuclear disk looking down the positive z-axis, rotating the disk itself to produce different lines of sight. These orientations are generated by points randomly drawn on a sphere, represented by

$$\theta = \arccos(2u_1 - 1) \tag{3.1a}$$

$$\phi = 2\pi u_2, \tag{3.1b}$$

where u_1 and u_2 are both uniform in $(0, 1)$. We use $\hat{k}$ to describe the unit vector pointing to (θ, ϕ). We rotate the angular momentum vector of the disk to the chosen point on the sphere by rotating by an angle ω around the vector $v_{\rm rot}$ with Rodrigues' rotation formula, where

$$\omega = \arccos(\hat{z} \cdot \hat{k}) \tag{3.2a}$$

$$v_{\rm rot} = \hat{z} \times \hat{k}. \tag{3.2b}$$

With this definition, $\theta = 90^\circ$ indicates that the disk will be seen edge on. ϕ then determines if the disk is viewed more along the major axis or the minor axis. $\phi = 0^\circ$ or 180° means we look down the major axis, while $\phi = 90^\circ$ or 270° means we look down the minor axis of the disk. $\theta = 0^\circ$ or 180° means we will observe a face on disk.

With 100 different "observations" of each disk, following Lauer et al. (2005) we classify them by eye into three main types of nuclei: double nuclei or nuclei with central minima, offset nuclei, and normal or typical nuclei. We refer to these categories as double nuclei, offset nuclei, and centered nuclei respectively.

In addition to photometric maps, we create line-of-sight velocity maps, velocity dispersion maps, and maps of the skew and kurtosis in the line-of-sight velocity in each orientation. We simulate a circular disk with the same parameters as our eccentric nuclear disk simulations to demonstrate the differences between them. We note that these maps and categories

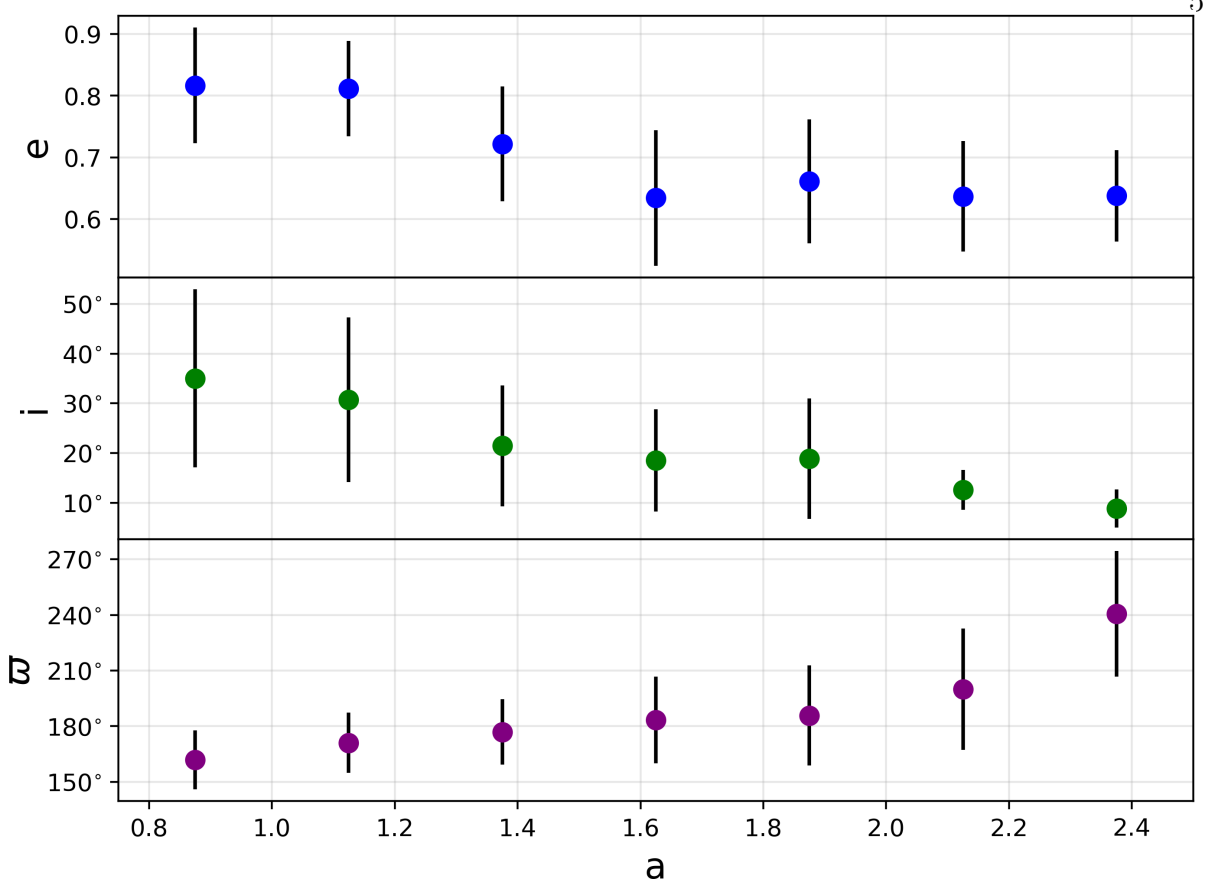

Figure 3.1: Orbital elements of an eccentric nuclear disk at 200 orbital periods (two secular times) as a function of semi-major axis: eccentricity (top), inclination (middle), and longitude of pericenter (bottom); mean values with 1σ error bars.

are illustrative only as the photometric and kinematic appearance of an eccentric nuclear disk (including the basic question of which of P1 and P2 is brighter) will be wavelength dependent in reality. Disks of various ages, mass functions, and degrees of mass segregation may present themselves very differently as a function of photometric band.

3.3 Photometric Maps

We create photometric maps of our simulated eccentric nuclear disks after two dynamical times. Here we define the secular dynamical timescale as

$$t_{\rm sec} \equiv \left(\frac{M_\bullet}{M_{\rm disk}} \right) P, \tag{3.3}$$

where $M_{\rm disk}$ is the mass of the disk and P is the orbital period for a star at the inner edge of the disk (Rauch & Tremaine 1996). In our simulations, $t_{\rm sec} = 100P$. We create photometric maps after two dynamical times to allow the disk more than a full secular time to relax. In particular the disk moves away from its (arbitrary) initial conditions and develops a negative eccentricity gradient, in which stars at lower semi-major axes have higher equilibrium eccentricities. Furthermore, Foote et al. (2020) find that vertical mass segregation occurs within two dynamical times (see section 3.3.1). Figure 3.1 shows the orbital eccentricity (top), inclination (middle), and longitude of pericenter (bottom) of a representative eccentric nuclear disk at two secular times as a function of semi-major axis.

In Figure 3.2 we show a small sample of photometric maps of our simulated eccentric nuclear disk viewed from various angles. The location of the supermassive black hole is indicated with a cross at the origin. Most lines of sight produce offset, elliptical nuclei, like those seen in the top two rows. Several of the surface density profiles reveal an M31-like tail or faint second peak. Some of these M31-like double nuclei are shown in the last row of Figure 3.2. Finally, we even see some nuclei that appear photometrically "normal," centered on the supermassive black hole, like those seen in the third row of Figure 3.2. The surface density contours are still elliptical.

With $N = 1000$ star particles and a resolution of 0.2 (where $a = 1$ is the semi-major axis at the inner edge of the disk), 78% of the orientations result in an elliptical nucleus that is offset from the central black hole. A strong double nucleus occurs 16% of the time and 6% of the orientations result in a single peak that is centered on the black hole. The percentages of double, centered, and offset nuclei for varying resolutions and N are listed in Table 3.1. We vary resolutions between 0.4, 0.2, and 0.13 with both $N = 100$ and $N = 1000$ stars. As expected, more double nuclei are seen with increasing resolution and numbers of stars. For reference, the double nucleus of M31 was observed with a resolution of $0\farcs044$ per pixel (Lauer et al. 1993), or 0.75 in code units if the inner edge of the disk is about 0.2pc ($a = 1$). This adopts the distance to M31 of 770kpc (Freedman & Madore 1990) so that $1'' = 3.4$pc.

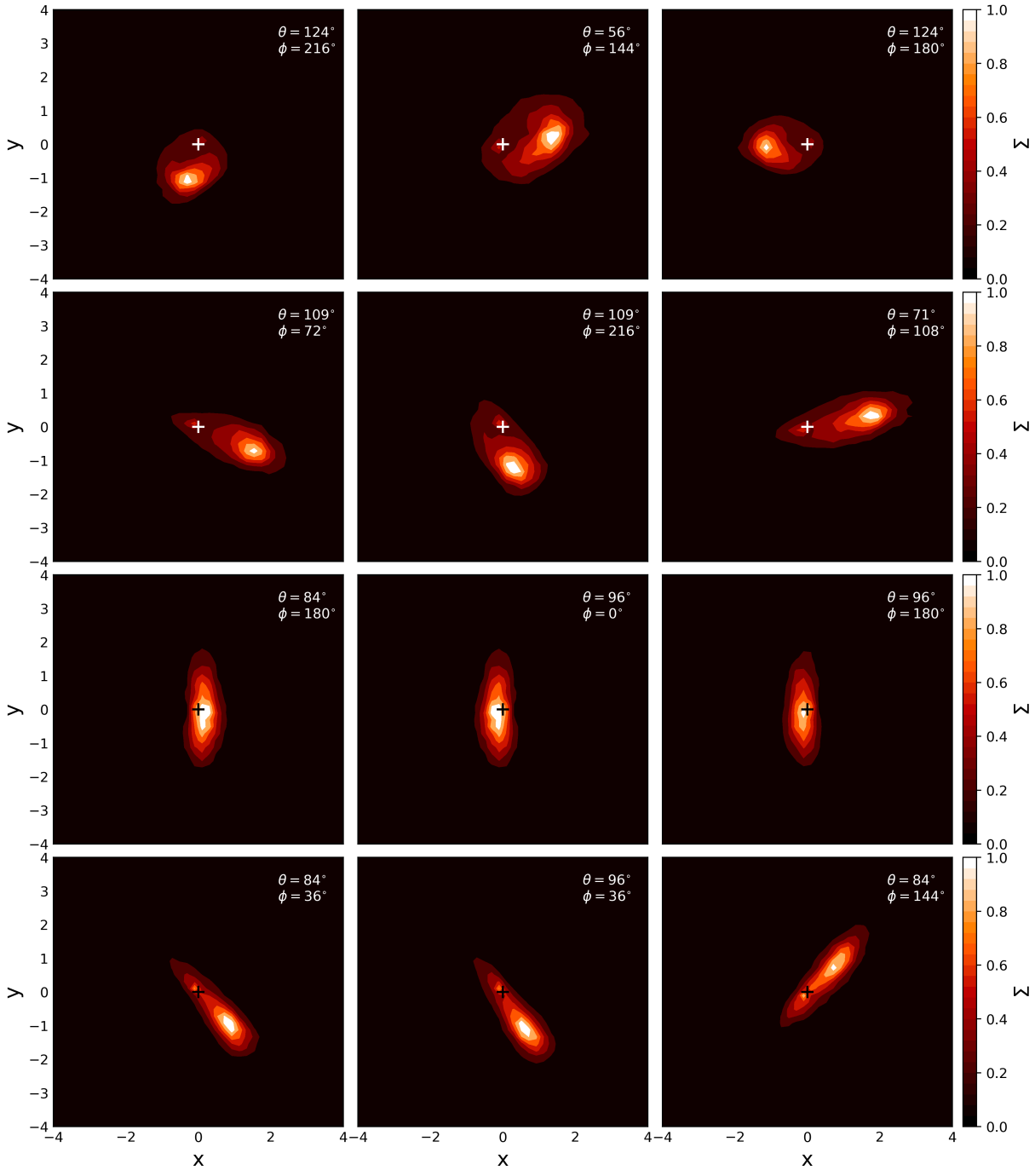

Figure 3.2: A sample of photometric maps of an eccentric nuclear disk viewed from different orientations. The position of the supermassive black hole is marked with a cross at the origin. This sample was created from an N-body simulation with $N = 1000$ stars and a photometric resolution of 0.2. The first two rows show examples of offset nuclei. The third row shows examples of centered nuclei, while the bottom row shows examples of double nuclei. θ and ϕ, randomly selected points on an sphere that generate new disk orientations as given in Equation 3.1, are listed for each panel.

Table 3.1: Percentage of double nuclei, centered nuclei, and offset nuclei seen with varying resolution and N star particles. Resolution is presented in terms of the inner edge of the disk. The sample size for each is 100 orientations.

Resolution	N	Double	Centered	Offset
0.4	100	0%	9%	91%
0.2	100	8%	7%	85%
0.13	100	15%	6%	79%
0.4	1000	1%	6%	93%
0.2	1000	16%	6%	78%
0.13	1000	34%	5%	61%

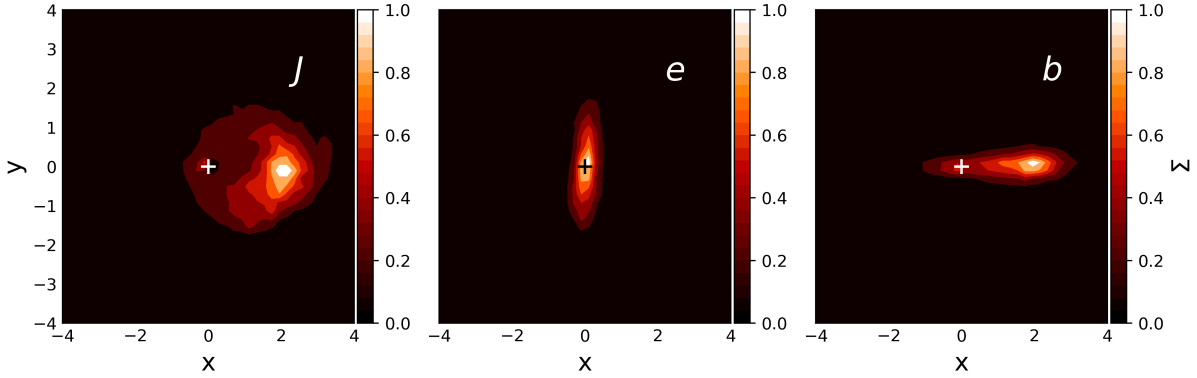

Figure 3.3: Photometric maps of an eccentric nuclear disk (N=1000 stars, 0.2 resolution) viewed along the angular momentum vector ($\boldsymbol{J}$), eccentricity vector ($\boldsymbol{e}$), and semi-latus rectum ($\boldsymbol{b}$). The location of the supermassive black hole is marked with a cross at the origin.

The three main categories of nuclei are best captured by viewing specific orientations as shown in Figure 3.3. If we orient the disk such that its angular momentum vector points towards us, and the disk is observed face on, we see a maximally offset, elliptical nucleus. The surface density contours become more elliptical and centered as the disk is rotated such that the eccentricity vector, or the major axis, points towards the observer. Looking down the eccentricity vector of the eccentric nuclear disk results in a single peak centered on the black hole. These centered orientations may appear photometrically "normal" (albeit with highly elliptical contours), but we should still expect to see unusual velocity signatures (see Section 3.4). Finally, if the observer looks along a line of sight parallel to the minor axis of the disk, they will observe a double-peaked nucleus similar to that found in M31. Figure 3.4

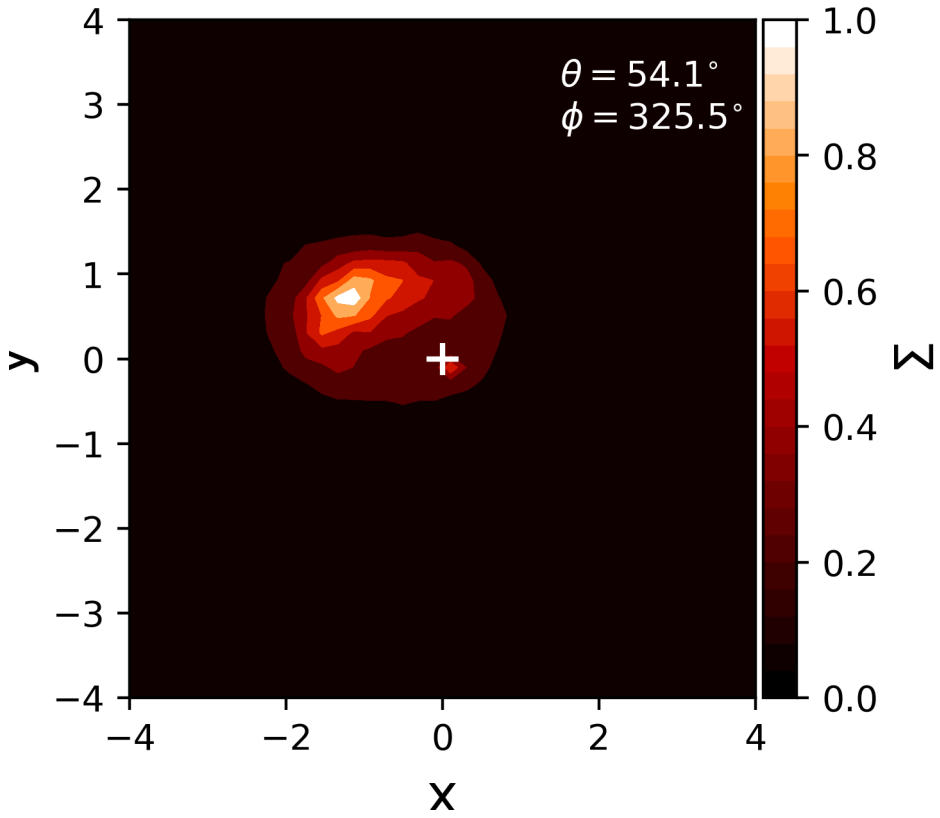

Figure 3.4: Photometric map of an eccentric nuclear disk with N=1000 stars and 0.2 resolution matching the observed orientation of the disk in the M31 nucleus. We use the angles given by Peiris & Tremaine (2003) to define θ and ϕ for M31. We do not observe the M31 disk edge-on, but it is sufficiently inclined to produce a small, second peak.

shows a photometric map that matches the observed orientation of the M31 double nucleus. We use angles derived from the nonaligned model in Peiris & Tremaine (2003) to define the θ and ϕ orientation angles for the M31 nuclear disk. We again note that there is no bulge or background stellar cusp in our simulations. The inclusion of such populations would enhance the observed luminosity of the secondary (P2) peak (Tremaine 1995).

In general, we observe a centered nucleus when viewing the eccentric nuclear disk along its eccentricity vector, or major axis, $\pm 6°$ in θ and $\pm 12°$ in ϕ. Similarly, we observe a double nucleus when viewing the eccentric nuclear disk along its minor axis $\pm 6°$ in θ and $\pm 30°$ in ϕ. In fact we find that the appearance of a double nucleus is most obvious when the disk is viewed just off of the minor axis, so that the observer's line of sight penetrates through

more of the disk at pericenter, enhancing the fainter (P2) peak.

3.3.1 Mass Segregation

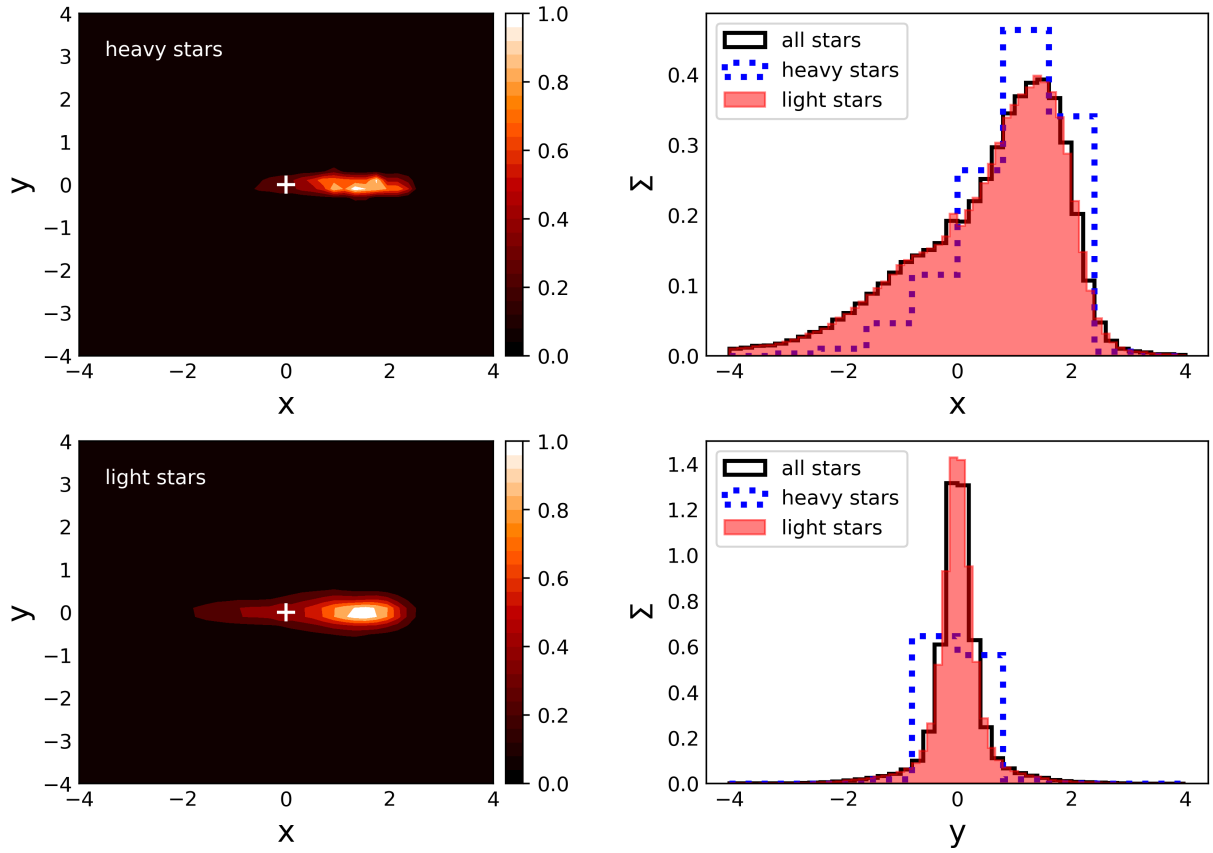

Figure 3.5: Mass segregation in photometric maps of simulated eccentric nuclear disks with N=400 light stars, N=5 heavy stars, stars and a resolution of 0.2. 15 simulations from Foote et al. (2020) are combined to create this plot. Top left: surface density plot of heavy stars. The cross marks the position of the supermassive black hole. Bottom left: surface density plot with only light stars for the disk orientation. The cross marks the position of the supermassive black hole. Top right: x-histogram of the surface density plots (i.e., moving along the disk major axis). The solid, black line histogram includes all stars. The dotted, blue histogram shows heavy stars (at low semi-major axis). The filled-in, red histogram shows light stars (at high semi-major axis). Bottom right: the y-histogram of the surface density plots. The density ratio between P1 and P2 is larger for the heavy star population than for the light star population.

Foote et al. (2020) showed that high mass stars segregate to lower semi-major axes and inclinations in an eccentric nuclear disk. In their N-body simulations, heavy stars

differ in mass by a factor ten from light stars. This simple two-species model, put forward by (Alexander & Hopman, 2009), approximates an evolved stellar population (coeval or continuously star-forming); light stars represent old low-mass main-sequence dwarfs, white dwarfs, and neutron stars with masses of order a solar mass, and heavy stars represent stellar-mass black holes with masses of order ten solar masses. Here we use simulations from Foote et al. (2020) in order to show the effect of mass segregation on the surface density of eccentric nuclear disks. Here we show the results of simulations in the strong mass segregation regime (Alexander & Hopman, 2009), where the heavy stars sink efficiently to lower semi-major axes and orbital inclination due to dynamical friction. In Figure 3.5, we combine 15 simulations, each with 400 light stars and 5 heavy stars. The relaxation coupling parameter for this model is $\Delta = 0.384$ (Alexander & Hopman, 2009, equation 10). The heavy stars concentrate preferentially in the brighter peak (P1). We see the same effect in simulations with larger Δ values (weaker mass segregation) but to a lesser extent. While the observational effects of this mass segregation will depend on the wavelength of the observations and the age of the stellar population, our results indicate that the two peaks (P1 and P2) of an eccentric nuclear disk with an evolved stellar population will have differing mass to light ratios at all wavelengths as the fraction of heavy objects are enhanced in P1 relative to P2. It makes sense that the heavy stars are found in the most offset peak because stars at low semi-major axes are the most eccentric in an eccentric nuclear disk (see Figure 3.1 and Madigan et al. (2018a)) and they spend the most time at apocenter.

3.4 Kinematic Maps

In Figure 3.6, we show photometric maps of disks alongside their line-of-sight velocity and velocity dispersion maps. The top row shows an eccentric nuclear disk oriented such that its eccentricity vector, or major axis, is pointed towards the observer. The middle row has the disk's minor axis pointed towards the observer. The bottom row shows an edge-on circular ring for comparison. The ring is initialized with the same orbital parameters as the

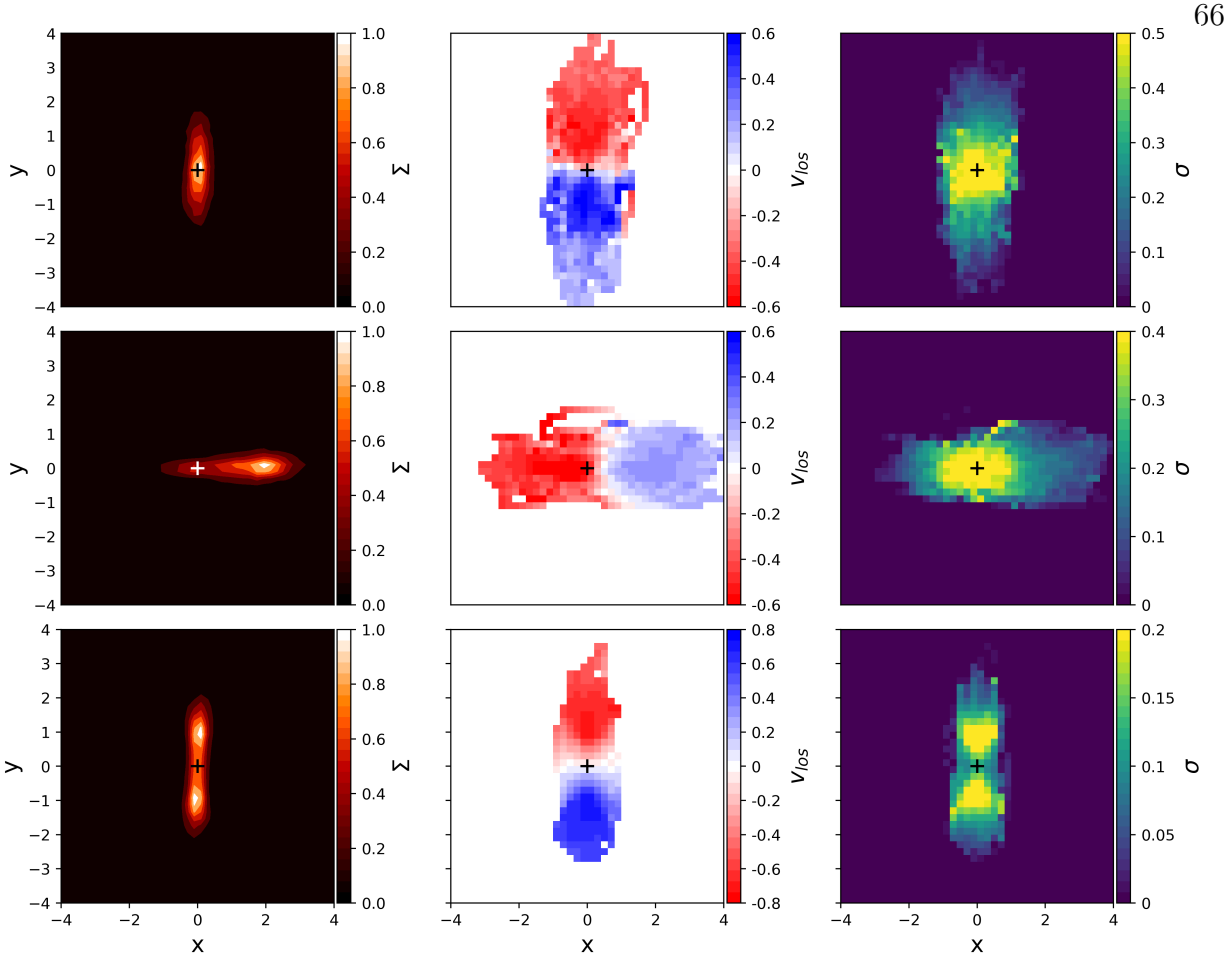

Figure 3.6: Top row: An eccentric nuclear disk with N=1000 stars and 0.2 resolution viewed along its major axis. Middle row: An eccentric nuclear disk with N=1000 stars and 0.2 resolution viewed along its minor axis. Bottom row: A circular disk with N=1000 stars and resolution of 0.2 viewed edge on. The left column shows the surface density. The position of the supermassive black hole is marked with a cross. The middle column shows the line-of-sight velocity. Positive velocity is out of the page, so that blue indicates blue-shifted stars and red indicates red-shifted stars. The right column shows the standard deviation of the line-of-sight velocity.

eccentric nuclear disk but with zero eccentricity.

In the top row, the photometric map shows what looks like an axisymmetric disk of stars orbiting a black hole (indicated by the cross at the origin). The line-of-sight velocities, however, are lower than in the circular disk. This is due to the fact that stars spend most of the time at apocenter in an eccentric nuclear disk, where their velocity is lower than the

circular velocity at that same radius. The velocity dispersion values peak around the black hole in the eccentric nuclear disk, but are significantly larger than in the circular case.

The peak of the photometric values in the middle row is clearly offset from the black hole, with a faint second peak. The blue-shifted (right) side of the disk corresponds to apocenter of the disk and has a much lower velocity than the red-shifted (left) side which maps to pericenter of the disk. The black hole lies within the red-shifted side. The velocity dispersion peaks around the supermassive black hole, even though the luminosity in the surface density plot peaks to the right of the supermassive black hole. In the circular disk, the strengths of the red- and blue-shifted velocities are equal in value and the black hole is directly in the center.

In the bottom row, we show an edge-on circular ring instead of an eccentric nuclear disk. When viewed edge-on, the circular ring of stars appears elongated and centered on the supermassive black hole, similar to the top row of Figure 3.6. The line-of-sight velocity distribution for the circular disk is symmetric about its rotation axis. The line-of-sight velocity dispersion is centered on the black hole with a central minimum, as expected for a circular ring of stars.

In Figure 3.7, we take a closer look at the kinematic profiles of our eccentric nuclear disks by mapping the skew and kurtosis in the line-of-sight velocity distributions. As in Figure 3.6, the top row shows an eccentric nuclear disk oriented such that its eccentricity vector is pointed towards the observer. The middle row shows an eccentric nuclear disk with its minor axis pointed towards the observer. The bottom row shows an edge-on circular ring for comparison.

In the edge-on circular ring (bottom row), the outer regions of the disk ($a > 1$), are skewed such that they have tails approaching zero velocity; this gives them positive and negative skew values for stars with negative and positive line-of-sight velocities respectively. Stars with the fastest line-of-sight velocities are in this region, and we look through a slower-moving portion of the disk. Within the inner edge of the disk ($a < 1$), the line-of-sight

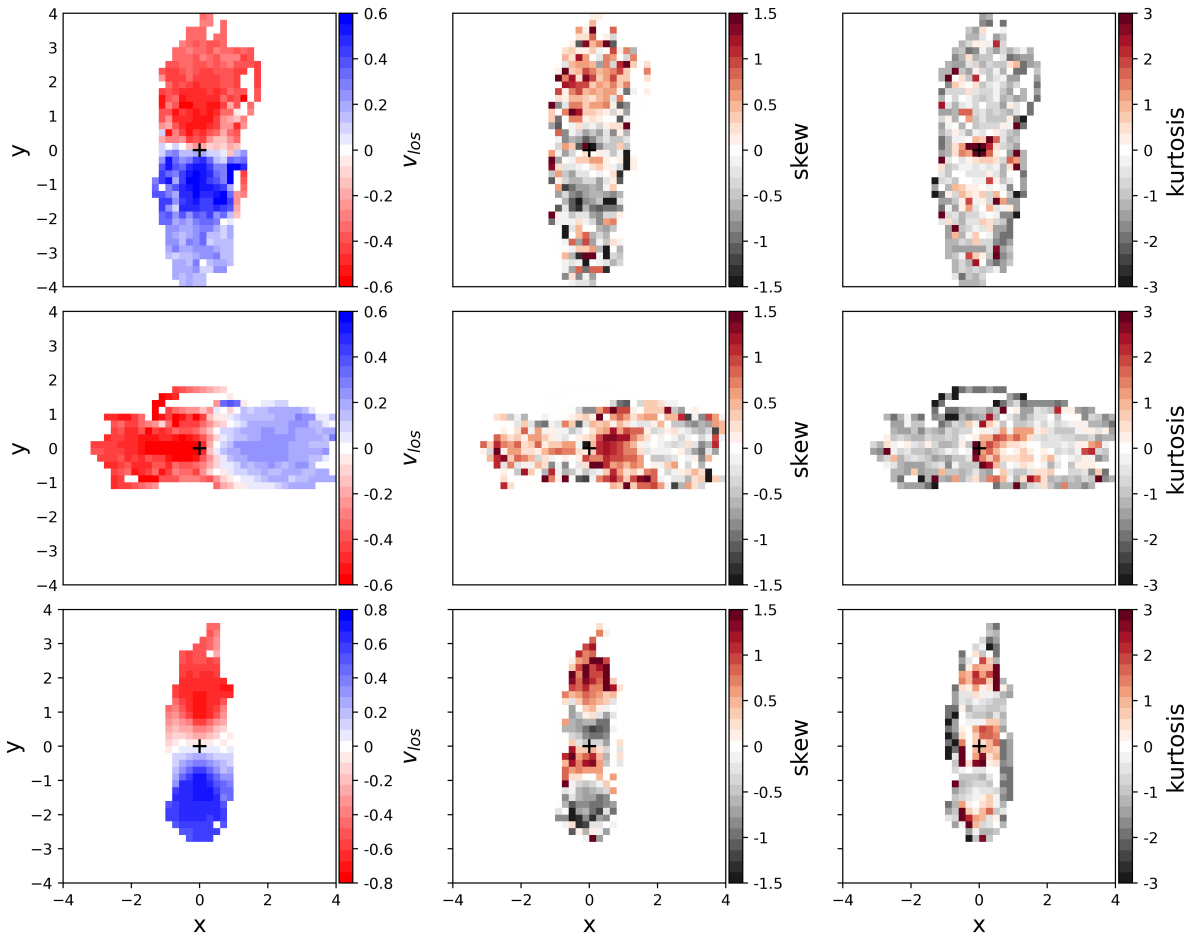

Figure 3.7: Top row: An eccentric nuclear disk with N=1000 stars and 0.2 resolution viewed along its major axis. Middle row: The same eccentric nuclear disk viewed along its minor axis. Bottom row: A circular ring viewed edge-on. The left column shows the line-of-sight velocity. Positive velocity is out of the page, so that blue indicates blue-shifted stars and red indicates red-shifted stars. The position of the supermassive black hole is marked with a cross. The middle column shows the skew in the line-of-sight velocity and the right column shows the kurtosis in the line-of-sight velocity.

velocities are small, as we are observing stars with primarily transverse velocities. The velocity distributions are quite flat in the central region with more low values than high to give skew values opposite to those in the outer disk.

Although noisier, the eccentric nuclear disk in the top row of Figure 3.7 shows very similar behavior in skew to the circular disk. The inner regions with opposite skew values appear smaller due to the orientation of the eccentric orbits. Viewing the eccentric nuclear

disk from the minor axis (middle row), we see that the line-of-sight velocity distributions are generally positively skewed on the left side of the disk near pericenter and negatively skewed on the far right side of the disk near apocenter.

In the right column of Figure 3.7, we map the kurtosis in the line-of-sight velocity distributions for an eccentric nuclear disk and a circular disk. The eccentric nuclear disk generally shows negative values of kurtosis, except in the very center where we see positive kurtosis values. This is in agreement with observations from Gültekin et al. (2014), who report mostly negative values of kurtosis for the nuclear stellar disk in NGC 3706.

In Figure 3.8, we look at the line-of-sight velocity distribution in several single pixels of the eccentric nuclear disk at 0.2 resolution. The pixels are sampled in a cross pattern from the very center (origin) of the eccentric nuclear disk in the top row of Figure 3.6. We compare the distributions to the distributions of the line-of-sight velocity in the central pixels of the circular disk in the bottom row of Figure 3.6. In a circular disk, we expect to see a velocity distribution that is peaked at a single value. Because we take the single pixels from near the origin of the plot, and center of the disk, the single peak should be centered on zero for the circular disk. For this reason, the values of $|v_{\rm los}|/\sigma$ are very small for both the eccentric nuclear disk and the circular disk in the horizontal pixels of Figure 3.8. In the pixels in the vertical portion of the cross however, we see larger values in $|v_{\rm los}|/\sigma$ for the circular disk and unusually small values for the eccentric nuclear disk.

Figure 3.9 looks at the line-of-sight velocity distribution in single pixels of an eccentric nuclear disk, sampling in a cross pattern from the very center (origin) of the eccentric nuclear disk in the middle row of Figure 3.6 (viewed along the minor axis). The distributions are compared to the line-of-sight velocity distributions for a circular disk in the same orientation. Here, we see that the $|v_{\rm los}|/\sigma$ values are very small compared to the circular disk in the two right-most pixels in the horizontal portion of the cross. In the vertical portion of the cross, the $|v_{\rm los}|/\sigma$ values are so small for the circular disk because the pixels are taken from the inner edge of the disk where the line-of-sight velocities are extremely small.

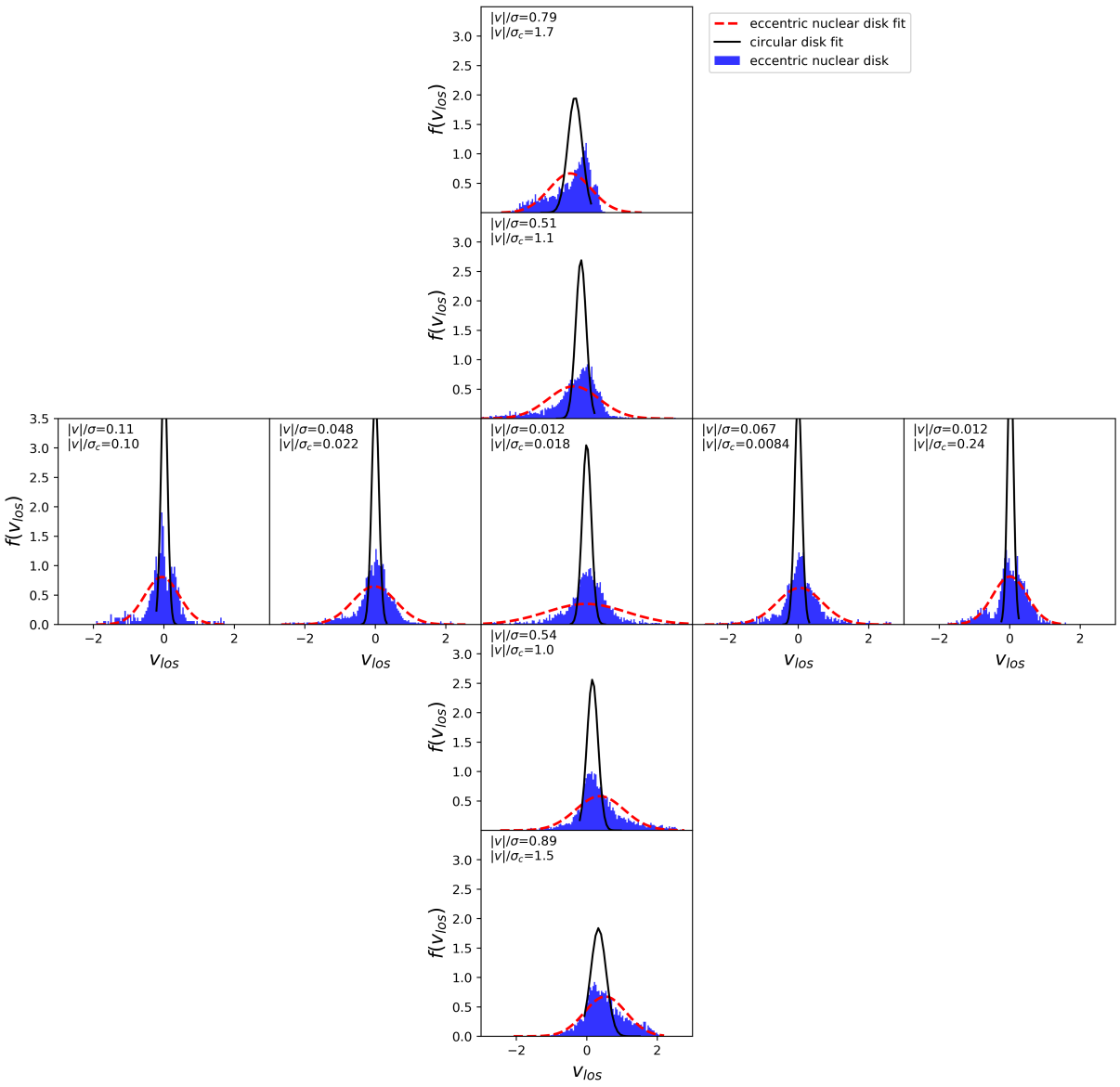

Figure 3.8: The line-of-sight velocity distributions for single pixels in an eccentric nuclear disk with N=1000 stars and 0.2 resolution viewed along its major axis are shown in blue (compare with top panel of Figure 3.6). Gaussian fits for the eccentric nuclear disk data are shown by the dashed red lines. The solid black lines show Gaussian fits for the line-of-sight velocity distributions in single pixels of a circular disk with N=1000 stars and 0.2 resolution (compare with bottom panel of Figure 3.6). The pixels are chosen in a cross pattern from the very center of each disk, so that the plot in the very center of the cross depicts the pixel centered on the black hole. The horizontal row shows five pixels chosen from the center of the disk along x (the minor axis), left to right. The vertical column shows five pixels chosen from the center of the disk along y, top to bottom. The velocity distributions for the eccentric nuclear disk are much broader than the narrow distributions of the circular ring. This means that the quantity $|v_{\rm los}|/\sigma$ is much lower for the eccentric nuclear disk than would be expected from a circular ring, except for when we look inside the inner edge of the circular disk, where the $v_{\rm los}$ values are extremely small.

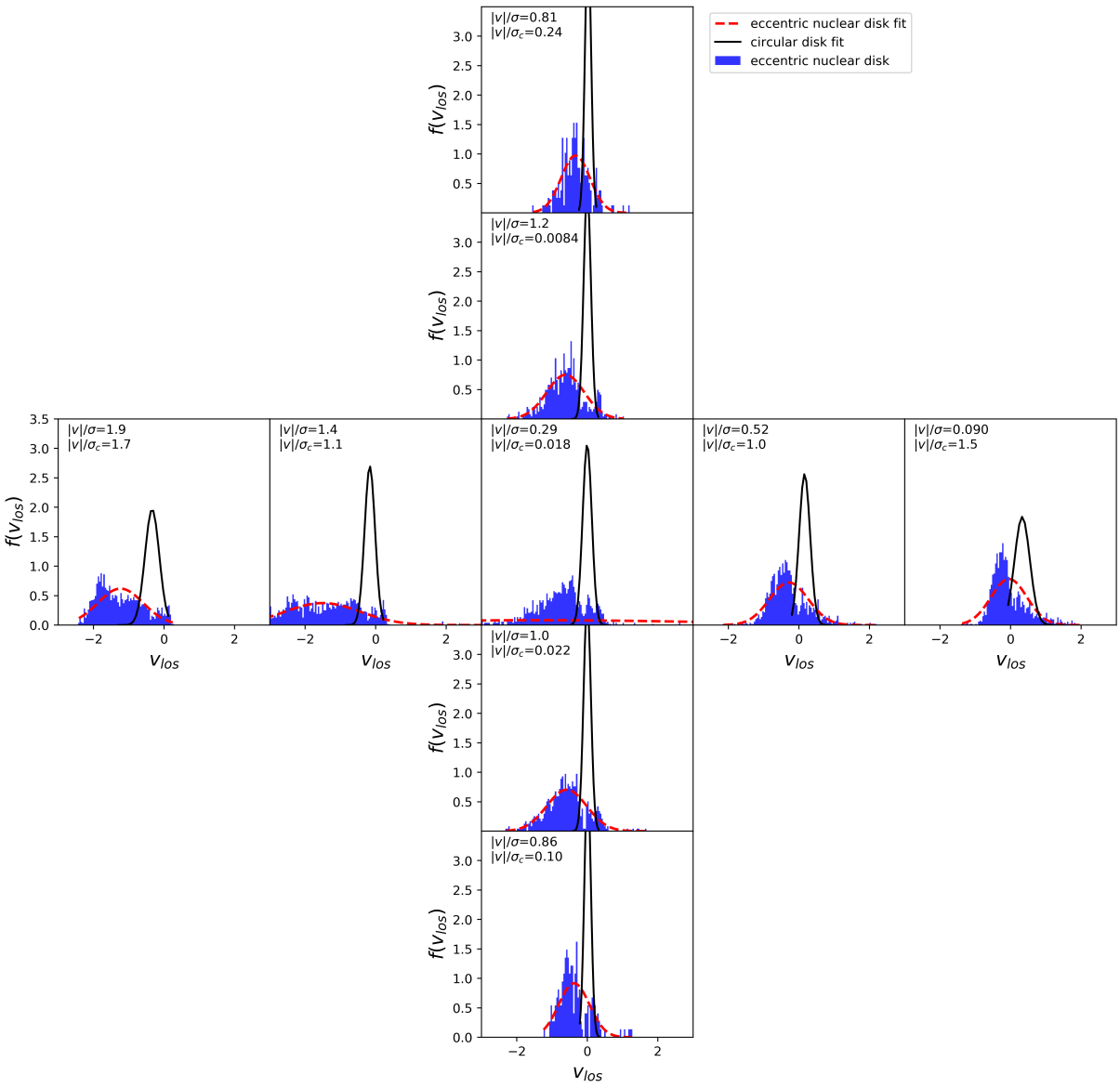

Figure 3.9: The line-of-sight velocity distributions for single pixels in an eccentric nuclear disk with N=1000 stars and 0.2 resolution viewed along its minor axis. The line-of-sight velocity distributions for the eccentric nuclear disk are shown in blue. Gaussian fits for the eccentric nuclear disk data are shown by the dashed red lines. The solid black lines show Gaussian fits for the line-of-sight velocity distribution in single pixels of a circular disk with N=1000 stars, 0.2 resolution, and oriented in the same way as the eccentric nuclear disk in the middle row of Figure 3.6. The pixels are chosen in a cross pattern from the very center of each disk, so that the plot in the center of the cross depicts the pixel centered on the black hole. The horizontal row shows five pixels chosen from the center of the disk along the major axis, left to right. The vertical column shows five pixels chosen from the center of the disk along y, top to bottom. The velocity distributions for the eccentric nuclear disk are red-shifted and much broader than the narrow distributions for the circular ring. In the right-most horizontal pixels, the $|v|/\sigma$ values are much smaller in comparison to the circular disk.

3.5 Discussion

In Madigan et al. (2018a) and Wernke & Madigan (2019), we focused on the internal dynamics of self-gravitating eccentric nuclear disks. Here we look at their photometric and kinematic maps. We rotate a simulated eccentric nuclear disk to observe the system from different viewing angles. We classify the resulting observations as double nuclei, centered nuclei, and offset nuclei in comparison to the galaxy sample studied by Lauer et al. (2005). Out of 77 galaxies, Lauer et al. (2005) found that 12 had centers too dust-obscured to derive surface density photometry. Out of the remaining 65, 5 had an offset nucleus and another 5 had either a double nucleus (1) or a local minimum in their surface brightness (4). That means that $\sim$15% of galaxies showed evidence for eccentric nuclear disks. We also discuss kinematic signatures expected from eccentric nuclear disks. Our results point to the following conclusions and implications:

(1) An eccentric nuclear disk with $N = 1000$ stars that is viewed from a large number of uniformly sampled angles at a resolution of 0.2 (where $a = 1$ is the inner edge of the disk) will result in a double nucleus 16% of the time, an offset nucleus 78% of the time, and will appear photometrically centered on the black hole 6% of the time. As resolution increases, the number of double nuclei observed also increases. Decreasing the number of simulated stars decreases the fraction of double nuclei observed.

(2) Foote et al. (2020) show that more massive bodies in an eccentric nuclear disk segregate to lower inclinations and semi-major axes. Using there simulation results, we show here that the most massive bodies in an eccentric nuclear disk should preferentially be found in the brighter peak furthest from the supermassive black hole (P1). While this result seems counter-intuitive at first, it is readily explained by the fact that orbits at low semi-major axes and inclination are the most eccentric, and bodies on eccentric orbits linger at apocenter. The two peaks of an eccentric nuclear disk will have different mass to light ratios.

(3) The average line-of-sight velocity values are lower in an eccentric nuclear disk than in a circular disk. The line-of-sight velocity dispersion values are higher and peak at the position of the supermassive black hole. This does not normally match the peak in photometry which is typically offset from the supermassive black hole in an eccentric nuclear disk.

(4) The skew of the line-of-sight velocity distributions of an eccentric nuclear disk generally resemble those of a circular disk (with some differences if the disk is viewed along its minor axis). The kurtosis values are generally negative except in the very center of the disk.

(5) The line-of-sight velocity distributions of an eccentric nuclear disk are much broader than the narrow distributions of a circular ring. In some pixels, the observational quantity $|v_{\rm los}|/\sigma$ is much smaller than expected from a circular ring.

NGC 3706 is an early-type galaxy with a central surface brightness minimum arising from an apparent edge-on stellar ring. Fitting imaging and spectroscopic data to axisymmetric orbit models, Gültekin et al. (2014) uncover a central black hole of mass $M = (6.0^{+0.7}_{-0.9}) \times 10^8 M_\odot$. They find however that the stellar ring is inconsistent with a population of co-rotating stars on circular orbits which would produce a narrow line-of-sight velocity distribution (as in the solid black lines of Figure 3.8). Instead the data indicate small line-of-sight values of $|v|/\sigma \sim 0.1 \sim 0.4$. They conclude that the stellar ring contains a retrograde (counter-rotating) component and is not consistent with co-rotating circular orbits. We look at this same value in both a simulated circular disk and a simulated eccentric nuclear disk in Figures 3.8 and 3.9 and find similarly low values for the eccentric nuclear disk. Could this feature be an eccentric nuclear disk? For an eccentric nuclear disk to be stable (i.e., apsidally clustered), inter-orbit torques must be sufficiently strong to damp differential apsidal precession. Hence orbits must be well-approximated by closed, Kepler ellipses. This translates to the condition that the disk lies within the radius of influence of a

black hole. As a consistency check, we determine that the central minimum feature in NGC 3706 lies within the radius of influence of the central black hole. We use the mass of the supermassive black holes, estimated using the $M - \sigma$ relation (Ferrarese & Merritt, 2000; Gebhardt et al., 2000), to determine the radius of influence (Peebles, 1972). In NGC 3706, the central minimum feature is within the calculated radius of influence.

In this paper we have simulated eccentric nuclear disks in isolation to focus on the effects of disk self-gravity on photometric and kinematic data. However, in reality, background stars will significantly contribute to the form of the gravitational potential, thus altering the dynamical evolution of the disk. We briefly discuss how this will affect our results. The stability of eccentric nuclear disks relies on the suppression of differential apsidal precession of disk orbits, maintained via inter-orbit gravitational torques (Madigan et al., 2018a). Precession also needs to be prograde with respect to the angular momentum of the disk unless the background potential is "abnormally" steep (Lynden-Bell, 1979; **?**). If we were to include a typical spherical background stellar distribution in our simulations (due to a cusp or bulge), disk orbits would undergo an enhanced rate of apsidal precession in the *retrograde* direction. The mass of the disk in our simulations would have to be enhanced to correct for this. In this way – including a background stellar potential and enhancing the disk mass – would move our simulations in a more astrophysically realistic direction. This is something we are interested in doing in future studies.

In Wernke & Madigan (2019) we showed that steady-state, eccentric nuclear disks have a non-negligible fraction of retrograde orbiting stars (in our previous simulations this amounted to $\sim$10%). In our current simulations, where we capture photometric and kinematic maps at 200 orbital periods, we show a lower percentage of retrograde orbits ($\sim$4%) because the secular dynamical mechanism causing TDEs and retrograde orbits is just beginning to have an effect. Future work will include analysis of these maps at later times with a larger population of retrograde orbits.

Chapter 4

An Eccentric Disk in the Outer Solar System

Axisymmetric near-Keplerian disks of eccentric orbits are subject to a dynamical instability due to the coherent, secular torques between their orbits. This "inclination instability" results in an exponential growth of orbital inclinations, clustering in argument of pericenter (ω), and a lowering of orbital eccentricities. After the instability saturates, a lopsided $m = 1$ mode (or an eccentric nuclear disk) forms. We show here that the apsidal clustering is long-lasting in simulations of a primordial scattered disk[1] with the orbit-averaged gravitational influence of the giant planets included. These collective gravitational dynamics may well explain the strange orbits of minor planets in the outer Solar System but we are also interested in finding evidence of the inclination instability in extra-solar debris disks. To this end, we present line-of-sight velocity maps of the instability as it occurs and surface density maps of the apsidal clustering that persists afterwards. We show surface density and line-of-sight velocity maps in both face-on and edge-on orientations.

4.1 Introduction

In previous chapters, we explored the dynamics of eccentric nuclear disks of stars orbiting supermassive black holes. Here we look at axisymmetric disks of bodies on eccentric orbits around a central star and show that this system evolves to an eccentric nuclear disk.

[1] The scattered disk is a structure in the outer solar system beyond Neptune, populated by small, icy minor planets on eccentric orbits.

The dynamics behind this eccentric nuclear disk formation are driven by secular (long-term orbit-averaged) gravitational torques between orbits.

Two-body relaxation is the uncorrelated diffusive process by which bodies exchange energy and angular momentum amongst themselves (Frank & Rees 1976). A circular disk diffuses slowly through two-body relaxation and does not undergo collective behavior (Ida 1990). An axisymmetric disk composed of high eccentricity orbits however, is subject to a dynamical instability. This dynamical instability, named the "inclination instability," is driven by the collective gravity of bodies in an axisymmetric near-Keplerian eccentric disk (Madigan & McCourt, 2016). The inclination instability causes orbits to cluster in argument of pericenter (ω) and grow exponentially in inclination. A narrow distribution in argument of pericenter geometrically translates to the orbits coherently tilting out of the disk plane. An initially thin disk lifts into the shape of a cone or a bowl due to the gravitational forces between the bodies in the disk. The physical mechanism behind the inclination instability is described in Madigan et al. (2018b).

Observations of extreme trans-Neptunian Objects (eTNOs) in the outer solar system show they are clustered in both argument of pericenter (ω) and longitude of pericenter (ϖ, i.e., apsidally clustered). Some have worked to explain this observed clustering as being a product of observational bias (see Trujillo (2020) and Kavelaars et al. (2020) for detailed discussions). Others have hypothesized that a large planet, Planet 9, exists beyond Neptune and perturbs the orbits of eTNOs so that they are apsidally clustered (Batygin & Brown 2016; Batygin et al. 2019). Zderic & Madigan (2020) recently showed that the inclination instability (and hence clustering in ω and ϖ) will occur in a massive primordial scattered disk precessing under the gravitational influence of the giant planets if the disk between $\sim$100–1000 AU is of order 20 Earth masses. This is similar to, but greater than, the predicted mass of Planet 9. This theory has the advantage of not needing anything new in the solar system - the mass comes from leftover planetesimals being scattered outwards by the giant planets early in the formation of the solar system.

Recent observations have shown lopsided protoplanetary disks and exoplanet systems (e.g., van der Marel et al. 2013). Some observations have even shown spiral arms in the line-of-sight velocity of protoplanetary disks (e.g., Huang et al. 2018; Rosotti et al. 2020). One possible explanation for lopsided features or spiral arms could be the presence of young planets. Planets do perturb the disks they are forming in (Goldreich & Tremaine 1979). In this case, spiral arms could be a helpful tool in finding young planets in exoplanetary systems. Another explanation for spiral arms in protoplanetary disks is the self-gravity of the particles in the disk (Rice et al. 2003; Cossins et al. 2010). The instability driven by the collective gravity of scattered minor planets is a new idea that could explain these observations. Here we present surface density maps of the disk in the outer solar system showing apsidal clustering. We also show the formation of spiral structures in line-of-sight velocity space.

This chapter is formatted in the following manner: in Section 4.2 we describe our N-body simulations, the addition of the gravitational influence of the giant planets, and the initial conditions and parameters for our variety of simulations. We present our photometric and kinematic maps of a compact disk, compact disk with the giant planets, scattered disk, and scattered disk with the giant planets in Section 4.3. In Section 4.4 we summarize and discuss our results.

4.2 N-Body Simulations

Our N-body simulations use the open-source framework `REBOUND` with the `IAS15` adaptive timestep integrator (Rein & Liu 2012; Rein & Spiegel 2015). Additionally, we use `REBOUNDx` (Tamayo et al. 2020) to add a zonal quadrupole term, J_2, to the central body to emulate the orbit-averaged influences of the giant planets (Jupiter, Saturn, Uranus, and Neptune). We use the Kepler elements: semi-major axis (a), eccentricity (e), inclination (i), argument of pericenter (ω), longitude of the ascending node (Ω), and mean anomaly (M) in order to describe the orbits in the disk. The number of disk particles is $N = 400$ and the

disk mass is $M_{\rm disk} = 10^{-3}\,M_\odot$, where $M_\odot$ is the mass of the sun.

The compact disk configuration (used here and in Zderic et al. (2020)) is a simplified, idealized setup which we introduced in Madigan & McCourt (2016); Madigan et al. (2018b). This configuration is unrealistic but ideal for physical analysis. The disk of orbits is initialized with a semi-major axis a distribution drawn uniformly from [0.9, 1.1], eccentricity $e = 0.7$, and inclination $i = 10^{-4}$ radians. The disk is initially axisymmetric, meaning that argument of pericenter, longitude of ascending node, and mean anomaly are all drawn from a uniform distribution in $[0, 2\pi)$ radians. We run simulations both with and without the added J_2 component.

The scattered disk configuration (used here and in Zderic et al. (2021)) is initialized to approximately model the scattered disk in the outer Solar System. The model is axisymmetric with an order of magnitude spread in semi-major axis. All bodies have the same initial pericenter ($p_0 = 30$ AU). As for the other initial orbital parameters, a_0 is drawn from a log-uniform distribution between $[10^2, 10^3]$ AU, i_0 is drawn from a Rayleigh distribution with a mean of 5°, and ω, Ω, and M are chosen from a uniform distribution in $[0, 2\pi)$ radians. All interactions between all particles are calculated. We run simulations both with and without the added J_2 component.

4.3 Photometric and Kinematic Maps

In Figures 4.1 through 4.19, we plot snapshots in time of a simulation of an axisymmetric, near-Keplerian disk with $N = 400$ bodies. We first populate each orbit of the simulation with $N = 100$ bodies spaced uniformly in mean anomaly to increase the effective resolution. We include figures of a compact disk configuration, a compact disk that includes the gravitational influence of the giant planets (J_2), a primordial scattered disk, and a primordial scattered disk with the gravitational influence of the giant planets. We show the surface density, Σ, and velocity along the line of sight, $v_{\rm los}$, for face-on and edge-on orientations in each configuration. The times of the simulations are presented in units of the secular

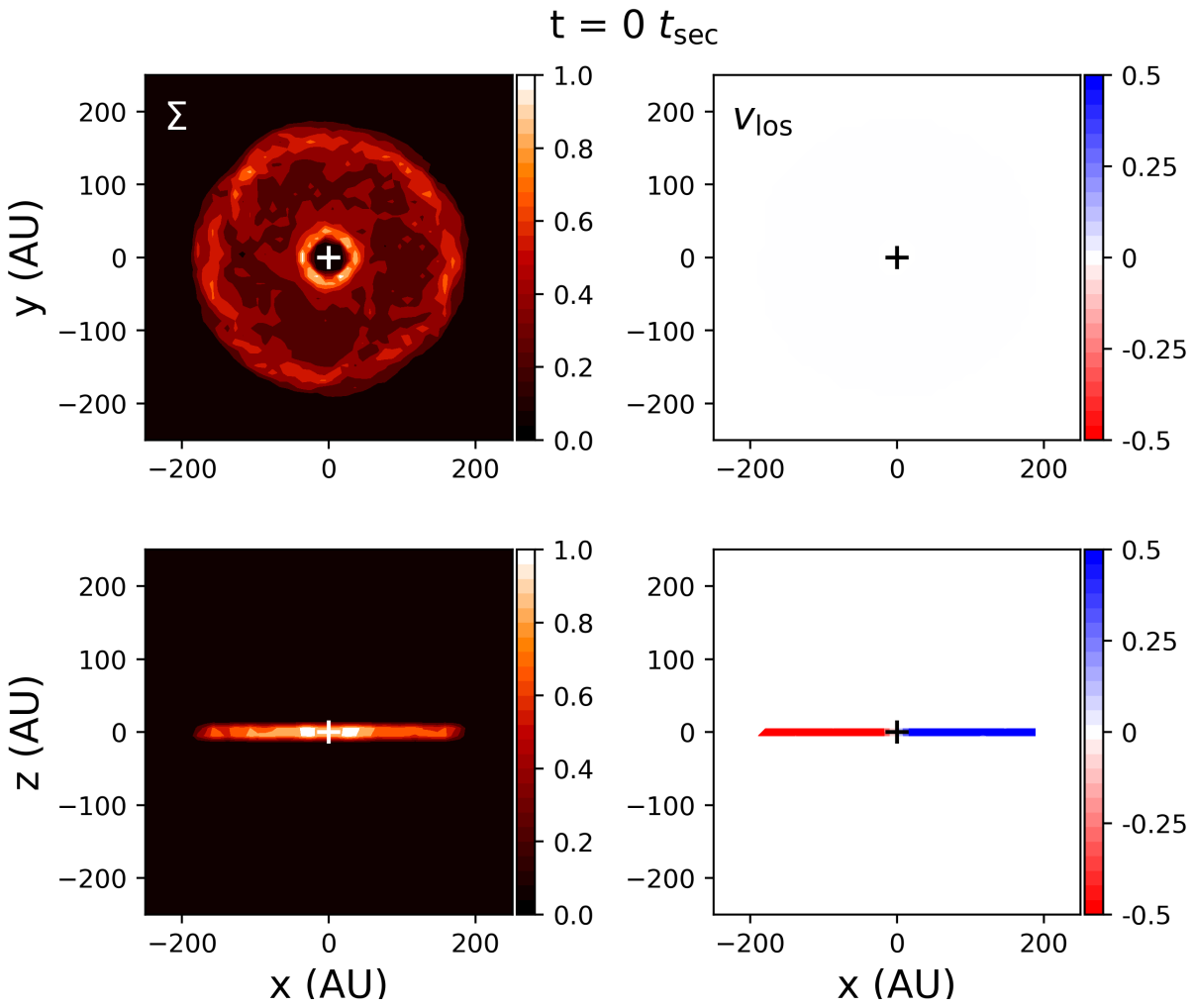

Figure 4.1: A compact disk without J_2 at $t = 0\,t_{\rm sec}$. Plotted are the surface density (left column) and velocity along the line of sight (right column) for both face-on (top row) and edge-on (bottom row) orientations. This figure shows the compact disk in its initial configuration.

timescale given by:

$$t_{\rm sec} \sim \frac{1}{2\pi}\frac{M_\odot}{M_{\rm disk}}P, \tag{4.1}$$

where P is the orbital period at $a = 1$. In this chapter, $M_{\rm disk} = 10^{-3}M_\odot$ so that $t_{\rm sec} \approx 160P$. We scale $a = 1$ to $a = 100$ AU so that an orbital period is then $P = 1000$ yr.

Figures 4.1 through 4.5 show snapshots in time for an idealized, compact disk configuration (pixel resolution 10 AU) without the giant planets. We see that everything evolves

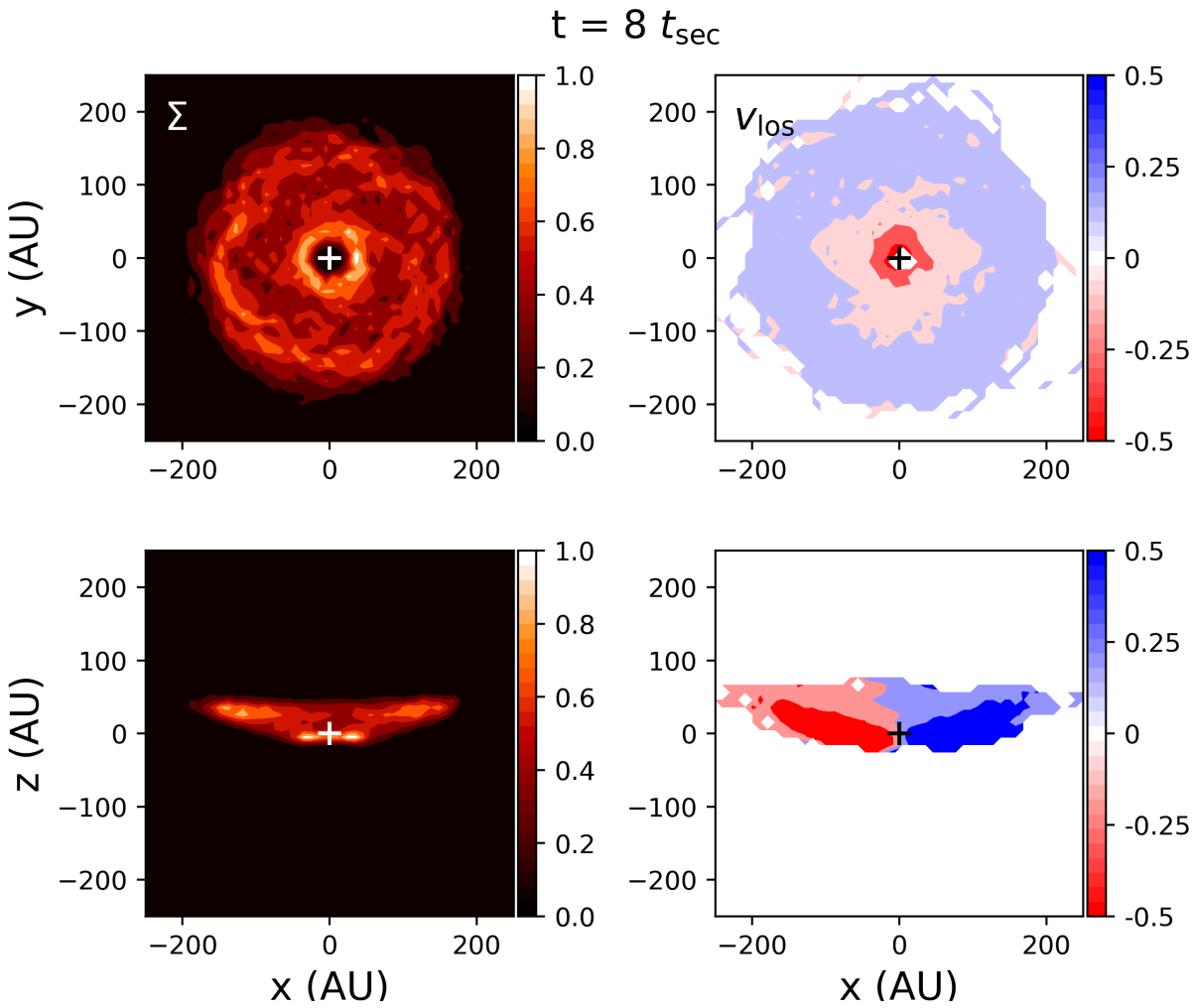

Figure 4.2: A compact disk without J_2 at $t = 8\,t_{\rm sec}$. Plotted are the surface density (left column) and velocity along the line of sight (right column) for both face-on (top row) and edge-on (bottom row) orientations. This figure shows the beginning of the inclination instability, as the orbits begin to form a bowl shape seen in the bottom left panel. The top right panel shows the orbits redshifted in the center and blueshifted at the outer edge.

very quickly in the compact disk configuration.

Figure 4.1 shows the initial conditions of the disk as described in Section 4.2. The left column shows surface density maps and the right column shows line-of-sight velocity maps. The top row shows the disk in a face-on orientation. The bottom row shows the disk in an edge-on orientation. Without the added J2 component, Figure 4.2 shows the beginning of the inclination instability at only 8 secular times. The system reaches peak instability after

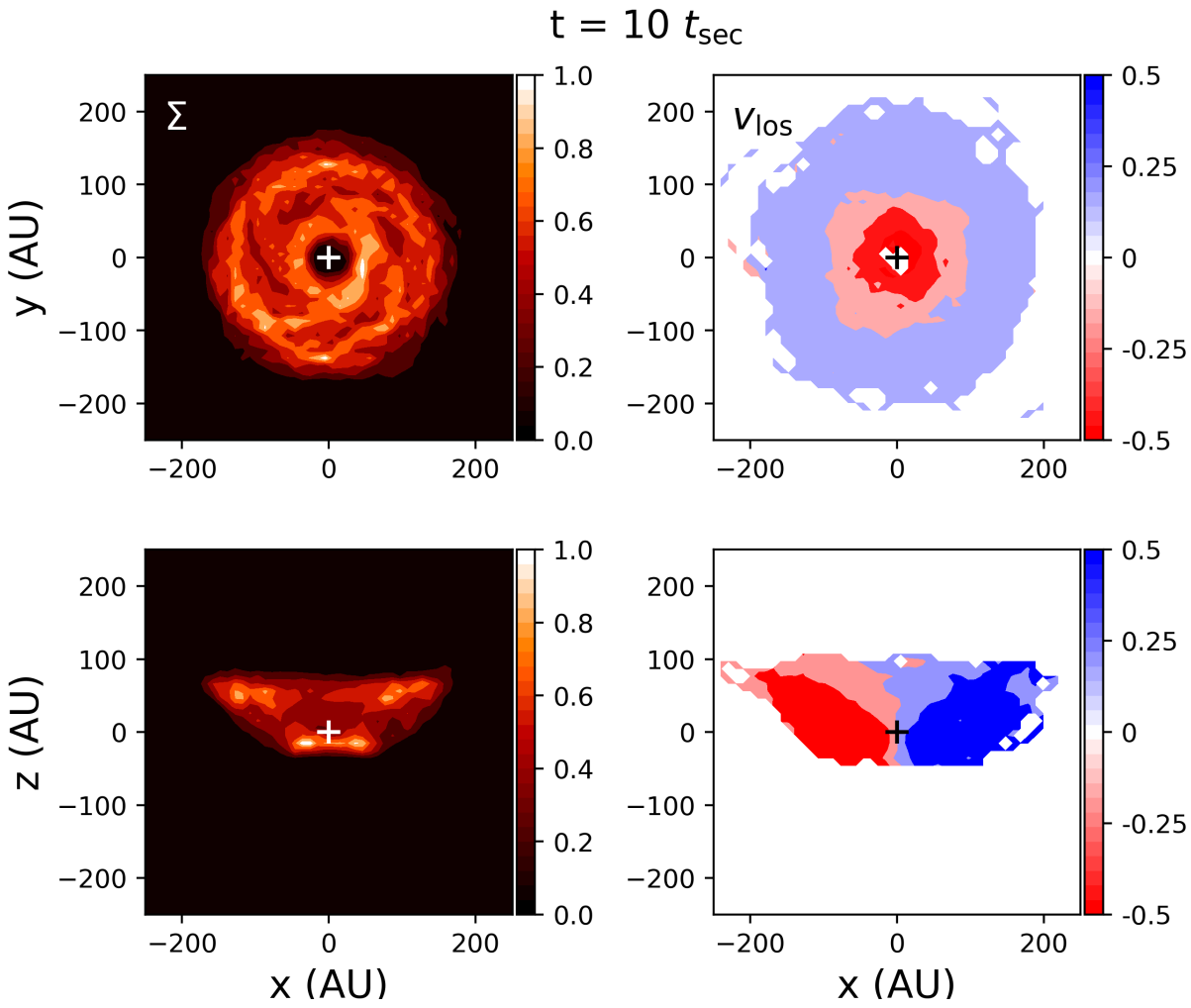

Figure 4.3: A compact disk without J_2 at $t = 10\,t_{\rm sec}$. Plotted are the surface density and velocity along the line of sight for face-on and edge-on orientations. The inclination instability is at its peak.

only 10 secular times in Figure 4.3. The instability is most easily observed in the edge-on view. We see the orbits beginning to lift up out of the x-y plane in Figure 4.2 and the orbits are highly inclined in Figure 4.3. We can also see the instability taking place in the face-on line-of-sight velocity plots. Notice that the inner part of the disk is redshifted, while the outer edge of the disk is blueshifted. This is due to the collective tilt of the orbits as they incline out of the plane. After the inclination instability takes place, we start to see apsidal clustering in the disk. This is shown in Figure 4.4 at 34 secular times. The clustering is best

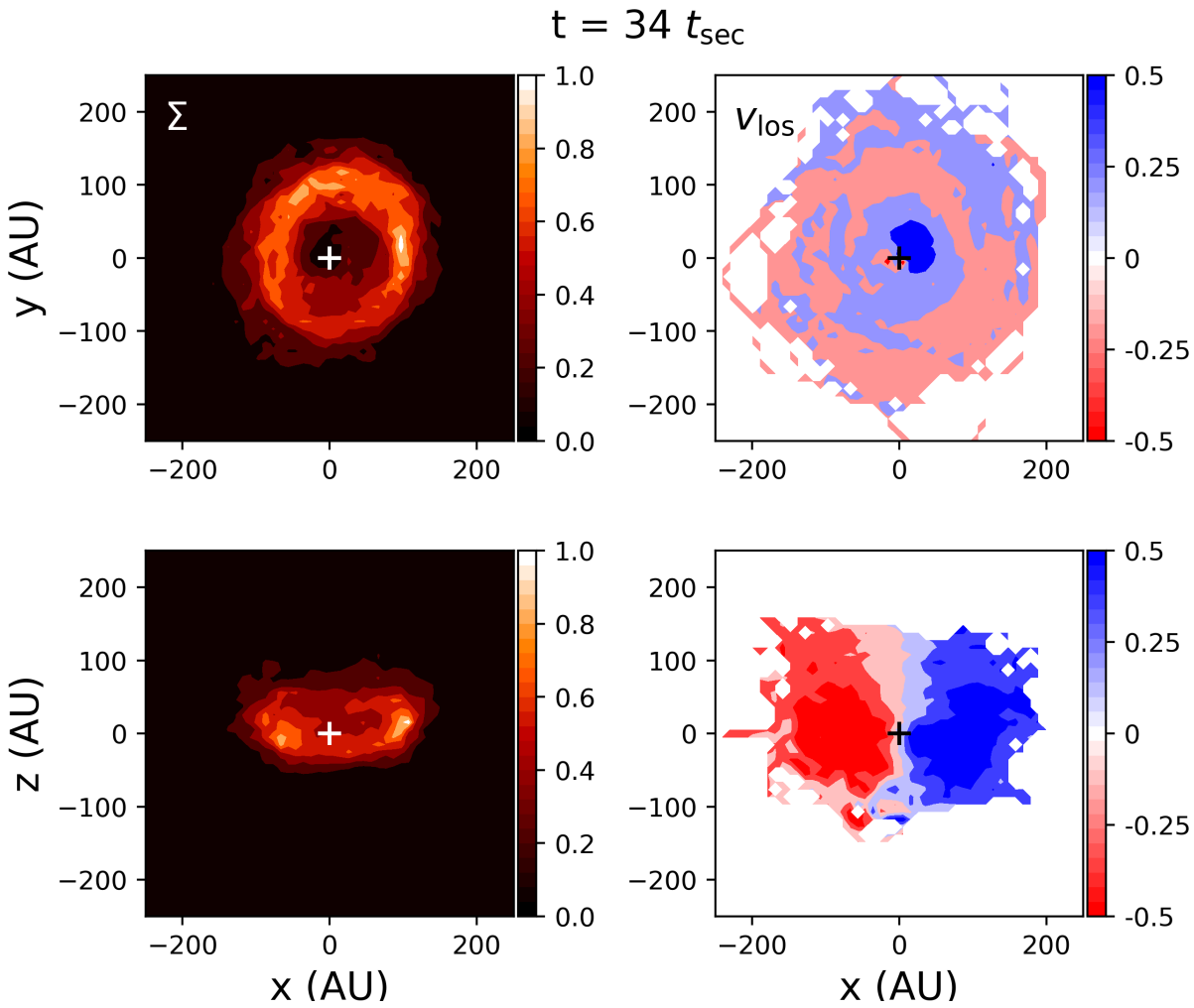

Figure 4.4: A compact disk without J_2 at $t = 34\,t_{\rm sec}$. Plotted are the surface density and velocity along the line of sight for face-on and edge-on orientations. Apsidal clustering is visible in the top left panel.

seen in the face-on surface density plots. In Figure 4.5, we see a very interesting structure in the line-of-sight velocity plot. There is a clear spiral structure in line-of-sight velocity space. This is observed at 79 secular times and persists for about 5 secular times. The spiral structure in velocity space is related to the buckling of the disk into and out of the plane.

We show snapshots in time of a compact disk configuration including the gravitational influence of the giant planets in Figures 4.6 through 4.9. The initial conditions are the same for the compact disk in Figure 4.1. When the gravitational influence of the giant planets

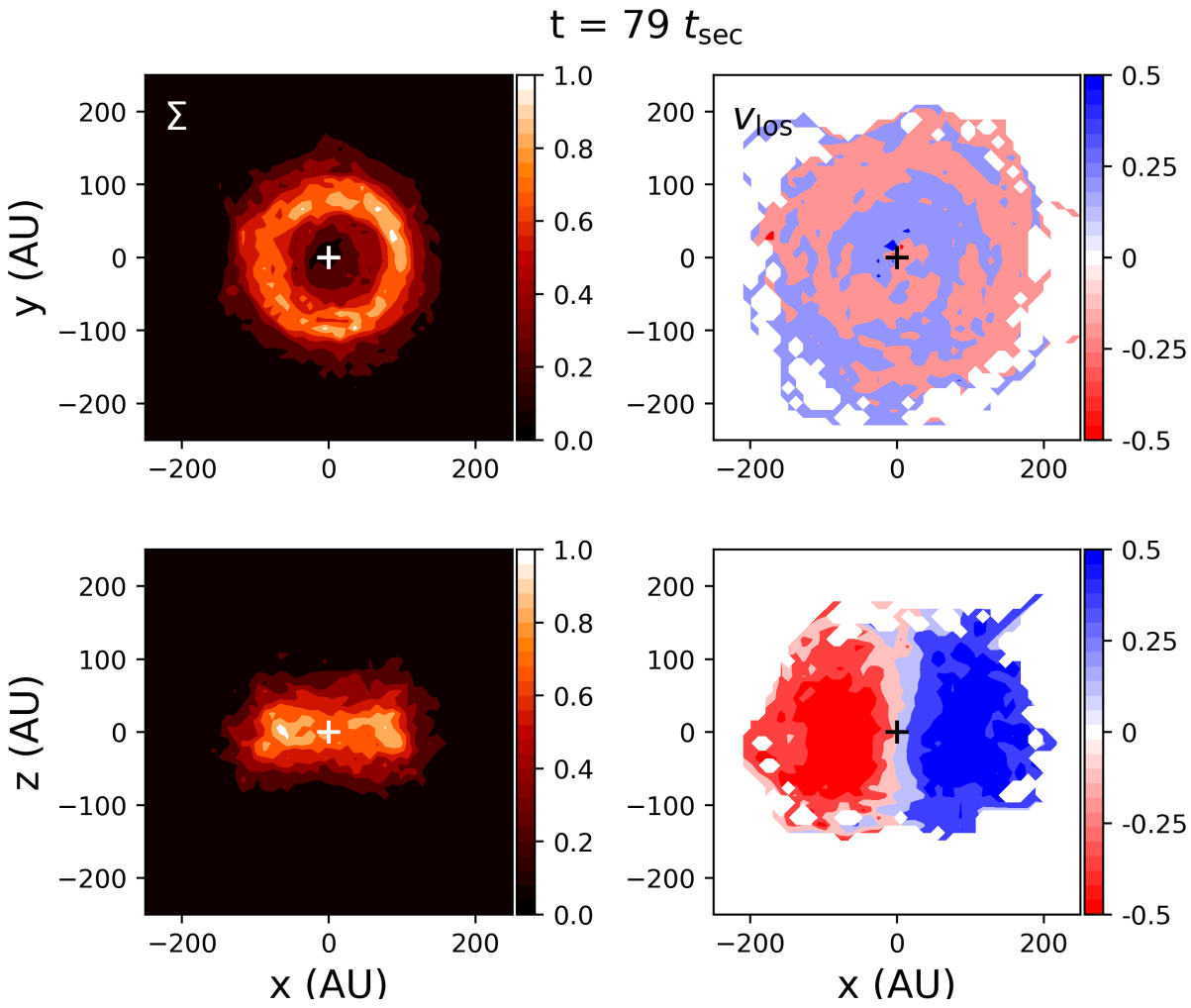

Figure 4.5: A compact disk without J_2 at $t = 79\,t_{\rm sec}$. Plotted are the surface density and velocity along the line of sight for face-on and edge-on orientations. A spiral structure is visible in the top right panel.

is included in the simulation, it takes a longer time for the inclination instability to begin. Figure 4.6 shows the inclination instability occurring at 29 secular times. The top row again shows the face-on view of the disk and the bottom row shows the edge-on view of the disk. We show both surface density (left column) and line-of-sight velocity (right column) maps. Positive velocity is out of the page so that blue indicates blueshifted bodies and red indicates redshifted bodies. We observe again in the line-of-sight velocity plot that the inner portion of the disk is redshifted and the outer edge is blueshifted due to the tilt of the orbits over

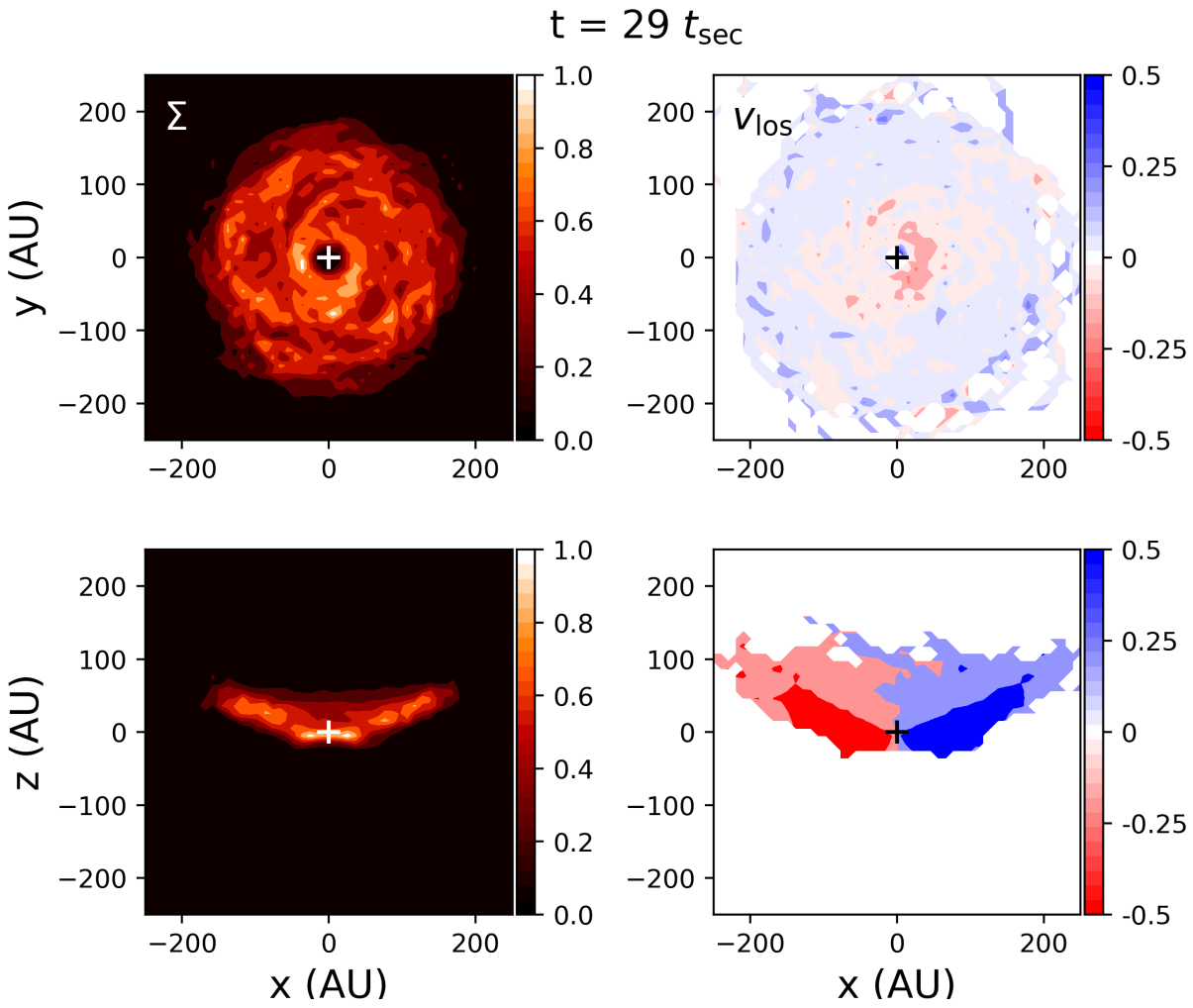

Figure 4.6: A compact disk with J_2 at $t = 29\,t_{sec}$. Plotted are the surface density and velocity along the line of sight for face-on and edge-on orientations. This is the beginning of the inclination instability.

their major axes. This trend continues as the disk reaches peak instability in Figure 4.7. Notice that the inclination instability persists for a much longer time (∼30 secular times) when J_2 is included in the simulation. In Figure 4.8, the inclination instability has gone past the peak and is in the saturated phase. Instead of a bowl, we now see an X-shape in the edge-on surface density plot, reminiscent of the buckling of a stellar bar in a disk galaxy. We also begin to see apsidal clustering in the face-on surface density plot. We continue to see apsidal clustering in Figure 4.9 at 113 secular times, indicating that the apsidal clustering

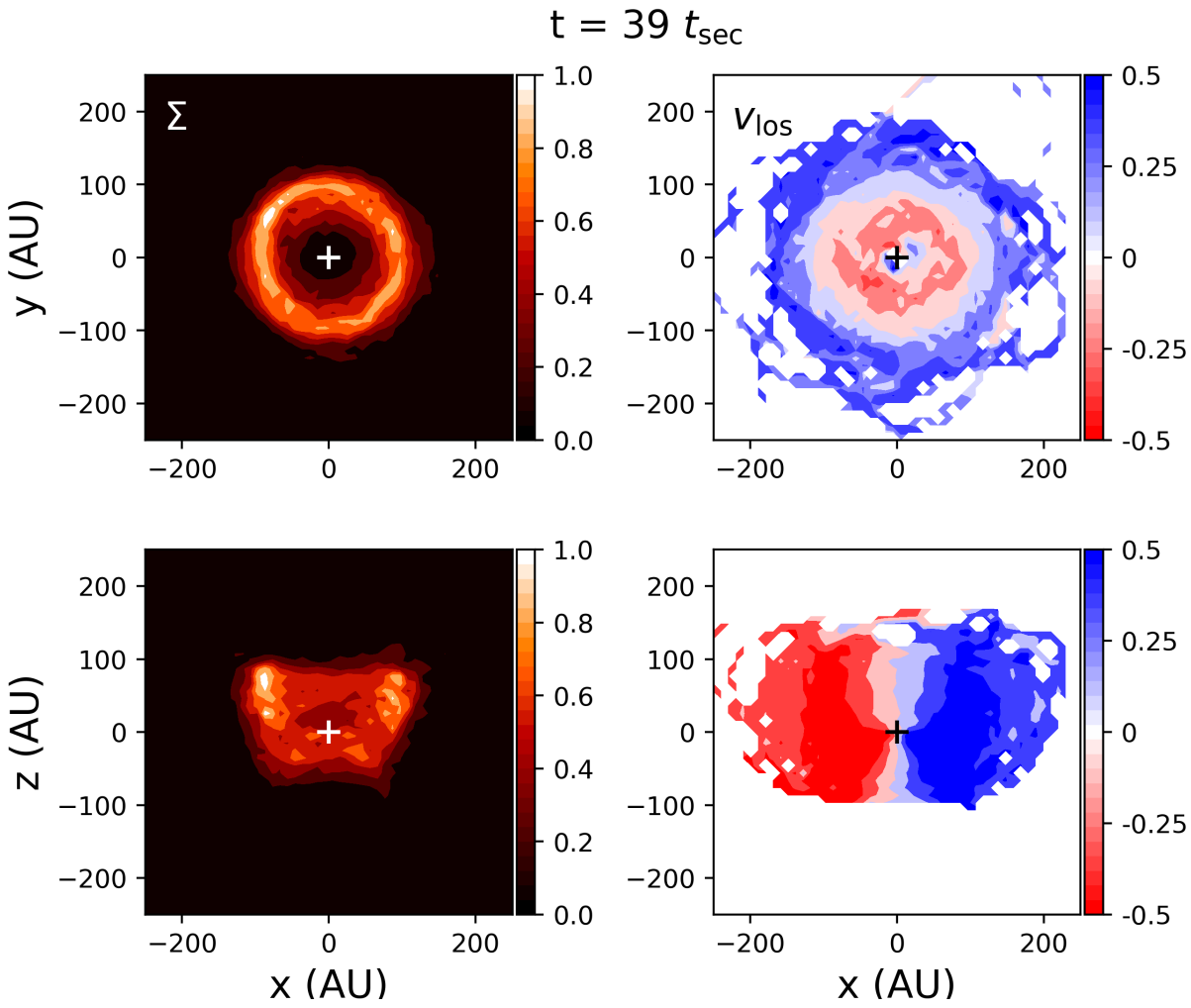

Figure 4.7: A compact disk with J_2 at $t = 39\,t_{\rm sec}$. Plotted are the surface density and velocity along the line of sight for face-on and edge-on orientations. The inclination instability reaches its peak here.

continues for many secular times after the inclination instability.

In Figures 4.10 through 4.15, we show snapshots in time of a more realistic primordial scattered disk (pixel resolution 20 AU), although without the gravitational influence of the giant planets. Figure 4.10 shows the primordial scattered disk in its initial conditions at 0 secular times. These conditions are explained in Section 4.2. Notice the larger scale in AU here in comparison with the compact disk. In the compact disk configuration, we showed that the addition of J_2 increased the time for the inclination instability to form

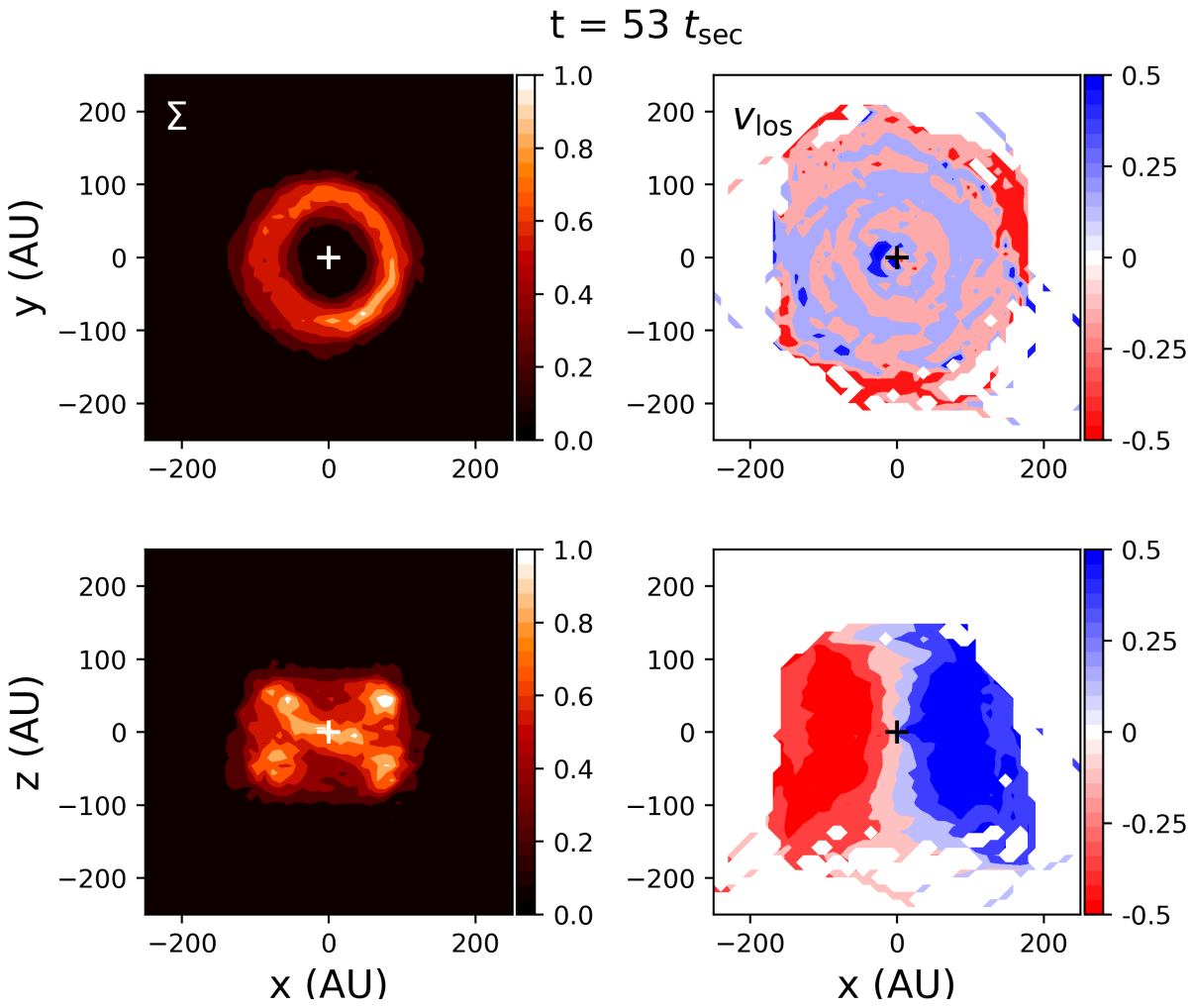

Figure 4.8: A compact disk with J_2 at $t = 53\,t_{\rm sec}$. Plotted are the surface density and velocity along the line of sight for face-on and edge-on orientations. Apsidal clustering is present and visible in the top left panel.

and the amount of time the instability was present for. Here we show that the effects of the inclination instability take much longer to appear in the primordial scattered disk as compared with the compact disk configuration. This is due to the lower mass density in this configuration. We see in Figure 4.11 that the inclination instability does not begin until about 80 secular times. Again, with the inclination instability beginning, the center of the disk becomes redshifted, seen in the face-on line-of-sight velocity plot. Figure 4.12 shows the simulation during the inclination instability about 20 secular times later. At 122 secular

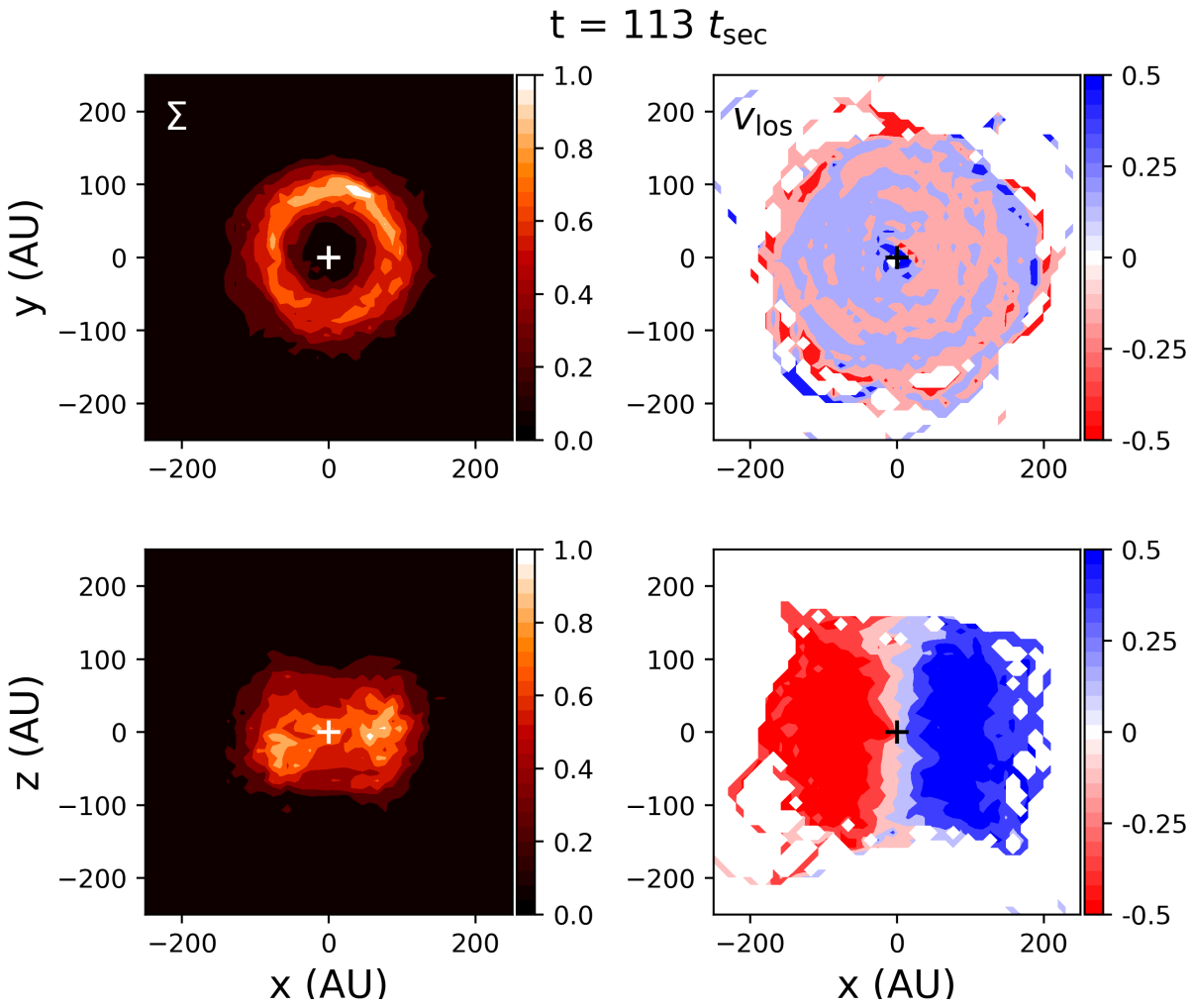

Figure 4.9: A compact disk with J_2 at $t = 113\,t_{sec}$. Plotted are the surface density and velocity along the line of sight for face-on and edge-on orientations. Apsidal clustering is visible in the top left panel.

times, in Figure 4.13, we see the X-shape in the edge-on surface density distribution as the inclination instability reaches the saturation phase. The inclination instability causes the orbits to lift off the plane into a bowl shape. In Figure 4.14, the orbits dip down across the disk plane, creating an upside down bowl shape as shown in the edge-on surface density plot. The orbital precession of orbits cause this back and forth oscillation of the bowl shape across the plane of the original disk. We also see that apsidal clustering is beginning to be present here, shown in the face-on view of the surface density plot. At 187 secular times, shown

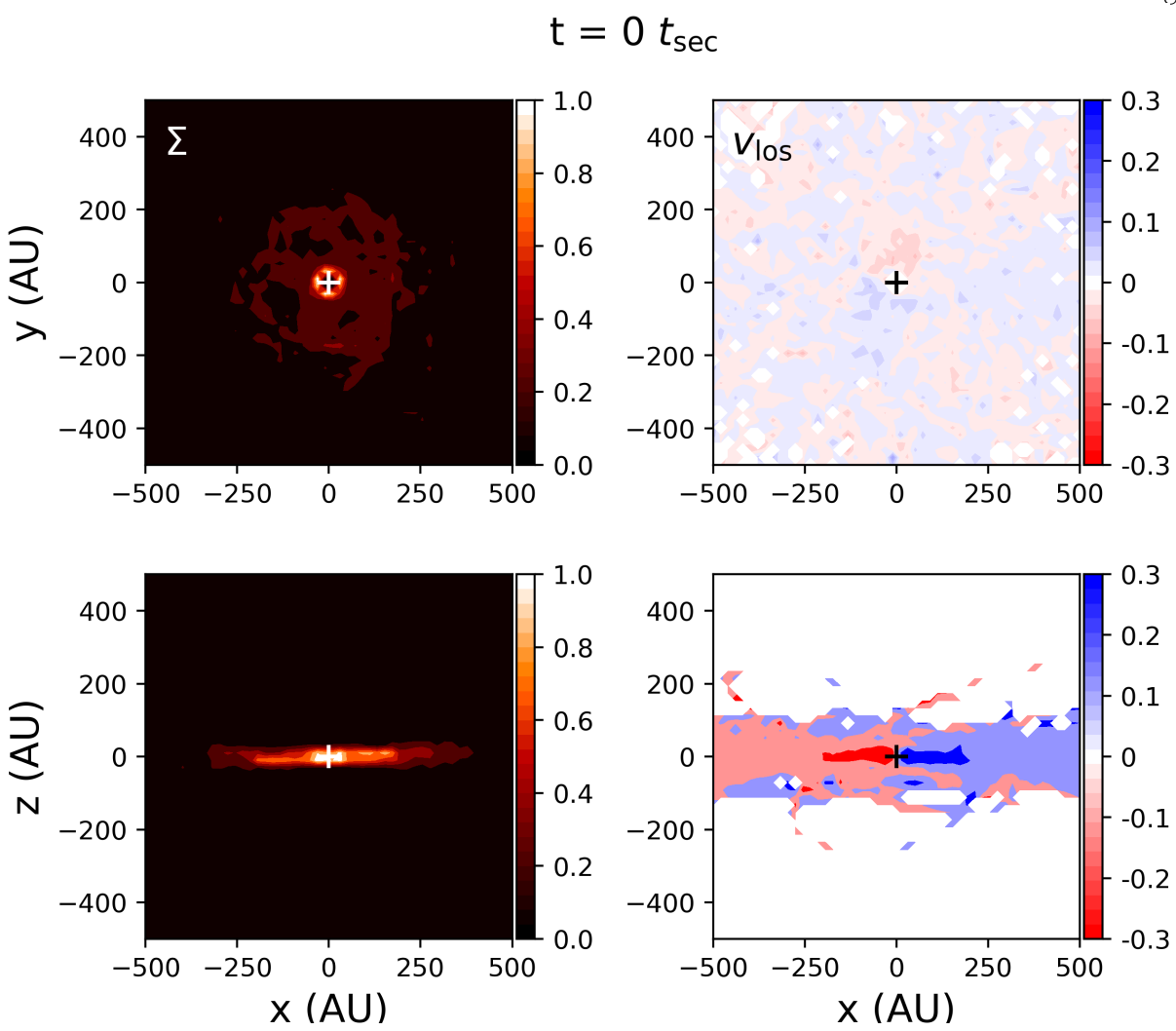

Figure 4.10: A scattered disk without J_2 at $t = 0\,t_{sec}$. Plotted are the surface density and velocity along the line of sight for face-on and edge-on orientations. Here we show the initial conditions for the primordial scattered disk.

in Figure 4.15, apsidal clustering in the primordial scattered disk is still present, lasting for many secular times.

We show snapshots in time for a primordial scattered disk including the gravitational influence of the giant planets in Figures 4.16 through 4.19. It is important to notice that the scattered disk with J_2 included takes much longer to reach the inclination instability and to evolve than the compact disk as well as the scattered disk without J_2. The disk without J2 reaches peak instability around 100 secular times, while the disk with J2 takes

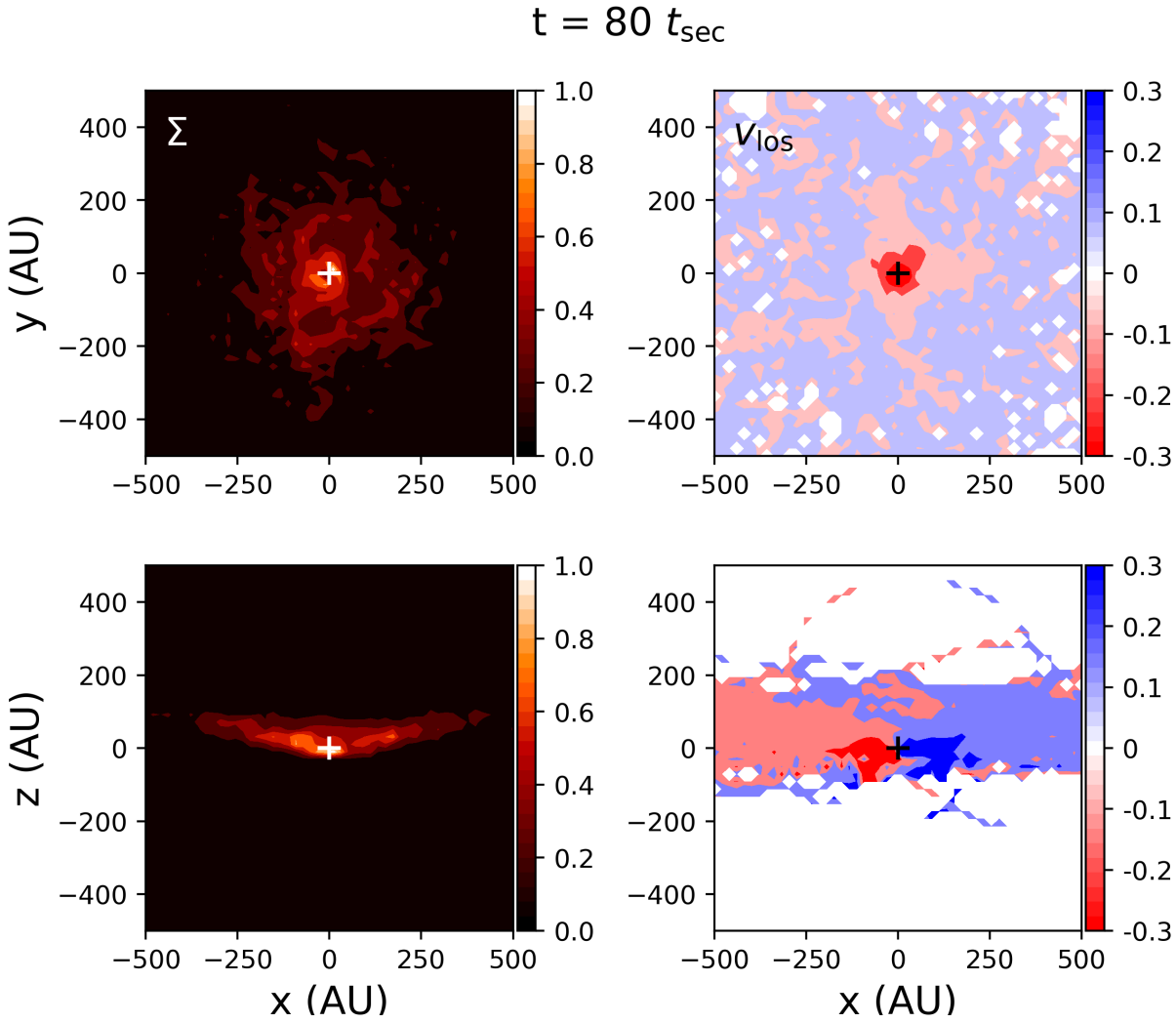

Figure 4.11: A scattered disk without J_2 at $t = 80\,t_{\rm sec}$. Plotted are the surface density and velocity along the line of sight for face-on and edge-on orientations. Here, the inclination instability is beginning to take effect.

until about 200 secular times to reach the peak instability and the saturation phase. The initial primordial scattered disk setup with J_2 is the same as in Figure 4.10. The initial conditions for this setup are explained in Section 4.2. It takes close to 200 secular times for the inclination instability to take place. This is shown in Figure 4.16. Just as in the other simulations, when the instability occurs we see the orbits lift out of the plane in the edge-on surface density plot. We also see the inner disk redshifted and the outer portion of the disk blueshifted due to the collective tilting of the orbits. In Figure 4.17, around 300

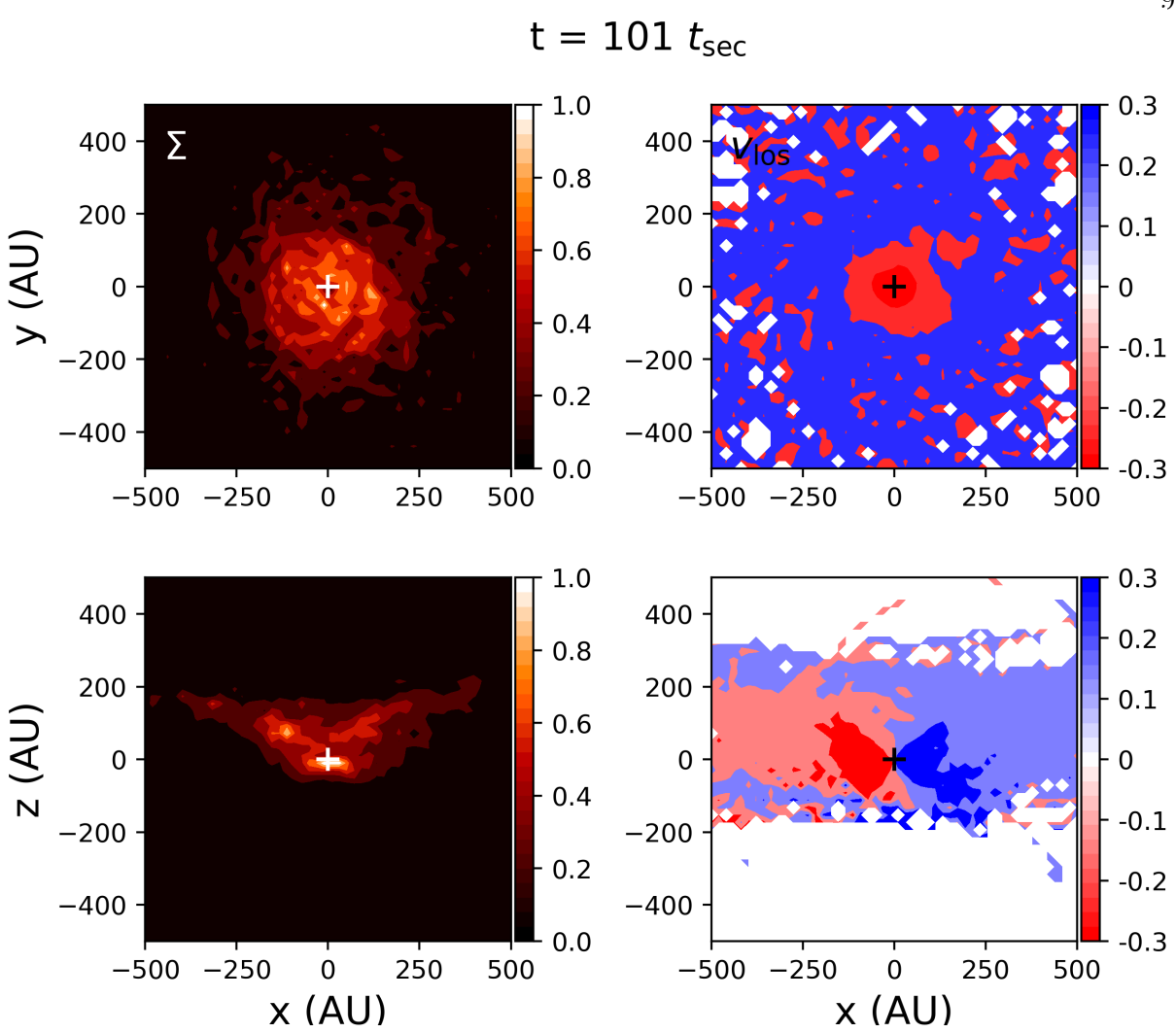

Figure 4.12: A scattered disk without J_2 at $t = 101\,t_{\rm sec}$. Plotted are the surface density and velocity along the line of sight for face-on and edge-on orientations. This figure shows the inclination instability at its peak.

secular times, we see a very strong spiral signature in the face-on line-of-sight velocity plot. We also see apsidal clustering at this time in the face-on surface density plot. The peak of the spiral in velocity space is offset from the peak in surface density, indicating that these structures are unrelated. The spiral occurs as the orbits roll through 0° inclination around their major axes. This is evident in the fact that the concentric circles of redshifted and blueshifted bodies are reversed after the spiral has saturated. At this point in time, the inclination instability is past its peak and is in the saturated phase. Figures 4.18 and 4.19

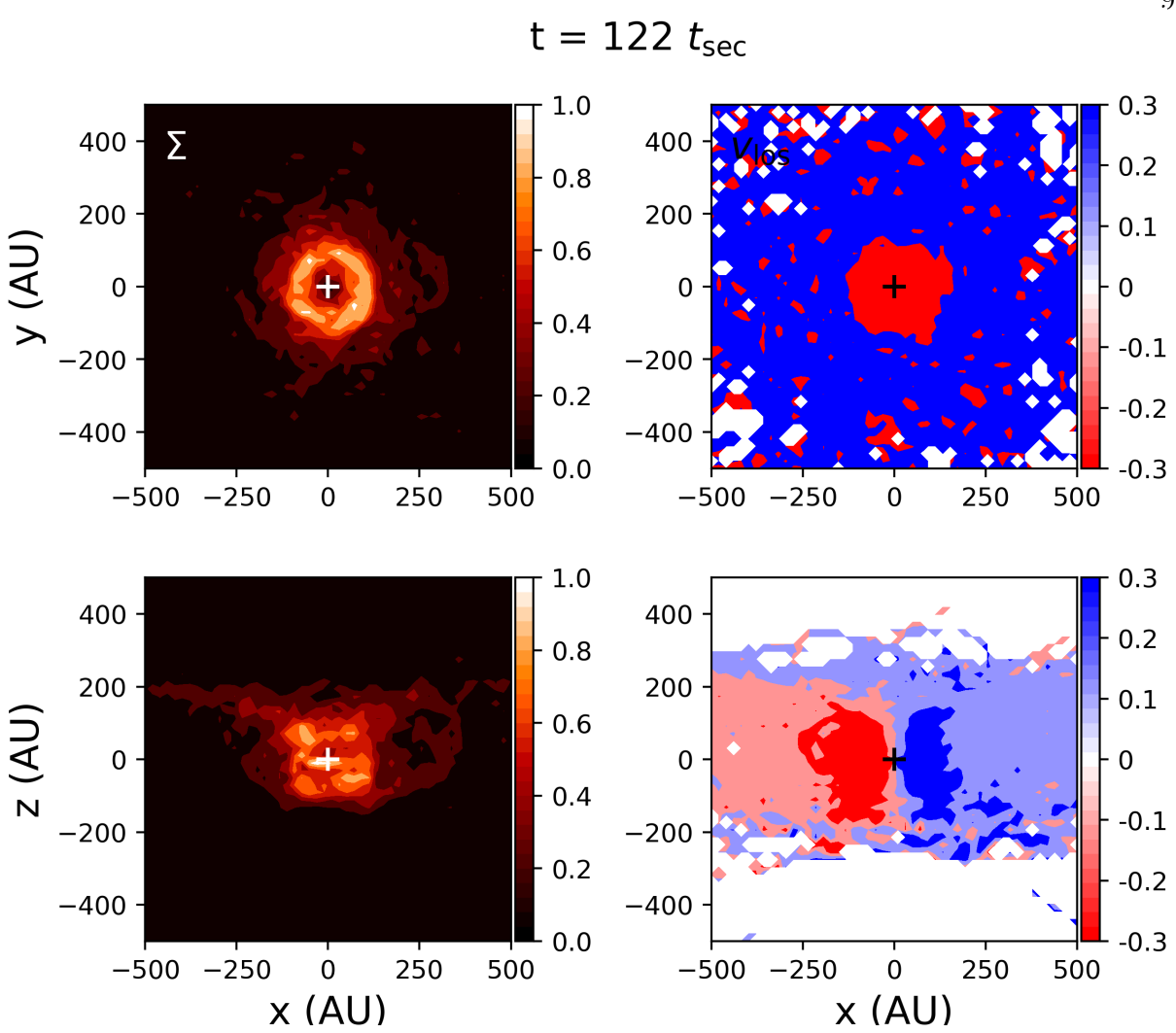

Figure 4.13: A scattered disk without J_2 at $t = 122\,t_{\rm sec}$. Plotted are the surface density and velocity along the line of sight for face-on and edge-on orientations.

show strong apsidal clustering that precesses and lasts for at least 300 secular times, until the end of the simulation.

4.4 Discussion

In this chapter, we explore the dynamics of the collective gravity of high eccentricity orbits in an axisymmetric near-Keplerian disk. Specifically, we look at the surface density and line-of-sight velocity maps of the axisymmetric disk over time for four different configurations.

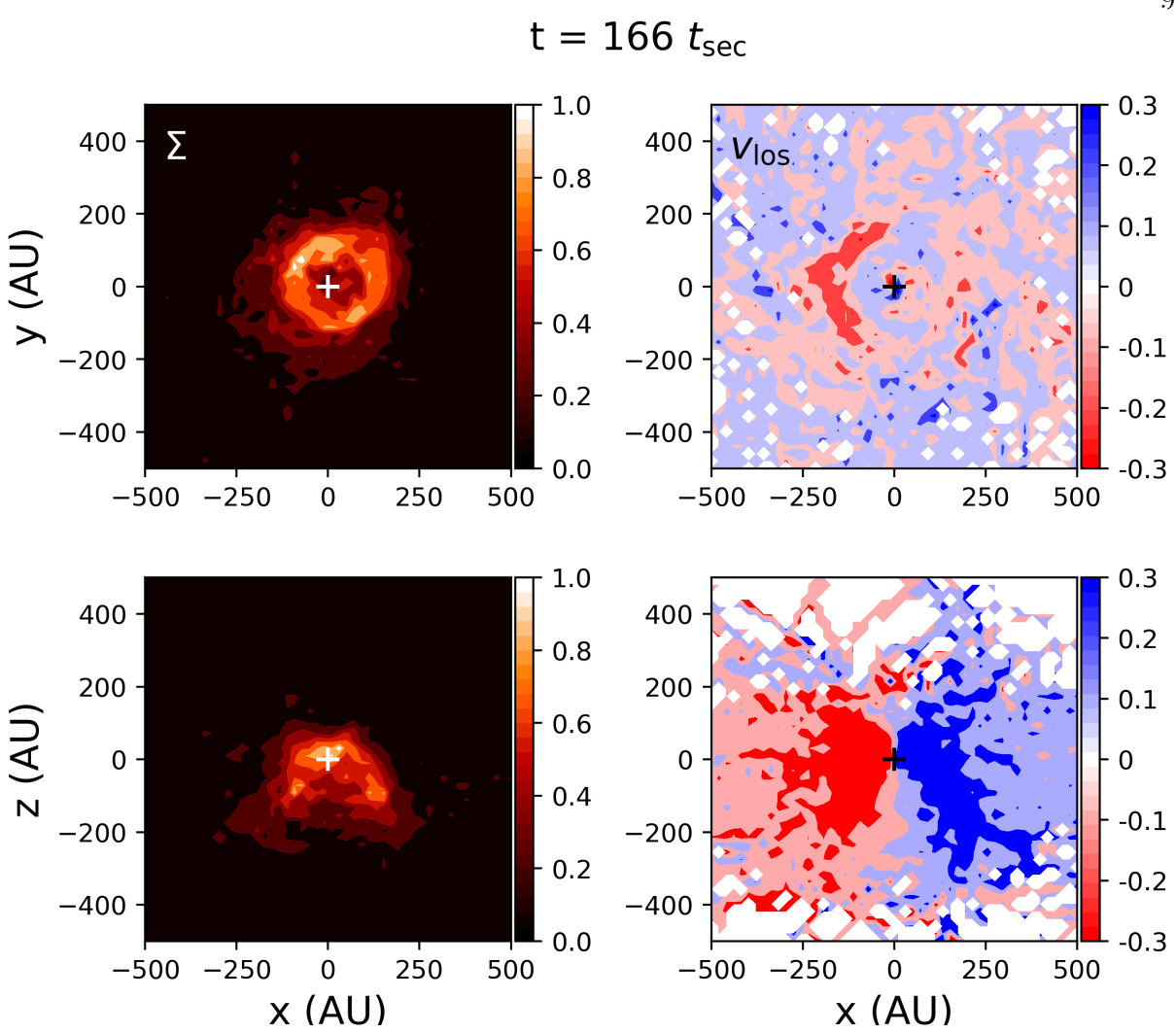

Figure 4.14: A scattered disk without J_2 at $t = 166\,t_{sec}$. Plotted are the surface density and velocity along the line of sight for face-on and edge-on orientations.

The line-of-sight velocity maps, especially, offer a new look at a system undergoing the inclination instability. Our findings point to the following conclusions:

(1) Apsidal clustering of the orbits of small bodies occurs in fully interacting N-body simulations of a primordial scattered disk that includes the gravitational influence of the Solar System's giant planets. The apsidal clustering begins after the inclination instability has saturated, but the instability is principal to the formation of the apsidal clustering.

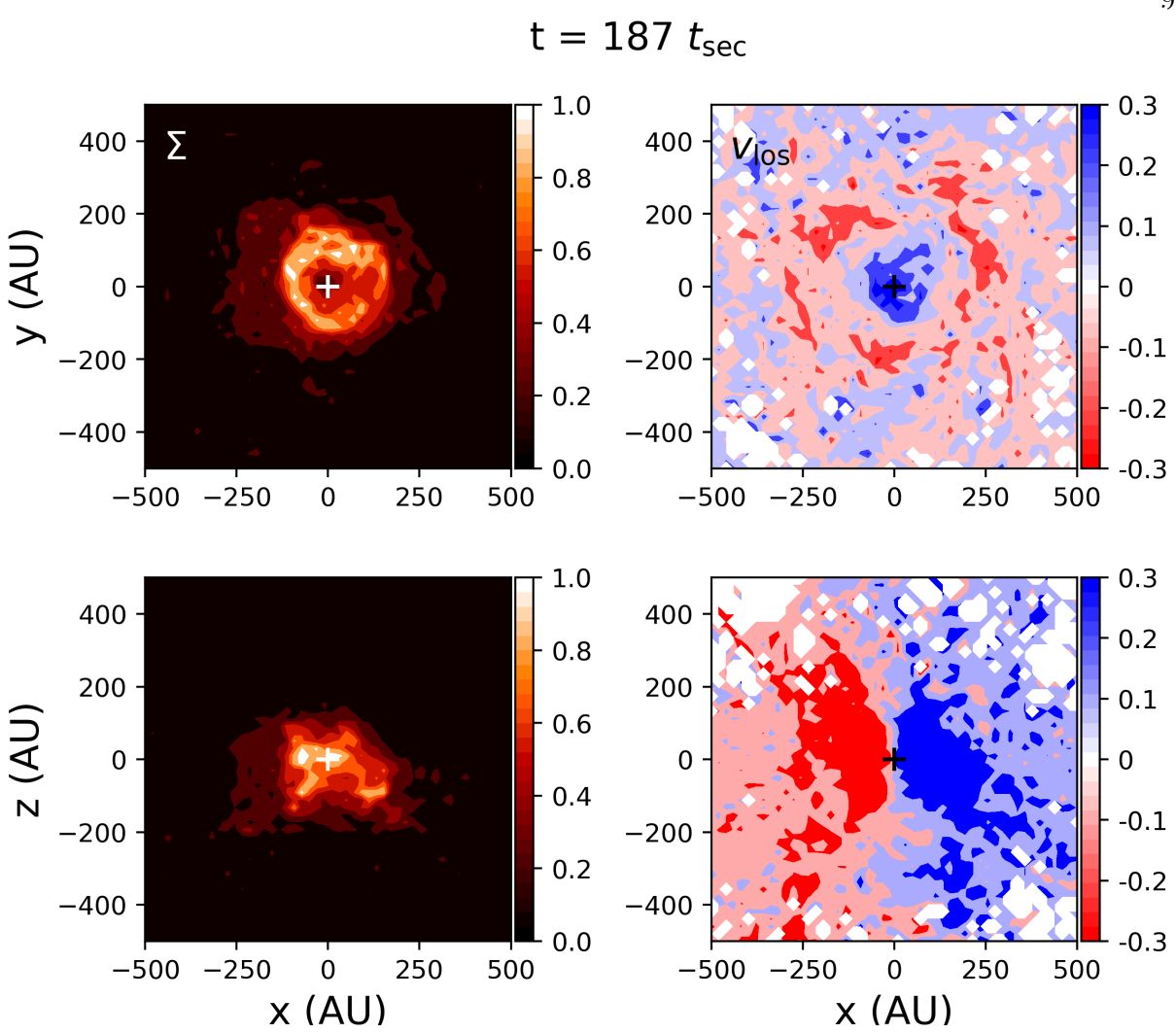

Figure 4.15: A scattered disk without J_2 at $t = 187\,t_{\rm sec}$. Plotted are the surface density and velocity along the line of sight for face-on and edge-on orientations. Apsidal clustering is visible in the top left panel.

(2) Apsidal clustering also occurs in a disk without the added influence of the giant planets, as shown in Zderic et al. (2020) and confirmed here.

(3) We confirm that the addition of a quadrupole J_2 moment increases the length of time that apsidal clustering persists after the inclination instability has saturated. In a full N-body simulation of a primordial scattered disk with the gravitational influence of the giant planets, apsidal clustering persists for at least 300 secular times.

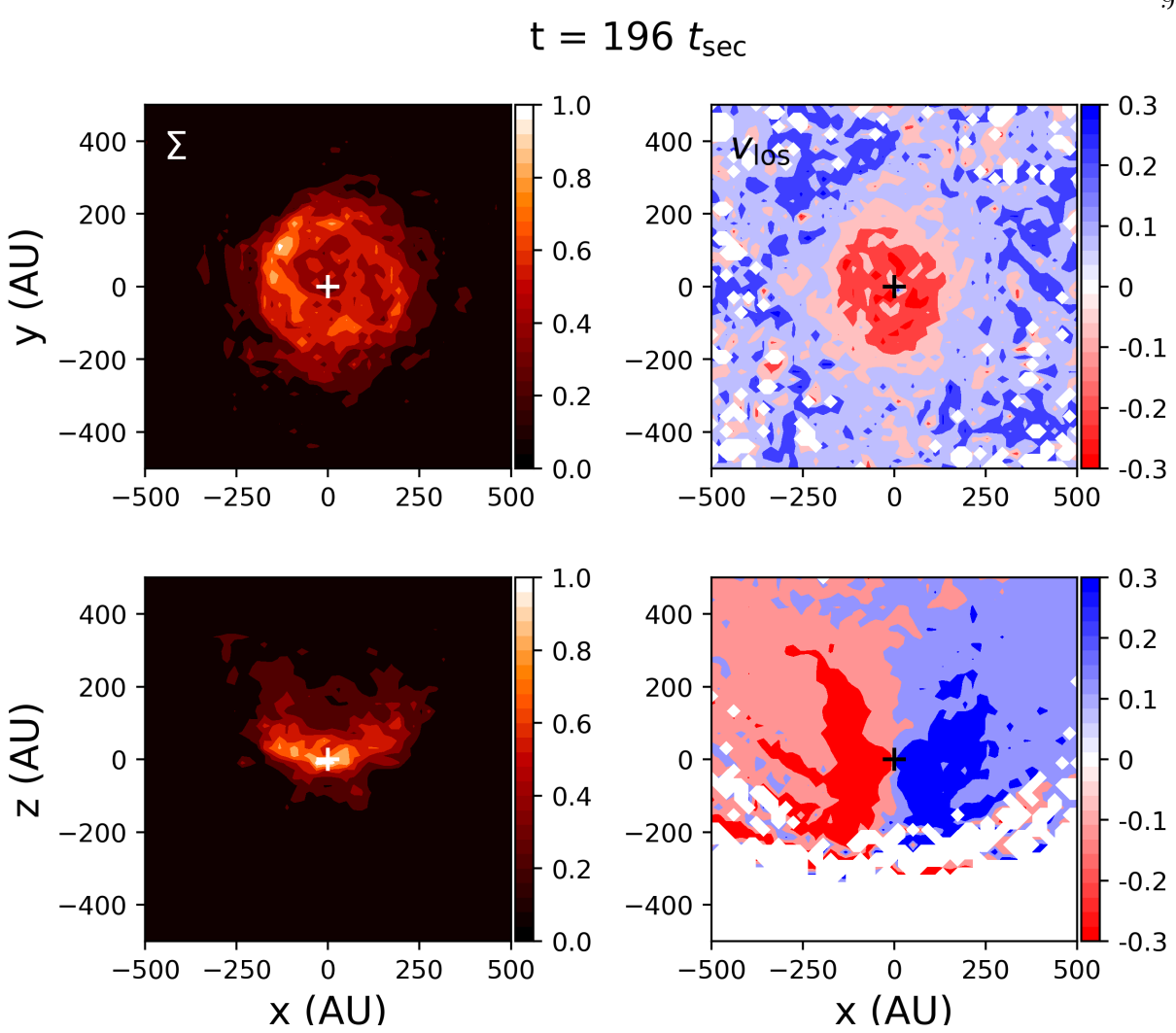

Figure 4.16: A scattered disk with J_2 at $t = 196\,t_{sec}$. Plotted are the surface density and velocity along the line of sight for face-on and edge-on orientations. The inclination instability occurs around 196 secular times.

(4) We show that during the inclination instability, the center of an axisymmetric disk becomes redshifted, while the outer edges of the disk are blueshifted (or vice versa). This confirms that the eccentric orbits tilt over their major axes in a coherent manner as indicated by the clustering in argument of pericenter.

(5) In addition to apsidal clustering, we also show the formation of spiral arms in the line-of-sight velocity space of a scattered disk of a planetary system. This is due to

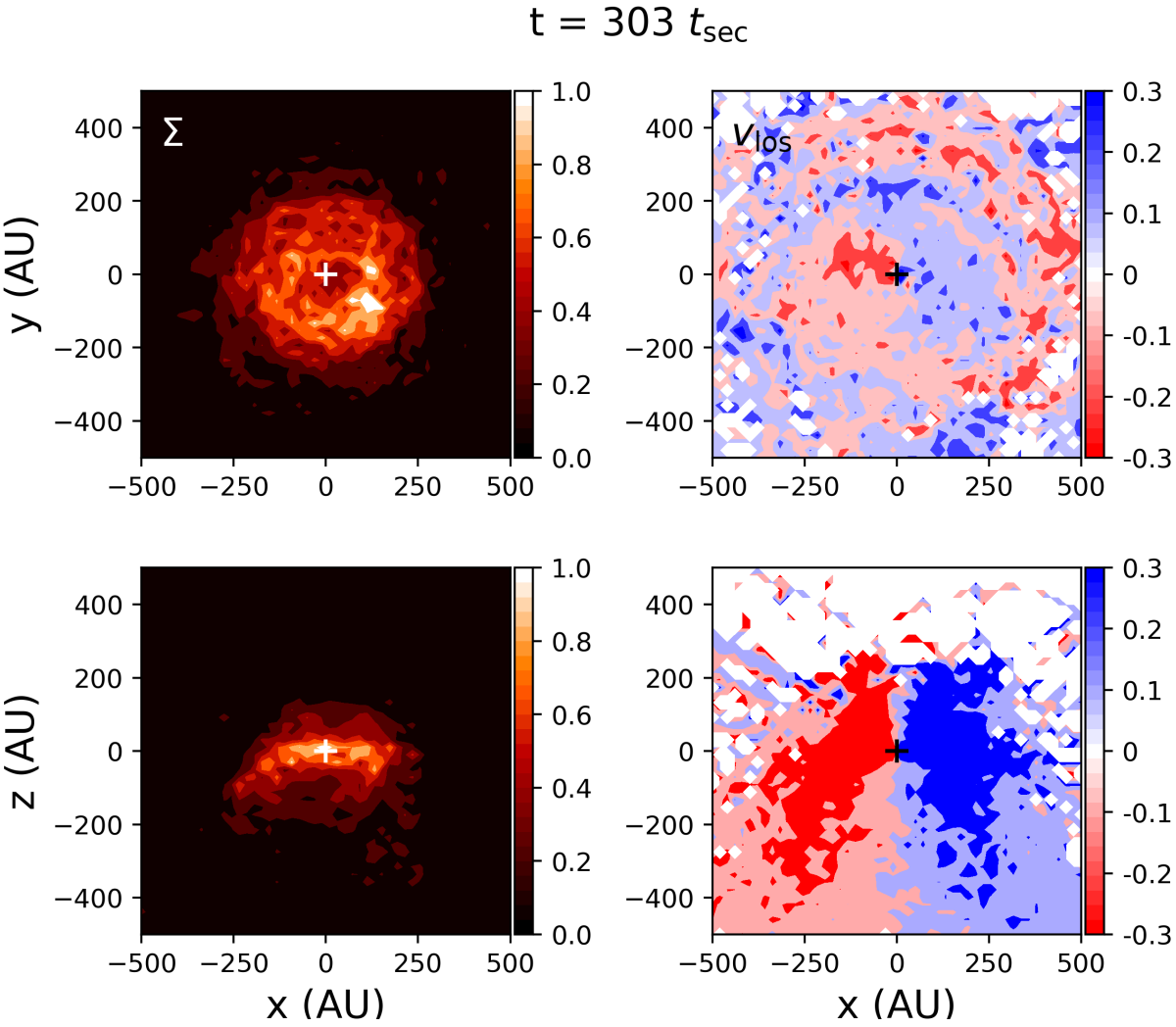

Figure 4.17: A scattered disk with J_2 at $t = 303\,t_{\rm sec}$. Plotted are the surface density and velocity along the line of sight for face-on and edge-on orientations. A strong spiral feature is observed in the face-on line-of-sight velocity plot. Apsidal clustering is also observed in face-on surface density plot.

the collective rolling of orbits over their major axes as they buckle into and out of the plane. Rosotti et al. (2020) have even already observed spiral arms in the surface density of a protoplanetary disk.

The saturation timescale, or the time for the disk to go through the inclination instability and to develop apsidal clustering, is $\lesssim 660$ Myr, which is much less than the age of the solar system. If the outer solar system underwent the inclination instability, apsidal

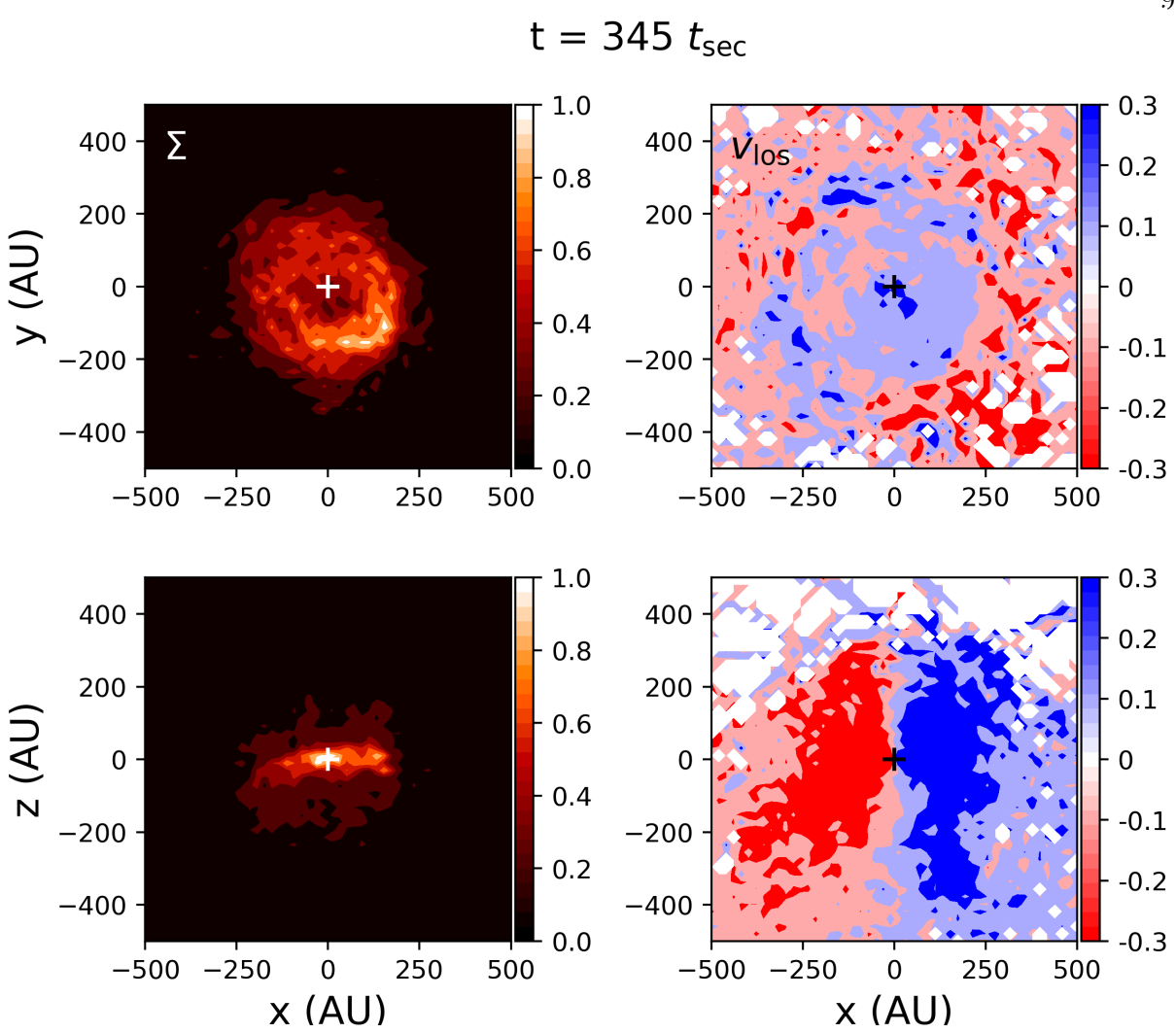

Figure 4.18: A scattered disk with J_2 at $t = 345\,t_{\rm sec}$. Plotted are the surface density and velocity along the line of sight for face-on and edge-on orientations. Strong apsidal clustering is visible in the top left panel.

clustering should be present today. Apsidal clustering or lopsidedness in a protoplanetary disk is essentially an eccentric nuclear disk. This means that an eccentric nuclear disk of icy bodies likely exists in our outer solar system. We predict that many minor planets exist beyond the Kuiper Belt. In fact, nearly 200 minor planets have been discovered with large semi-major axes in recent years, even though these objects are very difficult to find. In the future we will use the LSST survey simulator to confirm that our predicted lopsided disk of eTNOs will be accessible to the Vera Rubin Observatory due to come online in 2022.

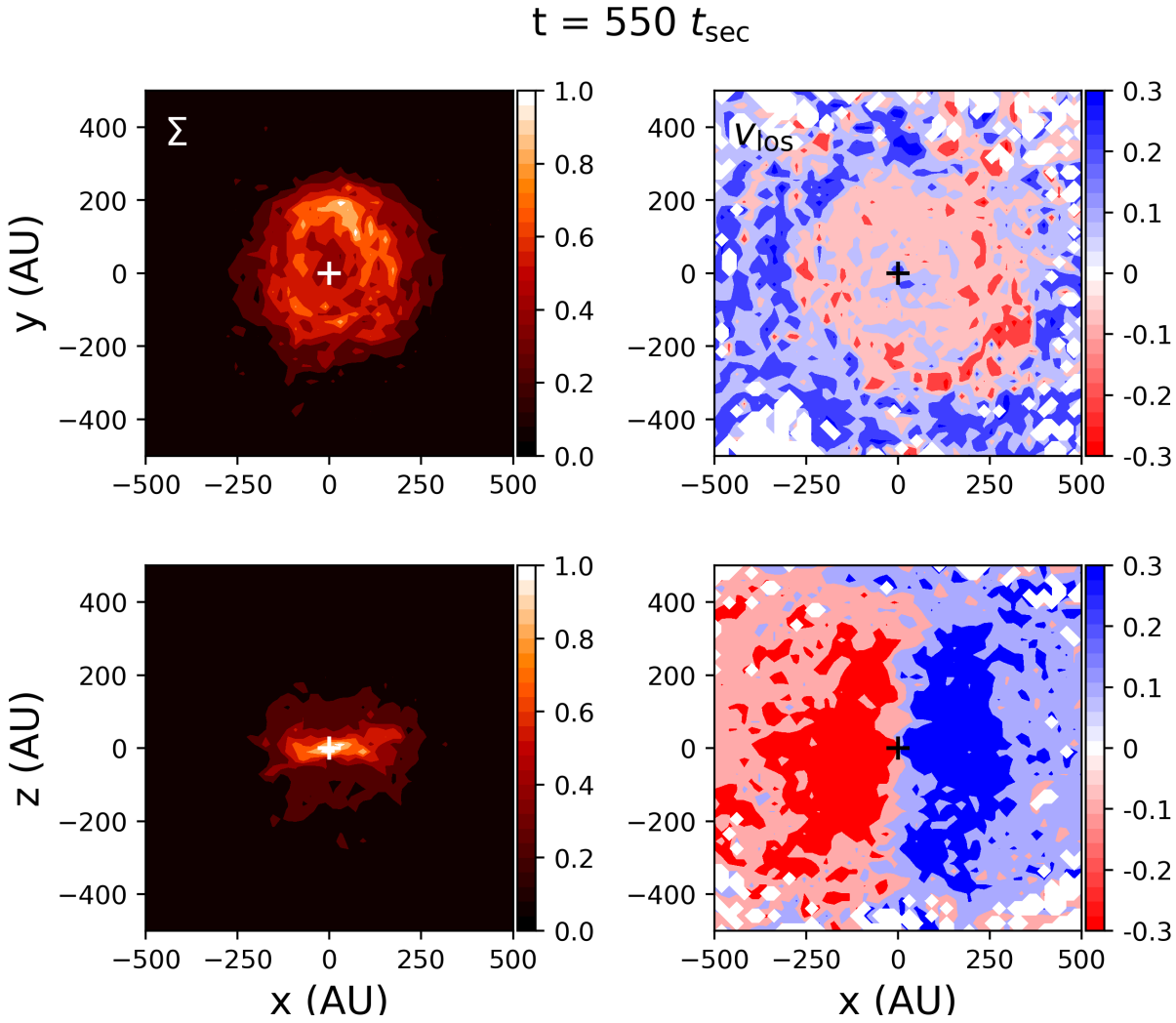

Figure 4.19: A scattered disk with J_2 at $t = 550\,t_{\rm sec}$. Plotted are the surface density and velocity along the line of sight for face-on and edge-on orientations.

Chapter 5

Conclusion

In this thesis, I provide further insight into the gravitational dynamics of many particles orbiting a central body. I study the motions of stars orbiting a supermassive black hole as well as minor planets orbiting a star on eccentric orbits. The gravitational relaxation of a spherically symmetric, isotropic cluster of bodies orbiting a central object has been studied extensively, and has been the default assumption for the distribution of stars around a supermassive black hole at the center of galaxies. With recent evidence that the centers of galaxies are not all spherically symmetric, I focus on the dynamics of massive eccentric nuclear disks, which are apsidally-aligned disks of stars. I run fully interacting N-body simulations so that the disks are self-gravitating. A primary motivation for this thesis work is the observed double nucleus in our nearest galactic neighbor, Andromeda (M31), which is well explained by an eccentric nuclear disk. The M31 nucleus has been an exciting topic since the day it was first observed and it continues to inspire us as we endeavor to explain the dynamics of eccentric nuclear disks.

In Chapter 2, I focused on tidal disruption events (TDEs) from eccentric nuclear disks. A TDE occurs when a star is torn apart by a black hole's tidal gravitational force. I ran N-body simulations of eccentric nuclear disks in both Newtonian gravity and with general relativistic precession. The same secular mechanism that keeps eccentric nuclear disks stable results in extremely high TDE rates. General relativistic precession does not decrease the TDE rate relative to that in Newtonian gravity because an eccentric nuclear disk is a

system in the full loss cone regime. I show that TDEs preferentially disrupt at 0° and 180° inclination, meaning that the orbits flip over their major axes and the stars disrupt in the disk plane. I also show that eccentric nuclear disks have a non-negligible fraction of retrograde orbiting stars (10%), mostly lying at the inner edge of the disk. Furthermore, I show that orbital elements between successive TDEs from eccentric nuclear disks are correlated, potentially resulting in unique observational signatures including overlapping TDE streams. We anticipate observing more and more TDEs (especially from eccentric nuclear disks) with the LSST on the Vera Rubin Observatory.

Given the importance of eccentric nuclear disks for TDE production and evidence that they are common in the local universe, Chapter 2 naturally leads into Chapter 3 as I seek to determine what astronomers should look for in order to observe eccentric nuclear disks in distant galactic nuclei. I present surface density plots, line-of-sight velocity plots, as well as velocity dispersion, skew, and kurtosis maps of eccentric nuclear disks viewed from many different orientations. I show that an eccentric nuclear disk can appear as a double nucleus, an offset nucleus, or a centered nucleus, but will appear most frequently as an offset nucleus. Additionally, stellar mass segregation will affect the mass to light ratio of the two brightness peaks. I show interesting features in the line-of-sight velocity and velocity dispersion maps including lower values in line-of-sight velocity than a circular disk due to the stars spending most of their time at apocenter. An eccentric nuclear disk also has a higher velocity dispersion than a circular disk with a peak that does not typically match the peak in photometry.

In Chapter 4, I use my method of "observing" eccentric nuclear disks from Chapter 3 to observe a disk of minor planets in the outer Solar System. I observe an axisymmetric disk in four different configurations including a compact disk and a primordial scattered disk both with and without the gravitational influence of the giant planets. An axisymmetric disk of eccentric orbits undergoes an instability in which the orbits collectively incline and tilt coherently over their major and minor axes. I show that apsidal clustering is long-lasting in a

primordial scattered disk with the gravitational influence of the giant planets. I confirm that the addition of a quadrupole J_2 moment to the central body increases the length of time that apsidal clustering persists after the inclination instability has saturated. Apsidal clustering is a lopsided $m = 1$ mode, which is an eccentric nuclear disk. Formation of an eccentric nuclear disk in the outer solar system takes us back to Chapter 2, as it could indicate the possibility for tidally disrupting objects from the outer Solar System. The trans-Neptunian scattered disk is likely where some comets that approach the Sun originate. An eccentric nuclear disk of icy bodies likely exists in our outer Solar System. We predict that many minor planets exist beyond the Kuiper Belt. In fact, nearly 200 minor planets have been discovered with large semi-major axes in recent years, even though these objects are very difficult to find. In addition to apsidal clustering, I show the formation of spiral structures in the line-of-sight velocity space. The spiral structure is related to the buckling of the disk into and out of the plane.

In the future, we will continue making our simulations more realistic by increasing the particle number, including a background potential, and including a mass spectrum. We will make surface density and line-of-sight velocity maps of eccentric nuclear disks at later times than 200 orbital periods in order to observe the effect of a larger population of retrograde orbits on the line-of-velocity distribution. Chapter 4 will lead to many more projects, including the further investigation of the formation of eccentric nuclear disks in the outer Solar System and in exoplanetary systems. We will explore the likelihood of observing lopsided protoplanetary disks and will further investigate the idea of scattering comets towards the Sun due to the secular torques in the eccentric disk in the outer solar system. We will use the LSST survey simulator to confirm that our predicted lopsided disk of extreme trans-Neptunian objects will be accessible to the Vera Rubin Observatory due to come online in 2022.

The research presented here may lead to exciting observing projects. Our results in Chapter 2 indicate that eccentric nuclear disks are excellent drivers of TDEs, meaning that

galaxies hosting an eccentric nuclear disk are a great place to search for these energetic events. Our results from Chapter 3 help observers know what to expect as an indication of the presence of an eccentric nuclear disk in a galactic nucleus. Finally, our results in Chapter 4 show that the dynamics in planetary disks undergo an inclination instability that results in apsidal clustering, forming an eccentric nuclear disk which could be a driver of icy bodies approaching the Sun as comets.

Gruzinov et al. (2020) showed that a lopsided configuration can be an equilibrium mode of a rotating nuclear star cluster. This tells us that eccentric nuclear disks may be common in the Universe. We show that they are likely to be common in galactic nuclei as well as in planetary disks. Continuing to search for galaxies with offset or double nuclei and unusual velocity signatures is important. Obtaining observations of these galactic nuclei with better and better resolution will be key for checking and developing the theory. For example, understanding the orientation that we observe the eccentric nuclear disk in M31 at is very important for understanding the structure of the disk, its relationship with the supermassive black hole, and how likely it is to find an eccentric nuclear disk at the center of any galaxy. Similarly, we should continue observing exoplanetary systems and looking for lopsided disks to increase our knowledge of how these systems work and just how common they are.

Additional future work involves determining ways that eccentric nuclear disks could form in galactic nuclei. Hopkins & Quataert (2010a,b) show that an eccentric nuclear disk could form in a gas-rich major galaxy merger. The presence of an eccentric nuclear disk in a galaxy could therefore provide information about the galaxy's merger history. These disks could also form after a black hole kick due to anisotropic gravitational wave emission (Akiba et al., in prep). As shown in Chapter 4, they could even form from something like the inclination instability in an axisymmetric disk, simply from the collective gravity of pre-existing eccentric orbits.

As eccentric nuclear disks are likely to be very common, are important for TDEs in

galactic nuclei and comets approaching the Sun, and could form in a variety of ways, it will be highly informative to continue studying their dynamics and to further our understanding of how they evolve.

Bibliography

Alexander, T. 2017, ARA&A, 55, 17

Alexander, T., & Hopman, C. 2009, ApJ, 697, 1861

Alonso-Herrero, A., Pereira-Santaella, M., García-Burillo, S., et al. 2018, ApJ, 859, 144

Arcavi, I., Gal-Yam, A., Sullivan, M., et al. 2014, ApJ, 793, 38

Bacon, R., Emsellem, E., Combes, F., et al. 2001, A&A, 371, 409

Batygin, K., Adams, F. C., Brown, M. E., & Becker, J. C. 2019, PhR, 805, 1

Batygin, K., & Brown, M. E. 2016, AJ, 151, 22

Begelman, M. C., Blandford, R. D., & Rees, M. J. 1980, Natur, 287, 307

Beloborodov, A. M., Illarionov, A. F., Ivanov, P. B., & Polnarev, A. G. 1992, MNRAS, 259, 209

Bender, R., Kormendy, J., Bower, G., et al. 2005, ApJ, 631, 280

Blaes, O., Lee, M. H., & Socrates, A. 2002, ApJ, 578, 775

Bloom, J. S., Giannios, D., Metzger, B. D., et al. 2011, Sci, 333, 203

Bogdanović, T., Cheng, R. M., & Amaro-Seoane, P. 2014, ApJ, 788, 99

Bonnerot, C., & Rossi, E. M. 2019, MNRAS, 484, 1301

Bricman, K., & Gomboc, A. 2020, ApJ, 890, 73

Brown, C. K., & Magorrian, J. 2013, MNRAS, 431, 80

Chen, X., Sesana, A., Madau, P., & Liu, F. K. 2011, ApJ, 729, 13

Cohn, H., & Kulsrud, R. M. 1978, ApJ, 226, 1087

Corbin, E., Shaw, M. J., Kitchin, M. R., Hagon, J. P., & Jaros, M. 2001, SeScT, 16, 263

Cossins, P., Lodato, G., & Testi, L. 2010, MNRAS, 407, 181

Couch, W. J., & Sharples, R. M. 1987, MNRAS, 229, 423

Davidge, T. J., Simons, D. A., Rigaut, F., Doyon, R., & Crampton, D. 1997, AJ, 114, 2586

Dou, L., Wang, T., Yan, L., et al. 2017, ApJ, 841, L8

Dressler, A., & Gunn, J. E. 1983, ApJ, 270, 7

Dressler, A., & Richstone, D. O. 1988, ApJ, 324, 701

Einstein, A. 1916, AnP, 354, 769

Evans, C. R., & Kochanek, C. S. 1989, ApJ, 346, L13

Ferrarese, L., & Merritt, D. 2000, ApJ, 539, L9

Foote, H. R., Generozov, A., & Madigan, A.-M. 2020, ApJ, 890, 175

Ford, E. B., Kozinsky, B., & Rasio, F. A. 2000, ApJ, 535, 385

Frank, J., & Rees, M. J. 1976, MNRAS, 176, 633

Freedman, W. L., & Madore, B. F. 1990, ApJ, 365, 186

French, K. D., Arcavi, I., & Zabludoff, A. 2016, ApJ, 818, L21

—. 2017, ApJ, 835, 176

Gebhardt, K., et al. 2000, ApJ, 539, L13

Goldreich, P., & Tremaine, S. 1979, ApJ, 233, 857

Gruzinov, A., Levin, Y., & Zhu, J. 2020, ApJ, 905, 11

Guillochon, J., & Ramirez-Ruiz, E. 2013, ApJ, 767, 25

Gültekin, K., Gebhardt, K., Kormendy, J., et al. 2014, ApJ, 781, 112

Gürkan, M. A., & Hopman, C. 2007, MNRAS, 379, 1083

Hills, J. G. 1975, Natur, 254, 295

Hopkins, P. F., & Quataert, E. 2010a, MNRAS, 407, 1529

—. 2010b, MNRAS, 405, L41

Huang, J., Andrews, S. M., Pérez, L. M., et al. 2018, ApJ, 869, L43

Ida, S. 1990, Icar, 88, 129

Ivanov, P. B., & Novikov, I. D. 2001, ApJ, 549, 467

Jacobs, V., & Sellwood, J. A. 2001, ApJ, 555, L25

Kara, E., Dai, L., Reynolds, C. S., & Kallman, T. 2018, MNRAS, 474, 3593

Kavelaars, J. J., Lawler, S. M., Bannister, M. T., & Shankman, C. 2020, Perspectives on the distribution of orbits of distant Trans-Neptunian objects, ed. D. Prialnik, M. A. Barucci, & L. Young, 61–77

Kesden, M. 2012, PhRvD, 85, 024037

Khabibullin, I., Sazonov, S., & Sunyaev, R. 2014, MNRAS, 437, 327

King, I. R., Stanford, S. A., & Crane, P. 1995, AJ, 109, 164

Kormendy, J. 1988, ApJ, 325, 128

Kormendy, J., & Bender, R. 1999, ApJ, 522, 772

Kozai, Y. 1962, AJ, 67, 591

Lauer, T. R., Faber, S. M., Groth, E. J., et al. 1993, AJ, 106, 1436

Lauer, T. R., Tremaine, S., Ajhar, E. A., et al. 1996, ApJ, 471, L79

Lauer, T. R., Gebhardt, K., Richstone, D., et al. 2002, AJ, 124, 1975

Lauer, T. R., Faber, S. M., Gebhardt, K., et al. 2005, AJ, 129, 2138

Leloudas, G., Fraser, M., Stone, N. C., et al. 2016, NatAs, 1, 0002

Lidov, M. L. 1962, P&SS, 9, 719

Light, E. S., Danielson, R. E., & Schwarzschild, M. 1974, ApJ, 194, 257

Lightman, A. P., & Shapiro, S. L. 1977, ApJ, 211, 244

Lockhart, K. E., Lu, J. R., Peiris, H. V., et al. 2018, ApJ, 854, 121

Lodato, G., King, A. R., & Pringle, J. E. 2009, MNRAS, 392, 332

Lu, J. R., Ghez, A. M., Hornstein, S. D., et al. 2009, ApJ, 690, 1463

Lynden-Bell, D. 1979, MNRAS, 187, 101

MacLeod, M., Goldstein, J., Ramirez-Ruiz, E., Guillochon, J., & Samsing, J. 2014, ApJ, 794, 9

MacLeod, M., Guillochon, J., & Ramirez-Ruiz, E. 2012, ApJ, 757, 134

Madigan, A.-M., Halle, A., Moody, M., et al. 2018a, ApJ, 853, 141

Madigan, A.-M., Hopman, C., & Levin, Y. 2011, ApJ, 738, 99

Madigan, A.-M., & McCourt, M. 2016, MNRAS, 457, L89

Madigan, A.-M., Zderic, A., McCourt, M., & Fleisig, J. 2018b, AJ, 156, 141

Mainetti, D., Lupi, A., Campana, S., et al. 2017, A&A, 600, A124

Maksym, W. P., Ulmer, M. P., Eracleous, M. C., Guennou, L., & Ho, L. C. 2013, MNRAS, 435, 1904

Merritt, D. 2013, Dynamics and Evolution of Galactic Nuclei (Princeton University Press)

Naoz, S., Kocsis, B., Loeb, A., & Yunes, N. 2013, ApJ, 773, 187

Nieto, J. L., Macchetto, F. D., Perryman, M. A. C., di Serego Alighieri, S., & Lelievre, G. 1986, A&A, 165, 189

Peebles, P. J. E. 1972, ApJ, 178, 371

Peiris, H. V., & Tremaine, S. 2003, ApJ, 599, 237

Pfister, H., Toscani, M., Wong, T. H. T., et al. 2021, arXiv e-prints, arXiv:2103.05883

Phinney, E. S. 1989, in IAU Symp. 136: The Center of the Galaxy, 543–+

Poggianti, B. 2004, in Baryons in Dark Matter Halos, ed. R. Dettmar, U. Klein, & P. Salucci, 104

Press, W. H., & Teukolsky, S. A. 1977, ApJ, 213, 183

Prieto, J. L., Krühler, T., Anderson, J. P., et al. 2016, ApJ, 830, L32

Rauch, K. P., & Ingalls, B. 1998, MNRAS, 299, 1231

Rauch, K. P., & Tremaine, S. 1996, NewA, 1, 149

Rees, M. J. 1988, Natur, 333, 523

Rein, H., & Liu, S.-F. 2012, A&A, 537, A128

Rein, H., & Spiegel, D. S. 2015, MNRAS, 446, 1424

Rice, W. K. M., Armitage, P. J., Bonnell, I. A., et al. 2003, MNRAS, 346, L36

Rosotti, G. P., Benisty, M., Juhász, A., et al. 2020, MNRAS, 491, 1335

Salow, R. M., & Statler, T. S. 2001, ApJ, 551, L49

—. 2004, ApJ, 611, 245

Sambhus, N., & Sridhar, S. 2000, ApJ, 539, L17

—. 2002, A&A, 388, 766

Saxton, C. J., Younsi, Z., & Wu, K. 2016, MNRAS, 461, 4295

Shapiro, S. L., & Marchant, A. B. 1978, ApJ, 225, 603

Sil'chenko, O. K., Burenkov, A. N., & Vlasyuk, V. V. 1998, A&A, 337, 349

Stone, N. C., Generozov, A., Vasiliev, E., & Metzger, B. D. 2018, MNRAS, 480, 5060

Stone, N. C., Kesden, M., Cheng, R. M., & van Velzen, S. 2019, GReGr, 51, 30

Stone, N. C., & Metzger, B. D. 2016, MNRAS, 455, 859

Stone, N. C., & van Velzen, S. 2016, ApJ, 825, L14

Tadhunter, C., Spence, R., Rose, M., Mullaney, J., & Crowther, P. 2017, NatAs, 1, 0061

Tamayo, D., Rein, H., Shi, P., & Hernandez, D. M. 2020, MNRAS, 491, 2885

Tremaine, S. 1995, AJ, 110, 628

—. 1998, AJ, 116, 2015

Trujillo, C. 2020, Observational Constraints on an Undiscovered Giant Planet in our Solar System, ed. D. Prialnik, M. A. Barucci, & L. Young, 79–105

Trujillo, C. A., & Sheppard, S. S. 2014, Natur, 507, 471

Ulmer, A. 1999, ApJ, 514, 180

van der Marel, N., van Dishoeck, E. F., Bruderer, S., et al. 2013, Sci, 340, 1199

van Velzen, S. 2018, ApJ, 852, 72

van Velzen, S., Farrar, G. R., Gezari, S., et al. 2011, ApJ, 741, 73

van Velzen, S., Anderson, G. E., Stone, N. C., et al. 2016, Sci, 351, 62

Wang, J., & Merritt, D. 2004, ApJ, 600, 149

Wernke, H. N., & Madigan, A.-M. 2019, ApJ, 880, 42

—. 2021, ApJ, in review

Zalamea, I., Menou, K., & Beloborodov, A. M. 2010, MNRAS, 409, L25

Zauderer, B. A., Berger, E., Soderberg, A. M., et al. 2011, Natur, 476, 425

Zderic, A., Collier, A., Tiongco, M., & Madigan, A.-M. 2020, ApJ, 895, L27

Zderic, A., & Madigan, A.-M. 2020, AJ, 160, 50

Zderic, A., Tiongco, M., Collier, A., et al. 2021, arXiv e-prints, arXiv:2106.09739